Modeling the Flow in Surf Zone Waves

by

Jayaram Veeramony

and

Ib A. Svendsen

RESEARCH REPORT NO. CACR-99-04

August 1999

Center for Applied Coastal Research
Ocean Engineering Laboratory
University of Delaware
Newark, DE 19716

TABLE OF CONTENTS

LIST OF FIGURES

LIST OF TABLES

ABSTRACT

A Boussinesq-type model has been developed to describe the wave transformation in the nearshore region. The model is fully non-linear up to $O(\mu^2)$ where μ is the wave length non-dimensionalized by the water depth. The model is derived from the fundamental equations of continuity and momentum by assuming that the motion in the surf zone is rotational. This leads to a formulation wherein the terms in the momentum equation that describe breaking appear as functions of the vorticity generated in the roller region of a breaking wave. Thus, in addition to the wave height evolution, the model is able to predict the velocity field due to the short wave motion in the surf zone. This feature is an improvement over the existing formulations for breaking waves using Boussinesq equations.

The equations are solved numerically using finite-difference methods. A fourth-order Adams-Bashforth-Moulton predictor-corrector method is used for time-stepping and a combination of second-order and fourth-order scheme is used for evaluating the spatial derivatives. An absorbing-generating boundary condition is used at the offshore boundary to specify the incoming waves and to absorb the reflected/outgoing waves. A shelf with finite but very small water depth is used at the shoreline. Breaking is initiated when the maximum of the slope at the front face of the waves exceeds a certain limit. The boundary conditions needed to solve for the vorticity are obtained from an analysis of weakly turbulent hydraulic jumps.

Comparisons to semi-analytical results are presented for the case of solitary wave propagation and shoaling. Very good agreement between the model results and experimental data is obtained for the wave heights, wave set-up, the velocity field and the undertow. The model performance with regard to the wave mass flux, the radiation stress, the wave speed, the development of vorticity in the surf zone and the development of the roller is also presented.

Chapter 1

INTRODUCTION.

Wave breaking is a natural phenomenon that is observed widely in the near-shore region. By this process, energy is transferred from the organized wave motion to a wide spectrum of frequencies that include both high frequency turbulence and low frequency motions such as infra-gravity waves, long-shore/cross-shore currents and shear waves. These low frequency motions are not always visible to the naked eye, yet they play a very important role in the surf zone dynamics. Breaking waves are also the primary agents for the sediment motions on a coast. To model all these processes accurately, the process of breaking and the velocity field it creates in the surf zone have to be modeled accurately.

Not all waves break when they reach the shoreline. If the wavelength (L) is sufficiently large and the wave height (H) sufficiently small, they can be reflected from the shoreline. Thus, whether a wave breaks (or reflects) as it approaches the shore is a function of how steep the wave is (i.e., how large H/L is) and how gently the beach slopes. Iribarren and Nogales (1949) used the parameter

$$I_r = \frac{h_x}{\sqrt{H_0/L_0}} \tag{1.1}$$

where h_x is the beach slope, H_0 and L_0 are the deep water wave height and wave length respectively to determine the transition between wave reflection and wave breaking as the waves approach the shoreline.

Observations and experiments suggest that the type of wave breaking is also a function of the incident wave steepness and the slope of the beach. There is a

continuous spectrum of wave breaking patterns in the near shore region. However, it was found by Galvin (1968) that the parameter I_r as well as the inshore parameter

$$I_r' = \frac{h_x}{H_b/gT^2}, \tag{1.2}$$

where H_b is the wave height at breaking, g is the acceleration due to gravity and T is the wave period, can be used to classify the breaking waves into four main types. This classification is based on the physical appearance of the waves during breaking.

In a *spilling* breaker, a white cap manifests at the crest of a wave, which is sometimes preceded by a small jet at the crest, and spills down the front face of the wave. In a *plunging* breaker, a jet is formed near the crest of the wave which plunges forward into the water causing a "splash-down" at the point where the jet meets the water surface. A very prominent air pocket is created by this plunging jet. These two types of breaking are characterized by the high intensity of the turbulence and the formation of a quasi-steady propagating bore shortly after breaking has been initiated. In a *collapsing* breaker, the crest is unbroken, while the lower part of the wave front steepens and forms a mildly turbulent surface without the formation of a bore-like feature. In a *surging* breaker, the crest again remains unbroken and there is minor breaking as the base of the front face gets close to the shoreline. The turbulent intensity in these two types is mild in comparison to the spilling and plunging breakers.

Galvin (1968) found that in general the Iribarren number I_r can be related to the type of wave breaking as:

spilling when	$I_r < 0.46$
plunging when	$0.46 < I_r < 3.3$
surging or collapsing when	$I_r > 3.3$

Battjes (1974) gave the transition point between spilling breakers and plunging breakers as $I_r = 0.5$.

A good description of the various mechanisms involved in the process of wave breaking can be found in Peregrine (1983). Comprehensive reviews of the different types of models to describe breaking waves in both deep water and in shallow water

can be found in existing literature (Battjes 1988; Hamm *et al.* 1993; Southgate 1993; Svendsen 1999). These models can be classified into two main types: phase-averaged models that cannot resolve the individual short wave motion and phase-resolving models which directly simulate the short wave motion in the surf zone. The first type includes spectral models, refraction-diffraction models, probabilistic models and energy based models, to name a few.

The present study will focus on modeling spilling breakers in the shallow water region using a phase-resolving model. A brief overview of models of this type is presented below.

1.1 Phase-resolving models

Most of the phase-resolving models are based primarily on the assumption that the wavelength of the short waves in the near-shore region is large in comparison to the local water depth. These models can be classified into three categories:

1. models based on the non-linear shallow water equations (NSW models)
2. models based on the Boussinesq theory
3. models based on the full Reynolds equations

1.1.1 NSW models.

The origin of these models can be traced to Airy (1945) who studied long waves of finite amplitude using the NSW equations. In one-dimension, these equations are

$$\zeta_t + (\overline{u}(h+\zeta))_x = 0, \tag{1.3}$$

$$\overline{u}_t + \overline{u}\overline{u}_x + g\zeta_x = 0, \tag{1.4}$$

where $\overline{u}$ is the depth-averaged velocity, h is the local water depth and ζ is the instantaneous water surface elevation. Airy concluded that, even on a horizontal bottom, long waves modeled by these equations would continuously steepen as they propagate. This steepening would cause the waves to transform into "bores" or "hydraulic jumps" (see also Benjamin and Lighthill 1954).

The NSW equations are essentially the continuity and momentum equations simplified under the assumption that the waves are non-dispersive (which corresponds to the assumption of hydrostatic pressure). The advantage of the NSW equations is that they are simple to model and give a reasonably accurate representation of the wave profile. Examples of simulations using this type of model are given in Hibberd and Peregrine (1979), Packwood and Peregrine (1980) and Packwood (1983).

The NSW equations do not include any mechanism to represent wave breaking. Thus, waves modeled by these equations will steepen, even on a horizontal bottom, until the vertical accelerations can no longer be neglected. At this stage, the basic assumption that the pressure is hydrostatic becomes invalid.

In the numerical solutions of the equations, a dissipative scheme is generally used so that the wave front is frozen at some shape before the front face becomes vertical. The choice of the numerical scheme can ensure that the numerical dissipation is equal to the dissipation in a bore of the same height. The dissipation as well as the wave shape is strongly influenced by the grid sizes chosen for the simulations. A further disadvantage is that the position at which the wave shape is frozen also depends on the length of the computational domain. Thus, extreme care has to be exercised so that the waves in the surf zone are modeled properly.

It turns out, however, that these types of models are very practical for analyzing the full non-linear run-up in the swash zone, where dispersion effects are minimal (see, e.g., Kobayashi *et al.* 1987; Kobayashi *et al.* 1989; Cox *et al.* 1994).

1.1.2 Boussinesq-type models for breaking waves.

The past decade has seen the advancement of Boussinesq type models to predict the nearshore characteristics of breaking waves. The classical Boussinesq model (Boussinesq 1872; Mei and LeMehaute 1966; Peregrine 1967) is a weakly non-linear and weakly dispersive wave model which represents shallow water waves of moderate amplitude quite well. For a one-dimensional case, the equations can be

written as

$$\zeta_t + (\overline{u}(h+\zeta))_x = 0, \tag{1.5}$$

$$\overline{u}_t + \overline{u}\overline{u}_x + g\zeta_x - \frac{h}{2}(h\overline{u}_t)_{xx} - \frac{h^2}{6}\overline{u}_{xxt} = 0. \tag{1.6}$$

The model is based on a coupled set of partial differential equations that are, as in the NSW equations, the continuity and momentum equations. There are two additional terms in the momentum equation, which correspond to the contribution from the non-hydrostatic pressure due to the vertical acceleration.

The Boussinesq equations can also be derived in terms of the horizontal velocity at any arbitrary location in the water column (Nwogu 1993; Wei *et al.* 1995). The characteristics of the models vary depending on the formulation used.

Substantial effort has gone into extending the validity of the classical equations to intermediate and deep water regimes by improving either the linear dispersion characteristics of the weakly dispersive model (Madsen *et al.* 1991; Nwogu 1993), or by including higher order dispersive terms (Madsen and Schäffer 1998b; Madsen and Schäffer 1998a; Gobbi *et al.* 1999). Similarly, the shoaling characteristics have been improved by including full non-linear effects up to the order of dispersion retained (Wei *et al.* 1995; Madsen and Schäffer 1998a).

On the other hand, incorporation of wave breaking in such models has followed fairly heuristic principles. In the Boussinesq models, unlike the NSW models, as the wave fronts steepen, the amplitude dispersion balances the frequency dispersion. This feature of the models stabilizes the waves, allowing the waves to continue shoaling until the computations break down. To incorporate breaking in such models, it is necessary to determine the way in which breaking is to be included and how the associated energy dissipation changes those equations.

There are several ways in which the signature of the breaking has been included in Boussinesq models. One concept was based on the inclusion of an artificial eddy viscosity (Tao 1983). The other concepts use a roller model, based on the observations of Peregrine and Svendsen (1978) where the flow field was split into two regions - the upper "roller" region having a high shear and the lower region with potential flow.

Eddy viscosity formulations.

This is based on the concept of an artificial eddy viscosity term of the form $(\nu_t u_x)_x$, which is added to the momentum equations (see for example Zelt 1991; Karambas and Koutitas 1992; Wei *et al.* 1995; Kennedy *et al.* 1999). Different forms of this term were used in an attempt to conserve the momentum in the breaking region as well as to model the waves accurately. The value of the eddy viscosity is calibrated with experimental data. With suitable choices for the eddy viscosity, very good approximations to the wave height data can be obtained. However, there is no physical justification for such a term, which essentially has the same form as the turbulent normal stresses in the horizontal direction. Another disadvantage is that the flow is still modeled as a potential flow. Therefore, the velocity profile remains unchanged from the standard quadratic profile (or a higher order polynomial depending upon the order of the terms retained in the Boussinesq theory).

Excess pressure formulations.

This approach is based on the concept of a surface roller. The breaking term is incorporated in the model as an additional pressure term due to the weight of the roller (Deigaard and Fredsoe 1989). Brocchini *et al.* (1992) used this approach to describe wave breaking and found fairly good agreement with measurements.

Excess momentum formulations.

In these breaking models, the roller rides on the front face of the wave at the speed of the wave (Schäffer *et al.* 1992; Schäffer *et al.* 1993; Madsen *et al.* 1997). The velocity is assumed to have a constant value in the roller region equal to about 1.3 times the wave speed. This introduces a change in the velocity profile once the waves break, and hence an excess momentum flux, which simulates wave breaking. Similar to the previous methods, comparisons with experimental data show that the results for the wave heights and set-up can be modeled quite accurately, although the flow is essentially modeled as a potential flow. However, physically, the velocity profile assumed in such models is unrealistic. In addition, the roller is modeled as a solid body that travels with the wave. We know that this is not the case, as was also shown experimentally by Lin and Rockwell (1994).

Verticity formulations.

In this method, the breaking terms are derived directly from the fundamental equations by assuming that the flow field is rotational (Yu and Svendsen 1995; Svendsen *et al.* 1996; Veeramony and Svendsen 1998). It turns out that both the excess pressure and momentum terms appear in the momentum equation. The vorticity generated by the breaking is determined by solving the vorticity transport equation. The resulting velocity profiles are continuous everywhere and thus also provide information about the flow field in the surf zone.

1.1.3 Modeling the complete Reynolds equations.

Recently, simulations of breaking waves have been performed by Lin and Liu (1998a, 1998b). They solved the Reynolds equations for the mean flow and the $k-\epsilon$ equation for turbulent kinetic energy using the VOF method. The model results and experimental data were found to be in excellent agreement. The advantage of this type of modeling is that flow details such as turbulent intensities and shear stresses can be directly evaluated from the model results. However, it takes about 48 hours of CPU time on a supercomputer to simulate one minute of real time for the two-dimensional case (the 1D horizontal case). Hence, applications to practical cases are limited.

1.2 Outline of the dissertation.

The aim of this study is to develop a model that can describe the wave transformation in the near-shore region including the shoaling region and the surf zone. In addition, the model should also be able to describe the velocity field under the short waves in the breaking region. Following the approach of Yu and Svendsen (1995), a fully non-linear Boussinesq-type model has been derived, which has very good shoaling properties. The model also incorporates the development of the vorticity due to the breaking process. This enables the model to describe the velocity field in the breaking waves.

In Chapter 2, the governing equations are derived starting from the Reynolds equations. The continuity and momentum equations are integrated over the depth. The pressure terms are eliminated from the momentum equations yielding a coupled set of partial differential equations with the horizontal velocity (u) and the surface

elevation (ζ) as the two dependent variables. The depth variation of u is obtained from the equation for the stream function. This gives the velocity at any water depth as a function of depth averaged horizontal velocity and the vorticity generated by the breaking process. Substituting this expression of u into the continuity and momentum equations yield a Boussinesq-type model for surf zone waves. Following the approach of Madsen and Sørensen (1993), the linear dispersion characteristic of the model is improved. A Stokes-type perturbation analysis is performed to show the analytical characteristics of the model on a horizontal bottom.

The equation that describes the vorticity distribution in the surf zone is derived in Chapter 3. Instead of attempting to solve this equation numerically, an analytical solution is obtained using an asymptotic expansion in δ, where δ is the ratio of the wave height to the water depth. The solution is obtained to the two lowest orders in δ. The similarity between breaking waves and bores is used to obtain the boundary condition for this equation from the analysis of experimental data in hydraulic jumps.

The numerical solution to the governing equations is presented in Chapter 4. A fourth-order Adams-Bashforth-Moulton predictor-corrector method is used for the time stepping and a combination of second- and fourth-order finite difference scheme is used for the spatial derivatives. Based on the method of von Neumann, the stability range for the linearized governing equations is evaluated. The absorbing-generating boundary condition used at the offshore and the absorption mechanism at the shoreline is also described. The boundary conditions for the vorticity, derived from the analysis in Chapter 3, are also shown. The modeling of the start of the wave breaking is described. The spurious short waves generated by the non-linear interactions, which cause stability problems in the numerical model, are eliminated using a numerical filter developed by Shapiro (1970).

In Chapter 5, the computational results are presented. The stability and conservative properties of the numerical scheme are illustrated by comparing the permanent form solution of the solitary wave to the solution given by Tanaka (1986). The computations of solitary wave shoaling, which illustrates the non-linear properties of the model are shown. These results are compared to the results from solving the

exact boundary value problem for irrotational motion (Grilli *et al.* 1994). The magnitudes of the terms that describe breaking are discussed, along with the vorticity distribution in the surf zone. The shoaling and breaking characteristics of the model, with regard to the wave heights, the crest and trough elevations and the set-up, are compared to both experimental data and the model of Kennedy *et al.* (1999). The distinguishing feature of the present model in comparison to the other Boussinesq-type models is that the velocity field in the surf zone can also be described. This feature is illustrated by comparing the model results to the instantaneous velocities under the waves in the surf zone and the measured undertow. The wave mass flux, the wave radiation stress and the phase speed results are also presented.

Chapter 6 presents the conclusions of this study, along with some suggestions for enhancements to the model.

Chapter 2

EQUATIONS FOR THE BREAKING MODEL.

In this chapter, a brief but comprehensive derivation of the governing equations that describe breaking waves is presented. The model is based on Boussinesq type equations where the idea is to reduce the equations from two dimensions (horizontal and vertical) to one dimension (horizontal) using shallow water assumptions. Such types of equations have been used extensively in the shallow water region in the nearshore with good results (see, e.g., Wei *et al.* 1995; Madsen *et al.* 1997; Gobbi *et al.* 1999).

The scaling arguments for shallow water waves are introduced first (section 2.1). The depth integrated continuity equation is derived from the differential form using the kinematic conditions at the bottom and at the surface. The pressure term is eliminated from the depth-integrated horizontal and vertical momentum equations yielding one equation for the conservation of momentum. The approximation for depth variation of the horizontal velocity is then obtained from the equation for stream function. Substituting this approximation into the momentum equation then yields the equations for breaking waves (section 2.2).

Stokes type analysis is performed on both the weakly non-linear model and the fully non-linear model (section 2.3). The analysis shows how, on a horizontal bottom, the non-linear characteristics of the Boussinesq models with and without dispersion enhancement compare with the results of third-order Stokes theory.

2.1 The equations of motion.

The length scales associated with wave motion are the characteristic wave amplitude, a_0, the characteristic water depth, h_0, and the characteristic wave number, k_0. These scales yield a set of two independent, non-dimensional parameters

$$\delta = a_0/h_0 \quad \text{and} \quad \mu = k_0 h_0. \tag{2.1a}$$

The first parameter, δ, describes the relative wave height which is a measure of the degree of non-linearity of the wave. The second, μ, describes the relative water depth, which is a measure of dispersiveness of the waves. In this study, we restrict ourselves to shallow water waves, $\mu^2 \ll O(1)$. The classical Boussinesq equations correspond to an additional restriction of weak non-linearity ($\delta/\mu^2 = O(1)$).

For shallow water waves, the independent variables are scaled as

$$x = k_0\hat{x}, \quad z = \hat{z}/h_0, \quad \text{and} \quad t = k_0\sqrt{gh_0}\hat{t}, \tag{2.1b}$$

where the $\hat{()}$ represents the dimensional quantities. The dependent variables $\hat{\zeta}$ (instantaneous water surface elevation) and $\hat{\psi}$ (stream function) are scaled as

$$\zeta = \hat{\zeta}/a_0 \quad \text{and} \quad \psi = \hat{\psi}/(\delta h_0\sqrt{gh_0}). \tag{2.1c}$$

Using these scales, the non-dimensional horizontal velocity (u), the vertical velocity (w) and the vorticity (ω) are

$$\hat{u} = \frac{\partial\hat{\psi}}{\partial\hat{z}} = \delta\sqrt{gh_0}u, \tag{2.1d}$$

$$\hat{w} = -\frac{\partial\hat{\psi}}{\partial\hat{x}} = \delta\mu\sqrt{gh_0}w, \tag{2.1e}$$

$$\hat{\omega} = \frac{\partial\hat{u}}{\partial\hat{z}} - \frac{\partial\hat{w}}{\partial\hat{x}} = \frac{\delta\sqrt{gh_0}}{h_0}\left(\frac{\partial u}{\partial z} - \mu^2\frac{\partial w}{\partial x}\right) = \frac{\delta\sqrt{gh_0}}{h_0}\omega. \tag{2.1f}$$

To the lowest order of approximation for irrotational motion, where $\omega = 0$, $\partial u/\partial z \sim O(\mu^2)$, i.e., u does not vary over depth. In the case of breaking waves, the vorticity generated is quite strong. Therefore we can expect $\omega \sim O(1)$ in the surf zone. The presence of this vorticity is utilized to formulate and develop the

breaking model detailed in this study. In the following, the model is developed for the two-dimensional case.

The beach slope, $\hat{h}_{\hat{x}}$, is an additional independent parameter which, when scaled using the arguments above, is

$$\hat{h}_{\hat{x}} = \mu h_x, \tag{2.1g}$$

giving $h_x L/h \sim O(2\pi)$, which is a *very* steep beach. Hence, it seems justified to assume $\hat{h}_{\hat{x}} = O(\mu^2)$. This, in essence, implies that the scale for the relative change in water depth is larger than the typical wave lengths considered. Later, it will be shown using the computed results from the model that this assumption is not very restrictive, particularly for waves shoaling on a plane beach.

2.1.1 Depth integrated continuity equation.

For a fluid with constant density, the two-dimensional differential form of the equation for continuity is

$$\frac{\partial \hat{u}}{\partial \hat{x}} + \frac{\partial \hat{w}}{\partial \hat{z}} = 0, \tag{2.2}$$

where $\hat{u}$ and $\hat{w}$ are the velocities in the $\hat{x}$ (horizontal) and $\hat{z}$ (vertical) directions, respectively. The still water line is at $\hat{z} = 0$. Integrating (2.2) over the water column $(-\hat{h} \leq \hat{z} \leq \hat{\zeta})$ gives

$$\int_{-\hat{h}}^{\hat{\zeta}} \frac{\partial \hat{u}}{\partial \hat{x}}\, dz + \hat{w}(\hat{\zeta}) - \hat{w}(-\hat{h}) = 0, \tag{2.3}$$

where $\hat{\zeta}$ is the instantaneous free surface elevation and $\hat{z} = -\hat{h}$ represents the bottom. In this present study, we only consider impermeable bottom where there is no flow through the bottom boundary. This condition is expressed as

$$\hat{w}(-\hat{h}) = -\hat{u}(-\hat{h})\frac{\partial \hat{h}}{\partial \hat{x}}. \tag{2.4}$$

At the free surface, the particles on the surface stay at the surface, which gives the surface boundary condition as

$$\hat{w}(\hat{\zeta}) = \frac{\partial \hat{\zeta}}{\partial \hat{t}} + \hat{u}(\hat{\zeta})\frac{\partial \hat{\zeta}}{\partial \hat{x}}. \tag{2.5}$$

Applying the Leibniz rule of differentiation of integrals to (2.3) and using the boundary conditions given by (2.4) and (2.5) to eliminate the vertical velocities at the boundaries yield

$$\frac{\partial \hat{\zeta}}{\partial \hat{t}} + \frac{\partial}{\partial \hat{x}} \int_{-\hat{h}}^{\hat{\zeta}} \hat{u}\, d\hat{z} = 0. \tag{2.6}$$

The instantaneous volume flux is defined as

$$\hat{Q} \equiv \int_{-\hat{h}}^{\hat{\zeta}} \hat{u}\, d\hat{z}. \tag{2.7}$$

With the scaling given by (2.1), the non-dimensionalized continuity equation is

$$\frac{\partial \zeta}{\partial t} + \frac{\partial Q}{\partial x} = 0. \tag{2.8}$$

2.1.2 Depth integrated momentum equation.

The differential form of the horizontal momentum equation is

$$\frac{\partial \hat{u}}{\partial \hat{t}} + \frac{\partial \hat{u}^2}{\partial \hat{x}} + \frac{\partial \hat{u}\hat{w}}{\partial \hat{z}} = -\frac{1}{\rho}\frac{\partial \hat{p}}{\partial \hat{x}} + \frac{1}{\rho}\left(\frac{\partial \hat{\tau}_{xx}}{\partial \hat{x}} + \frac{\partial \hat{\tau}_{xz}}{\partial \hat{z}}\right). \tag{2.9}$$

Integrating over depth and using the Leibniz rule gives

$$\begin{aligned}
&\frac{\partial}{\partial \hat{t}} \int_{-\hat{h}}^{\hat{\zeta}} \hat{u}\, d\hat{z} + \frac{\partial}{\partial \hat{x}} \int_{-\hat{h}}^{\hat{\zeta}} \hat{u}^2\, d\hat{z} - \left[\hat{u}\left(\frac{\partial \hat{\zeta}}{\partial \hat{t}} + \hat{u}\frac{\partial \hat{\zeta}}{\partial \hat{x}} - \hat{w}\right)\right]_{\hat{\zeta}} - \left[\hat{u}\left(\hat{u}\frac{\partial \hat{h}}{\partial \hat{x}} + \hat{w}\right)\right]_{-\hat{h}} \\
&\quad = \frac{1}{\rho}\frac{\partial}{\partial \hat{x}} \int_{-\hat{h}}^{\hat{\zeta}} (-\hat{p} + \hat{\tau}_{xx})\, d\hat{z} + \frac{\hat{p}(-\hat{h})}{\rho}\frac{\partial \hat{h}}{\partial \hat{x}} + \frac{1}{\rho}\left[(\hat{\tau}_{xz})_{\hat{\zeta}} + (\hat{p} - \hat{\tau}_{xx})_{\hat{\zeta}}\frac{\partial \hat{\zeta}}{\partial \hat{x}}\right] \\
&\qquad - \frac{1}{\rho}\left[(\hat{\tau}_{xz})_{-\hat{h}} - (\hat{\tau}_{xx})_{-\hat{h}}\frac{\partial \hat{h}}{\partial \hat{x}}\right].
\end{aligned} \tag{2.10}$$

The last two terms on the right hand side are the horizontal components of the forces on the surface and the bottom respectively. Using (2.4) and (2.5) and defining

$$\hat{R}_x^s \equiv \frac{1}{\rho}\left[(\hat{\tau}_{xz})_{\hat{\zeta}} + (\hat{p} - \hat{\tau}_{xx})_{\hat{\zeta}}\frac{\partial \hat{\zeta}}{\partial \hat{x}}\right], \tag{2.11a}$$

$$\hat{\tau}_x^B \equiv \frac{1}{\rho}\left[(\hat{\tau}_{xz})_{-\hat{h}} - (\hat{\tau}_{xx})_{-\hat{h}}\frac{\partial \hat{h}}{\partial \hat{x}}\right], \tag{2.11b}$$

results in the depth integrated horizontal momentum equation in dimensional form

$$\frac{\partial}{\partial \hat{t}} \int_{-\hat{h}}^{\hat{\zeta}} \hat{u}\, d\hat{z} + \frac{\partial}{\partial \hat{x}} \int_{-\hat{h}}^{\hat{\zeta}} \hat{u}^2\, d\hat{z} = \frac{\hat{p}(-\hat{h})}{\rho} \frac{\partial \hat{h}}{\partial \hat{x}} + \frac{\partial}{\partial \hat{x}} \int_{-\hat{h}}^{\hat{\zeta}} (-\hat{p} + \hat{\tau}_{xx})\, d\hat{z} + \hat{R}_x^s - \hat{\tau}_x^B. \tag{2.12}$$

In this study, only the region from intermediate/shallow water depths to the shoreline is considered. Then the effect of horizontal surface forces, such as due to wind, is minimal. To further simplify the problem, we also choose to neglect the shear stresses at the bottom at this time. This implies a free-slip condition at the bottom. In addition, the small deviatoric normal stresses are omitted. Thus, the non-dimensional form of the simplified equation corresponding to (2.12) is

$$\frac{\partial Q}{\partial t} + \delta \frac{\partial}{\partial x} \int_{-h}^{\delta\zeta} u^2\, dz = p(-h) \frac{\partial h}{\partial x} - \frac{\partial}{\partial x} \int_{-h}^{\delta\zeta} p\, dz. \tag{2.13}$$

The expression for pressure can be obtained from the depth integrated vertical momentum equation. Again, proceed as before and start with the vertical momentum equation in differential form

$$\frac{\partial \hat{w}}{\partial \hat{t}} + \frac{\partial \hat{u}\hat{w}}{\partial \hat{x}} + \frac{\partial \hat{w}^2}{\partial \hat{z}} = -\frac{1}{\rho} \frac{\partial \hat{p}}{\partial \hat{z}} + \frac{1}{\rho} \left(\frac{\partial \hat{\tau}_{xz}}{\partial \hat{x}} + \frac{\partial \hat{\tau}_{zz}}{\partial \hat{z}} \right). \tag{2.14}$$

Integrating from the surface to a level $\hat{z}$ and using the Leibniz rule along with the boundary conditions (2.4) and (2.5) gives the expression for pressure, which in dimensional form is

$$\frac{\hat{p}(\hat{z})}{\rho} = g(\hat{\zeta} - \hat{z}) - \hat{w}^2 + \frac{\partial}{\partial \hat{t}} \int_{\hat{z}}^{\hat{\zeta}} \hat{w}\, d\hat{z} + \frac{\partial}{\partial \hat{x}} \int_{\hat{z}}^{\hat{\zeta}} (\hat{u}\hat{w} - \frac{\hat{\tau}_{xz}}{\rho})\, d\hat{z}, \tag{2.15}$$

where the small contributions from the vertical components of the forces at the surface have also been omitted. Notice that formally, $\hat{z} = \hat{z}(x)$ in the lower limit of the integrals. The first term represents the hydrostatic pressure component, the second term represents the contribution from the vertical fluid motion, the third term is the effect of the vertical acceleration of the fluid column and the last term represents the weight of the water column supported by the adjacent water columns. Using the scalings given by (2.1), (2.15) is

$$p(z) = (\zeta - \frac{z}{\delta}) - \delta\mu^2 w^2 + \mu^2 \frac{\partial}{\partial t} \int_z^{\delta\zeta} w\, dz + \delta\mu^2 \frac{\partial}{\partial x} \int_z^{\delta\zeta} uw\, dz$$

$$-\frac{\partial}{\partial \hat{x}}\int_{\hat{z}}^{\hat{\zeta}}\frac{\hat{\tau}_{xz}}{\delta\rho g h_0}\,d\hat{z}. \tag{2.16}$$

The scaling for the turbulent stress term $\hat{\tau}_{xz}$ is obtained noting that there is no contribution from this term outside the breaking region. Inside the surf zone, measurements indicate (see, e.g., Cox *et al.* 1995) that the eddy viscosity $\hat{\nu}_t \simeq 0.03\hat{h}\sqrt{g\hat{h}}$. Therefore, the eddy viscosity is scaled as

$$\hat{\nu}_t = \mu h_0\sqrt{g h_0}\nu_t, \tag{2.17}$$

which gives the scale for the turbulent shear stress as

$$\hat{\tau}_{xz} = \hat{\nu}_t\left(\frac{\partial \hat{u}}{\partial \hat{z}} + \frac{\partial \hat{w}}{\partial \hat{x}}\right) = \delta\mu\rho g h_0\nu_t\left(\frac{\partial u}{\partial z} + \mu^2\frac{\partial w}{\partial x}\right). \tag{2.18}$$

Substituting (2.18) into (2.16) and neglecting terms smaller than $O(\mu^2)$, the vertical momentum equation reads

$$\begin{aligned} p(z) =&(\zeta - \frac{z}{\delta}) - \delta\mu^2 w^2 + \mu^2\frac{\partial}{\partial t}\int_z^{\delta\zeta} w\,dz + \delta\mu^2\frac{\partial}{\partial x}\int_z^{\delta\zeta} uw\,dz \\ &- \mu^2\frac{\partial}{\partial x}\int_z^{\delta\zeta}\nu_t\frac{\partial u}{\partial z}\,dz + O(\mu^4). \end{aligned} \tag{2.19}$$

Taking the derivative in x of this expression for pressure, integrating over the entire water column and applying the Leibniz rule gives

$$\begin{aligned} \frac{\partial}{\partial x}\int_{-h}^{\delta\zeta} p\,dz =& (h+\delta\zeta)\zeta_x - \delta\mu^2\int_{-h}^{\delta\zeta}\frac{\partial w^2}{\partial x}\,dz + \mu^2\int_{-h}^{\delta\zeta}\frac{\partial^2}{\partial x\partial t}\int_z^{\delta\zeta} w\,dz\,dz \\ &+ \delta\mu^2\int_{-h}^{\delta\zeta}\frac{\partial^2}{\partial x^2}\int_z^{\delta\zeta} uw\,dz\,dz + p(-h)\frac{\partial h}{\partial x} \\ &- \mu^2\int_{-h}^{\delta\zeta}\frac{\partial^2}{\partial x^2}\int_z^{\delta\zeta}\nu_t\frac{\partial u}{\partial z}\,dz\,dz + O(\mu^4). \end{aligned} \tag{2.20}$$

Substituting (2.20) in (2.13) results in the equation

$$\begin{aligned} &\frac{\partial Q}{\partial t} + \delta\frac{\partial}{\partial x}\int_{-h}^{\delta\zeta} u^2\,dz + (h+\delta\zeta)\zeta_x - \delta\mu^2\int_{-h}^{\delta\zeta}\frac{\partial w^2}{\partial x}\,dz \\ &\quad + \mu^2\int_{-h}^{\delta\zeta}\frac{\partial^2}{\partial x\partial t}\int_z^{\delta\zeta} w\,dz\,dz + \delta\mu^2\int_{-h}^{\delta\zeta}\frac{\partial^2}{\partial x^2}\int_z^{\delta\zeta} uw\,dz\,dz \end{aligned}$$

$$-\mu^2 \int_{-h}^{\delta\zeta} \frac{\partial^2}{\partial x^2} \int_{z}^{\delta\zeta} \nu_t \frac{\partial u}{\partial z}\, dz\, dz = O(\mu^4). \tag{2.21}$$

The vertical velocity in the above equation can be replaced with the horizontal velocity using the continuity equation

$$w(z) = -\frac{\partial}{\partial x} \int_{-h}^{z} u\, dz, \tag{2.22}$$

which gives the combined momentum equation in terms of the horizontal velocity and the water surface elevation as

$$\begin{aligned}
&\frac{\partial Q}{\partial t} + \delta \frac{\partial}{\partial x} \int_{-h}^{\delta\zeta} u^2\, dz + (h+\delta\zeta)\zeta_x - \mu^2 \int_{-h}^{\delta\zeta} \frac{\partial^2}{\partial x \partial t} \int_{z}^{\delta\zeta} \frac{\partial}{\partial x} \int_{-h}^{z} u\, dz\, dz\, dz \\
&\quad - \delta\mu^2 \int_{-h}^{\delta\zeta} \frac{\partial}{\partial x} \left(\frac{\partial}{\partial x} \int_{-h}^{z} u\, dz \right)^2 dz - \mu^2 \int_{-h}^{\delta\zeta} \frac{\partial^2}{\partial x^2} \int_{z}^{\delta\zeta} \nu_t \frac{\partial u}{\partial z}\, dz\, dz \\
&\quad - \delta\mu^2 \int_{-h}^{\delta\zeta} \frac{\partial^2}{\partial x^2} \int_{z}^{\delta\zeta} u \frac{\partial}{\partial x} \int_{-h}^{z} u\, dz\, dz\, dz \\
&\quad = 0.
\end{aligned} \tag{2.23}$$

2.1.3 The approximate equation for the horizontal velocity.

To solve (2.8) and (2.23), the depth variation of the horizontal velocity u must be determined. In traditional Boussinesq models, the shallow water assumption is utilized to represent the vertical variation of the velocity potential ϕ, where $u = \partial\phi/\partial x$, by an infinite polynomial series. The coefficients of this polynomial are obtained by solving the Laplace equation and applying the boundary condition on ϕ. From this approximation of ϕ, the depth variation of u is obtained. However, in the surf zone, strong vorticity is generated by the breaking waves. Consequently, the velocities can no longer be represented by a potential function. Instead, the stream function $\hat{\psi}$ is used, which satisfies

$$\hat{u} = \frac{\partial \hat{\psi}}{\partial \hat{z}} \quad \text{and} \quad \hat{w} = -\frac{\partial \hat{\psi}}{\partial \hat{x}}, \tag{2.24}$$

which implies

$$\hat{\psi}_{\hat{x}\hat{x}} + \hat{\psi}_{\hat{z}\hat{z}} = \hat{\omega}, \tag{2.25}$$

or, in non-dimensional form

$$\mu^2\psi_{xx} + \psi_{zz} = \omega. \tag{2.26}$$

Analogous to the derivation of the classical Boussinesq equations, the depth variation of both the stream function and the vorticity is represented by an infinite polynomial series

$$\psi = \sum_{n=0}^{\infty}(z+h)^n\psi_n(x,t), \tag{2.27a}$$

$$\omega = \sum_{n=0}^{\infty}(z+h)^n\omega_n(x,t). \tag{2.27b}$$

Then, from (2.27a),

$$\psi_x = \sum_{n=0}^{\infty}(z+h)^n[(\psi_n)_x + (n+1)h_x\psi_{n+1}], \tag{2.28a}$$

$$\psi_{xx} = \sum_{n=0}^{\infty}(z+h)^n[(\psi_n)_{xx} + 2(n+1)h_x(\psi_{n+1})_x + (n+1)h_{xx}\psi_{n+1} + (n+1)(n+2)h_x^2\psi_{n+2}], \tag{2.28b}$$

and

$$\psi_{zz} = \sum_{n=0}^{\infty}(z+h)^n[(n+1)(n+2)\psi_{n+2}]. \tag{2.28c}$$

Substituting (2.27b), (2.28b) and (2.28c) into (2.26),

$$\sum_{n=0}^{\infty}(z+h)^n[\mu^2(\psi_n)_{xx} + 2\mu^2(n+1)h_x(\psi_{n+1})_x + \mu^2(n+1)h_{xx}\psi_{n+1} + (n+1)(n+2)\psi_{n+2}(1+\mu^2h_x^2) - \omega_n] = 0, \tag{2.29}$$

which gives the recurrence relation

$$\psi_{n+2} = \frac{\omega_n - \mu^2(\psi_n)_{xx} - 2\mu^2(n+1)h_x(\psi_{n+1})_x - \mu^2(n+1)h_{xx}\psi_{n+1}}{(n+1)(n+2)(1+\mu^2h_x^2)}. \tag{2.30}$$

Using this relation and the boundary conditions for ψ, the individual terms in the polynomial series for ψ (2.27a) can now be determined. The boundary conditions are

$$\psi(z=-h) = 0 \quad \Rightarrow \quad \psi_0 = 0, \tag{2.31a}$$

$$\psi_z(z=-h)=u_0 \quad \Rightarrow \quad \psi_1=u_0, \tag{2.31b}$$

where u_0 is the velocity at the bottom ($z=-h$). The free-slip condition at the sea bed implies that the vorticity at the bottom (ω_0) is zero.

Retaining only terms up to $O(\mu^2)$, consistent with the weak dispersion assumption mentioned at the beginning, the recurrence relation (2.30) yields

$$\psi_1=\frac{\omega_0}{(n+1)(n+2)}-2\mu^2h_x\frac{(u_0)_x}{n+2}-\mu^2h_{xx}\frac{u_0}{n+2}+O(\mu^4), \tag{2.32a}$$

$$\begin{aligned}\psi_2=&\frac{\omega_1}{(n+1)(n+2)}-\mu^2\frac{(u_0)_{xx}}{(n+1)(n+2)}-2\mu^2h_x\frac{(\omega_0)_x}{n(n+1)(n+2)}\\&-\mu^2h_{xx}\frac{\omega_0}{n(n+1)(n+2)}+O(\mu^4),\end{aligned} \tag{2.32b}$$

$$\begin{aligned}\psi_{n+2}=&\frac{\omega_n}{(n+1)(n+2)}-\mu^2\frac{(\omega_{n-2})_{xx}}{(n-1)n(n+1)(n+2)}-2\mu^2h_x\frac{(\omega_{n-1})_x}{n(n+1)(n+2)}\\&-\mu^2h_{xx}\frac{\omega_{n-1}}{n(n+1)(n+2)}+O(\mu^4),\quad \text{n}=3,4,\cdots.\end{aligned} \tag{2.32c}$$

Substituting (2.32a) - (2.32c) in (2.27a), the expression for the stream function is obtained as

$$\begin{aligned}\psi=u_0(z+h)&-\frac{1}{2}\mu^2(z+h)^2[2h_xu_{0_x}+h_{xx}u_0]-\frac{\mu^2}{6}u_{0_{xx}}(z+h)^3\\&+\sum_{n=0}^{\infty}\frac{\omega_n}{(n+1)(n+2)}(z+h)^{n+2}\\&-\mu^2\sum_{n=0}^{\infty}\frac{(\omega_n)_{xx}+2(n+1)h_x(\omega_{n+1})_x+(n+1)h_{xx}\omega_{n+1}}{(n+1)(n+2)(n+3)(n+4)}(z+h)^4.\end{aligned} \tag{2.33}$$

Notice that in the summation over ω_n, all terms are formally the same order of magnitude. Hence the summation cannot be truncated. However, the summations involving ω_n are equivalent to integrals over the water column (from (2.27b)). Thus, the expression for the stream function is

$$\begin{aligned}\psi=u_0(z+h)&-\frac{1}{2}\mu^2(z+h)^2[2h_xu_{0_x}+h_{xx}u_0]-\frac{\mu^2}{6}u_{0_{xx}}(z+h)^3\\&+\int_{-h}^{z}\int_{-h}^{z}\omega\,dz\,dz-\mu^2\int_{-h}^{z}\int_{-h}^{z}\int_{-h}^{z}\int_{-h}^{z}\omega_{xx}\,dz\,dz\,dz\,dz+O(\mu^4).\end{aligned} \tag{2.34}$$

An alternative derivation of the expression for ψ, by direct integration of (2.26), is given in Appendix A.

From (2.34), the horizontal velocity is obtained by differentiation with respect to z as

$$u = u_0 - \mu^2(z+h)[2h_x u_{0_x} + h_{xx}u_0] - \frac{\mu^2}{2}u_{0_{xx}}(z+h)^2 + \int_{-h}^{z} \omega \, dz - \mu^2 \int_{-h}^{z}\int_{-h}^{z}\int_{-h}^{z} \omega_{xx} \, dz \, dz \, dz + O(\mu^4). \tag{2.35}$$

This expression for the horizontal velocity is different from that obtained by Yu (1996) in that the gradients of the slope do not appear explicitly in the terms involving the vorticity. Notice that there are two basic components in the expression for the horizontal velocity. The first three terms constitute the expression for the horizontal velocity in the standard weakly non-linear, weakly dispersive Boussinesq equations. The rest of the terms are associated with the presence of vorticity in the flow field. In the region before breaking where there is no generation of vorticity at the surface, these terms vanish. Thus, we define the potential component of the velocity (u_p) and the rotational component of the velocity (u_r) as

$$u_p \equiv u_0 - \mu^2(z+h)[2h_x u_{0_x} + h_{xx}u_0] - \frac{\mu^2}{2}u_{0_{xx}}(z+h)^2 + O(\mu^4), \tag{2.36a}$$

$$u_r \equiv \int_{-h}^{z} \omega \, dz - \mu^2 \int_{-h}^{z}\int_{-h}^{z}\int_{-h}^{z} \omega_{xx} \, dz \, dz \, dz + O(\mu^4), \tag{2.36b}$$

so that the total velocity is

$$u = u_p + u_r. \tag{2.37}$$

The depth averaged potential velocity is then

$$\begin{aligned}\overline{u}_p &\equiv \frac{1}{h+\delta\zeta}\int_{-h}^{\delta\zeta} u_p \, dz \\ &= u_0 - \frac{1}{2}\mu^2(h+\delta\zeta)(hu_0)_{xx} + \frac{\mu^2}{2}(h+\delta\zeta)(h^2 - \frac{\Delta_2}{3})u_{0_{xx}} + O(\mu^4),\end{aligned} \tag{2.38}$$

where $\Delta_2 \equiv \delta^2\zeta^2 - \delta\zeta h + h^2$. The velocity at the bottom is now expressed as

$$u_0 = \overline{u}_p + \frac{1}{2}\mu^2(h+\delta\zeta)(hu_0)_{xx} - \frac{\mu^2}{2}(h+\delta\zeta)(h^2 - \frac{\Delta_2}{3})u_{0_{xx}} + O(\mu^4). \tag{2.39}$$

Substituting (2.39) into (2.36a) and keeping terms only up to $O(\mu^2)$,

$$u_p = \overline{u}_p + \mu^2(\frac{\Delta_1}{2} - z)(h\overline{u}_p)_{xx} + \frac{\mu^2}{2}\left(\frac{\Delta_2}{3} - z^2\right)\overline{u}_{p_{xx}}, \tag{2.40}$$

where $\Delta_1 \equiv \delta\zeta - h$. The total velocity can now be expressed in terms of the depth-averaged potential velocity and the rotational velocity as

$$\begin{aligned} u = \overline{u}_p + \mu^2(\frac{\Delta_1}{2} - z)(h\overline{u}_p)_{xx} + \frac{\mu^2}{2}\left(\frac{\Delta_2}{3} - z^2\right)\overline{u}_{p_{xx}} \\ + \int_{-h}^{z} \omega \, dz - \mu^2 \int_{-h}^{z}\int_{-h}^{z}\int_{-h}^{z} \omega_{xx} \, dz \, dz \, dz + O(\mu^4). \end{aligned} \tag{2.41}$$

2.2 The breaking models.

Using the expression for u given by (2.41), the momentum equation can be reduced from a two-dimensional to a one-dimensional description of the flow. The accuracy of the model is entirely dependent upon the order of the terms retained both in δ and μ. A weakly non-linear assumption, where $O(\delta) \sim O(\mu^2)$ yields the classical Boussinesq equations in the shoaling region which is detailed in the first part of this section. As will be shown later, depending on the form of the equations, this assumption can lead to a significant misrepresentation of the wave heights close to the breaking region. Extending the validity in this region involves retaining terms which are higher order in δ.

2.2.1 Weakly non-linear breaking model.

From (2.23), keeping terms only up to $O(\delta, \mu^2)$, the momentum equation is

$$\begin{aligned} \frac{\partial Q}{\partial t} + \delta\frac{\partial}{\partial x}\int_{-h}^{\delta\zeta} u^2 \, dz + (h + \delta\zeta)\zeta_x - \mu^2 \int_{-h}^{0} \frac{\partial^2}{\partial x \partial t}\int_{z}^{0} \frac{\partial}{\partial x}\int_{-h}^{z} u \, dz \, dz \, dz \\ - \mu^2 \int_{-h}^{\delta\zeta} \frac{\partial^2}{\partial x^2}\int_{z}^{\delta\zeta} \nu_t \frac{\partial u}{\partial z} \, dz \, dz = 0, \end{aligned} \tag{2.42}$$

and with similar approximation, the horizontal velocity given by (2.41) reduces to

$$u = \overline{u}_p - \mu^2(\frac{h}{2} + z)(h\overline{u}_p)_{xx} + \frac{\mu^2}{2}\left(\frac{h^2}{3} - z^2\right)\overline{u}_{p_{xx}} + u_r + O(\delta\mu^2, \mu^4). \tag{2.43}$$

The continuity equation remains unchanged from (2.8) and is exact. The terms involving the integrals can now be evaluated. Notice that these terms are of $O(\delta, \mu^2)$ and therefore only terms of $O(1)$ in u need to be retained. Thus,

$$\begin{aligned}\int_{-h}^{\delta\zeta} u^2\, dz &= \int_{-h}^{\delta\zeta} (\overline{u}_p + u_r)^2\, dz + O(\mu^2) \\ &= \int_{-h}^{\delta\zeta} ({\overline{u}_p}^2 + 2\overline{u}_p\overline{u}_r + {\overline{u}_r}^2) + (2\overline{u}_p u_r + u_r^2 - 2\overline{u}_p\overline{u}_r - {\overline{u}_r}^2)\, dz + O(\mu^2) \\ &= (h+\delta\zeta)\overline{u}^2 + \int_{-h}^{\delta\zeta} (u_r^2 - {\overline{u}_r}^2)\, dz + O(\mu^2) \\ &= \frac{Q^2}{h+\delta\zeta} + \Delta M + O(\mu^2), \end{aligned} \tag{2.44}$$

where $\overline{u}$ and Q are the mean velocity over depth and the total volume flux, respectively. Inside the surf zone, Q includes the contribution from the depth averaged component of the rotational part of the velocity. The momentum deficit ΔM is defined by

$$\Delta M \equiv \int_{-h}^{\delta\zeta} (u_r^2 - {\overline{u}_r}^2)\, dz, \tag{2.45}$$

which is the contribution from the vertical variation of the rotational velocity. Notice that for ΔM, the integration is carried out over the entire water column. The reason for this is that the contribution to u_r from the vorticity is mainly concentrated in the upper flow region. Therefore, evaluating ΔM as

$$\Delta M \equiv \int_{-h}^{0} (u_r^2 - {\overline{u}_r}^2)\, dz$$

would result in an underestimation of the momentum flux due to breaking. Similarly,

$$\begin{aligned}&\int_{-h}^{\delta\zeta} \frac{\partial^2}{\partial x \partial t} \int_z^{\delta\zeta} \frac{\partial}{\partial x} \int_{-h}^{z} u\, dz\, dz\, dz \\ &\qquad = \int_{-h}^{0} \frac{\partial^2}{\partial x \partial t} \int_z^{0} \frac{\partial}{\partial x} \int_{-h}^{z} \overline{u}\, dz\, dz\, dz + (\Delta P)_{xxt} + O(\delta, \mu^2) \\ &\qquad = \frac{h^2}{2} Q_{xxt} - \frac{h^3}{6}\left(\frac{Q}{h}\right)_{xxt} - (\Delta P)_{xxt} + O(\delta, \mu^2), \end{aligned} \tag{2.46}$$

where

$$\Delta P \equiv -\int_{-h}^{\delta\zeta} \int_z^{\delta\zeta} \int_{-h}^{z} (u_r - \overline{u}_r)\, dz\, dz\, dz. \tag{2.47}$$

And finally, if the shear stress is modeled using an eddy viscosity that is independent of z, then

$$\begin{aligned}
D_s &\equiv \int_{-h}^{\delta\zeta} \frac{\partial^2}{\partial x^2} \int_z^{\delta\zeta} \nu_t \frac{\partial u}{\partial z}\, dz\, dz \\
&= \int_{-h}^{\delta\zeta} \frac{\partial^2}{\partial x^2} \nu_t \left[u(\delta\zeta) - u(z)\right]\, dz \\
&= \int_{-h}^{\delta\zeta} \frac{\partial^2}{\partial x^2} \nu_t \left[u_r(\delta\zeta) - u_r(z)\right]\, dz + O(\mu^2) \\
&= (h+\delta\zeta)\frac{\partial^2}{\partial x^2}\left[\nu_t u_r(\delta\zeta)\right] + \delta\frac{\partial\zeta}{\partial x}\frac{\partial}{\partial x}\left[\nu_t u_r(\delta\zeta)\right] + \delta\frac{\partial}{\partial x}\left[\nu_t u_r(\delta\zeta)\frac{\partial\zeta}{\partial x}\right] \\
&\quad - \frac{\partial^2}{\partial x^2}\left[\nu_t \overline{u}_r(h+\delta\zeta)\right]. \qquad (2.48)
\end{aligned}$$

Substituting (2.44), (2.46) and (2.48) in (2.42),

$$\begin{aligned}
&\frac{\partial Q}{\partial t} + (h+\delta\zeta)\frac{\partial\zeta}{\partial x} + \delta\left(\frac{Q^2}{h+\delta\zeta}\right)_x - \mu^2\frac{h^2}{2}Q_{xxt} + \mu^2\frac{h^3}{6}\left(\frac{Q}{h}\right)_{xxt} \\
&\qquad + \delta\left(\Delta M\right)_x + \mu^2\left(\Delta P\right)_{xxt} - \mu^2 D_s = 0. \qquad (2.49)
\end{aligned}$$

Equations (2.8) and (2.49) form the basis of the breaking model for the case of weakly non-linear shoaling and is similar to the equations developed by Yu (1996). However, the dispersion characteristic of this model is very poor for intermediate and deep-water waves. Although it is not possible to obtain any significant improvement in these characteristics without including higher order dispersive terms; a modest improvement can be obtained by enhancing the linear characteristics. This enhancement also leads to a stabilization of the numerical scheme and helps to reduce the high frequency waves generated by the breaking waves. Madsen and Schäffer (1998b) suggested enhancement of the frequency dispersion by applying a linear operator

$$L = 1 + B\mu^2 h^2 \frac{\partial^2}{\partial x^2} \qquad (2.50)$$

on the non-breaking terms in (2.49) and retaining terms of $O(\delta, \mu^2)$. B is a free parameter, chosen such that the dispersion characteristic most closely resemble that of linear theory. Thus, (2.49) becomes

$$\frac{\partial Q}{\partial t} + (h+\delta\zeta)\frac{\partial\zeta}{\partial x} + \delta\left(\frac{Q^2}{h+\delta\zeta}\right)_x + \mu^2\left(B - \frac{1}{2}\right)h^2\left(Q\right)_{xxt} + \mu^2\frac{h^3}{6}\left(\frac{Q}{h}\right)_{xxt}$$

$$+\mu^2 Bh^2\left(h\zeta_x\right)_{xx}+\delta\left(\Delta M\right)_x+\mu^2\left(\Delta P\right)_{xxt}-\mu^2 D_s=O(\delta\mu^2,\mu^4). \tag{2.51}$$

The last three terms in (2.51) depend entirely on the vorticity field in the domain. Thus, in the shoaling region where there is no generation of vorticity, these terms vanish, and (2.51) reduces to the standard Boussinesq equations with dispersion correction. On the other hand, inside the surf zone the vorticity terms are the only signatures of breaking, as vorticity is generated due to the breaking process leading to non-zero contributions from ΔM, ΔP and D_s.

Equations (2.8) and (2.51) together constitute the weakly non-linear, weakly dispersive form, with enhanced dispersion, of the equations for conservation of mass and momentum for the breaking waves.

2.2.2 Fully non-linear breaking model.

As will be seen later, one of the major problems with the weakly non-linear model is the fact that the shoaling is not predicted very well. For accurate predictions in the surf zone, this is a severe limitation. Furthermore, with the weakly non-linear formulation, the Doppler shift associated with waves on a current has to be treated explicitly (see, e.g., Yoon and Liu 1989; Chen *et al.* 1998) which introduces additional terms in the equations.

It has been found by Wei *et al.* (1995) that including the higher order terms in δ in the Boussinesq equations result in a much better prediction of the wave heights close to the breaking region. It also turns out that, if all terms of $O(\mu^2)$ terms are retained (i.e., $\delta\sim O(1)$), then the additional terms needed in the weakly non-linear equations associated with waves on a current are contained in the $O(\delta\mu^2)$ terms of the equations (Kirby 1997; Madsen and Schäffer 1998a).

The continuity equation is exact and hence remains unchanged from (2.8). On the other hand, the momentum equation will have additional terms. The expressions for the terms in the momentum equation were obtained using Maple (Kofler 1997). For this case, where $\delta\sim O(1)$, we choose to use the $\zeta-\overline{u}$ formulation, as this form of the equation become much simpler. Recovery of the $\zeta-Q$ version of the model is fairly trivial since

$$Q=\overline{u}(h+\delta\zeta). \tag{2.52}$$

Thus, the continuity equation is

$$\frac{\partial \zeta}{\partial t} + \frac{\partial}{\partial x}[\overline{u}(h+\delta\zeta)] = 0. \tag{2.53}$$

All terms in the momentum equation (2.23) have to be retained and is restated here for convenience:

$$\begin{aligned}
&\frac{\partial Q}{\partial t} + \delta\frac{\partial}{\partial x}\int_{-h}^{\delta\zeta} u^2\,dz + (h+\delta\zeta)\zeta_x - \mu^2\int_{-h}^{\delta\zeta}\frac{\partial^2}{\partial x\partial t}\int_z^{\delta\zeta}\frac{\partial}{\partial x}\int_{-h}^{z} u\,dz\,dz\,dz \\
&\quad - \delta\mu^2\int_{-h}^{\delta\zeta}\frac{\partial}{\partial x}\left(\frac{\partial}{\partial x}\int_{-h}^{z} u\,dz\right)^2 dz - \mu^2\int_{-h}^{\delta\zeta}\frac{\partial^2}{\partial x^2}\int_z^{\delta\zeta}\nu_t\frac{\partial u}{\partial z}\,dz\,dz \\
&\quad - \delta\mu^2\int_{-h}^{\delta\zeta}\frac{\partial^2}{\partial x^2}\int_z^{\delta\zeta} u\frac{\partial}{\partial x}\int_{-h}^{z} u\,dz\,dz\,dz \\
&\quad = 0,
\end{aligned} \tag{2.54}$$

with u now being given by the full expression

$$u = \overline{u}_p + \mu^2\left(\frac{\Delta_1}{2} - z\right)(h\overline{u}_p)_{xx} + \frac{\mu^2}{2}\left(\frac{\Delta_2}{3} - z^2\right)\overline{u}_{p_{xx}} + u_r. \tag{2.55}$$

The first term in (2.54) is

$$\frac{\partial Q}{\partial t} = (h+\delta\zeta)\frac{\partial \overline{u}}{\partial t} - \overline{u}\frac{\partial}{\partial x}[\overline{u}(h+\delta\zeta)]. \tag{2.56}$$

The value of u^2 is found from (2.37) substituting (2.40) for u_p:

$$\begin{aligned}
u^2 &= {\overline{u}_p}^2 + u_r^2 + 2\mu^2\left(\frac{\Delta_1}{2} - z\right)\overline{u}_p(h\overline{u}_p)_{xx} + \mu^2\left(\frac{\Delta_2}{3} - z^2\right)\overline{u}_p\overline{u}_{p_{xx}} \\
&\quad + 2\mu^2\left(\frac{\Delta_1}{2} - z\right)u_r(h\overline{u}_p)_{xx} + \mu^2\left(\frac{\Delta_2}{3} - z^2\right)u_r\overline{u}_{p_{xx}} + O(\mu^4) \\
&= {\overline{u}_p}^2 + u_r^2 + 2\mu^2\left(\frac{\Delta_1}{2} - z\right)\overline{u}(h\overline{u}_p)_{xx} + \mu^2\left(\frac{\Delta_2}{3} - z^2\right)\overline{u\overline{u}}_{p_{xx}} \\
&\quad + 2\mu^2\left(\frac{\Delta_1}{2} - z\right)(u_r - \overline{u}_r)(h\overline{u}_p)_{xx} + \mu^2\left(\frac{\Delta_2}{3} - z^2\right)(u_r - \overline{u}_r)\overline{u}_{p_{xx}} + O(\mu^4).
\end{aligned} \tag{2.57}$$

Note that the integral over depth of the third and fourth terms in (2.57) is zero. Thus, the convective term in (2.54) is

$$\delta\frac{\partial}{\partial x}\int_{-h}^{\delta\zeta} u^2\,dz = \frac{\partial}{\partial x}[(h+\delta\zeta)\overline{u}^2] + \frac{\partial}{\partial x}\int_{-h}^{\delta\zeta}(u_r^2 - {\overline{u}_r}^2)\,dz$$

$$
\begin{aligned}
&+\frac{\partial}{\partial x}\int_{-h}^{\delta\zeta} 2\mu^2\left(\frac{\Delta_1}{2}-z\right)(u_r-\overline{u}_r)(h\overline{u}_p)_{xx}\,dz\\
&+\frac{\partial}{\partial x}\int_{-h}^{\delta\zeta} \mu^2\left(\frac{\Delta_2}{3}-z^2\right)(u_r-\overline{u}_r)\overline{u}_{p_{xx}}\,dz\\
=&(h+\delta\zeta)\overline{u}\frac{\partial\overline{u}}{\partial x}+\overline{u}\frac{\partial}{\partial x}[\overline{u}(h+\delta\zeta)]+(\Delta M)_x+\mu^2\left(\Delta M_1\right)_x, \qquad (2.58)
\end{aligned}
$$

where

$$
\Delta M_1=-(\overline{u}_p)_{xx}\left[\int_{-h}^{\delta\zeta}(2hz+z^2)(u_r-\overline{u}_r)\,dz\right]+O(h_x) \qquad (2.59)
$$

since

$$
\int_{-h}^{\delta\zeta}(u_r-\overline{u}_r)\,dz=0,
$$

and ΔM is still defined by (2.45). In the fourth and fifth terms of (2.54), which represents the vertical acceleration term, the $O(\mu^2)$ terms in the expression for velocity u lead to $O(\mu^4)$ terms. Retaining terms up to $O(\mu^2)$ gives

$$
u=\overline{u}_p+u_r+O(\mu^2)=\overline{u}+(u_r-\overline{u}_r)+O(\mu^2). \qquad (2.60)
$$

Thus, the fourth term in (2.54) becomes

$$
\begin{aligned}
\int_{-h}^{\delta\zeta}\frac{\partial^2}{\partial x\partial t}\int_{z}^{\delta\zeta}\frac{\partial}{\partial x}\int_{-h}^{z}u\,dz\,dz\,dz=&\int_{-h}^{\delta\zeta}\frac{\partial^2}{\partial x\partial t}\int_{z}^{\delta\zeta}\frac{\partial}{\partial x}\int_{-h}^{z}\overline{u}\,dz\,dz\,dz\\
&+\int_{-h}^{\delta\zeta}\frac{\partial^2}{\partial x\partial t}\int_{z}^{\delta\zeta}\frac{\partial}{\partial x}\int_{-h}^{z}(u_r-\overline{u}_r)\,dz\,dz\,dz\\
&+O(\mu^2). \qquad (2.61)
\end{aligned}
$$

The first component of this term evaluates as

$$
\begin{aligned}
\int_{-h}^{\delta\zeta}\frac{\partial^2}{\partial x\partial t}\int_{z}^{\delta\zeta}\frac{\partial}{\partial x}\int_{-h}^{z}\overline{u}\,dz\,dz\,dz=&\frac{1}{3}(h+\delta\zeta)^3\overline{u}_{xxt}\\
&+(h+\delta\zeta)^2\left[\delta\zeta_{xt}\overline{u}_x+\overline{u}_{xt}h_x+\frac{1}{2}\overline{u}_t h_{xx}+\delta\zeta_x\overline{u}_{xt}+\delta\overline{u}_{xx}\zeta_t\right]\\
&+(h+\delta\zeta)\left[2\delta\zeta_t h_x\overline{u}_x+\delta^2\zeta_x\zeta_t\overline{u}_x+\delta\zeta_x\overline{u}_t h_x+\delta\overline{u}\zeta_{xt}h_x+\delta\overline{u}h_{xx}\zeta_t\right]. \qquad (2.62)
\end{aligned}
$$

Notice that the h_x-terms have been retained in this evaluation. Later, the importance of these terms will be shown negligible for reasonably gentle beaches. Using

the Leibniz rule to bring the derivatives outside the integrals, the second component becomes

$$\begin{aligned}
&\int_{-h}^{\delta\zeta} \frac{\partial^2}{\partial x \partial t} \int_{z}^{\delta\zeta} \frac{\partial}{\partial x} \int_{-h}^{z} (u_r - \overline{u}_r)\, dz\, dz\, dz \\
&\qquad = \frac{\partial^2}{\partial x \partial t} \int_{-h}^{\delta\zeta} \int_{z}^{\delta\zeta} \frac{\partial}{\partial x} \int_{-h}^{z} (u_r - \overline{u}_r)\, dz\, dz\, dz + O(h_x) \\
&\qquad = \frac{\partial^2}{\partial x \partial t} \int_{-h}^{\delta\zeta} \frac{\partial}{\partial x} \int_{z}^{\delta\zeta} \int_{-h}^{z} (u_r - \overline{u}_r)\, dz\, dz\, dz \\
&\qquad = -\left(\Delta P\right)_{xxt} + O(h_x), \qquad (2.63)
\end{aligned}$$

where ΔP, defined by (2.47), is

$$\Delta P = -\int_{-h}^{\delta\zeta} \int_{z}^{\delta\zeta} \int_{-h}^{z} (u_r - \overline{u}_r)\, dz\, dz\, dz.$$

The continuity equation (2.53) is used to eliminate the time derivatives of ζ in (2.62), which gives

$$\begin{aligned}
\int_{-h}^{\delta\zeta} \frac{\partial^2}{\partial x \partial t} \int_{z}^{\delta\zeta} \frac{\partial}{\partial x} \int_{-h}^{z} \overline{u}\, dz\, dz\, dz &= (h+\delta\zeta)^3 \left[\frac{1}{3}\overline{u}_{xxt} - 2\delta \overline{u}_x \overline{u}_{xx}\right] \\
&+ (h+\delta\zeta)^2 \left[\, h_x \overline{u}_{xt} + \frac{1}{2} h_{xx} \overline{u}_t + \delta\zeta_x \overline{u}_{xt} - 2\delta h_x \overline{u}\overline{u}_{xx} - 4\delta h_x \overline{u}_x^2 \right. \\
&\qquad \left. -2\delta h_{xx} \overline{u}\overline{u}_x - \delta^2 \overline{u}\zeta_x \overline{u}_{xx} - 3\delta^2 \zeta_x \overline{u}_x^2 - \delta^2 \zeta_{xx} \overline{u}\overline{u}_x \right] \\
&+ (h+\delta\zeta) \left[-4\delta h_x^2 \overline{u}\overline{u}_x - 2\delta h_x h_{xx} \overline{u}^2 + \delta h_x \zeta_x \overline{u}_t - \delta^2 h_x \zeta_{xx} \overline{u}^2 \right. \\
&\qquad \left. -5\, \delta^2 \zeta_x h_x \overline{u}\overline{u}_x - \delta^2 h_{xx} \zeta_x \overline{u}^2 - \delta^3 \zeta_x^2 \overline{u}\overline{u}_x \right]. \qquad (2.64)
\end{aligned}$$

In the fifth term in (2.54), which represents the contributions from the vertical fluid motion, the $O(\mu^2)$ contributions to u can again be omitted which gives

$$\int_{-h}^{\delta\zeta} \frac{\partial}{\partial x} \left(\frac{\partial}{\partial x} \int_{-h}^{z} u\, dz \right)^2 dz = \int_{-h}^{\delta\zeta} \frac{\partial}{\partial x} \left(\frac{\partial}{\partial x} \int_{-h}^{z} \overline{u}\, dz \right)^2 dz + D_w + O(\mu^2), \quad (2.65)$$

with

$$D_w \equiv \frac{\partial}{\partial x} \int_{-h}^{\delta\zeta} \left[\left(\frac{\partial}{\partial x} \int_{-h}^{z} (u_r - \overline{u}_r)\, dz \right) \frac{\partial}{\partial x} \int_{-h}^{z} (\overline{u} + u_r - \overline{u}_r)\, dz \right] dz. \qquad (2.66)$$

The first part of this term evaluates as

$$\int_{-h}^{\delta\zeta} \frac{\partial}{\partial x} \left(\frac{\partial}{\partial x} \int_{-h}^{z} \overline{u}\, dz \right)^2 dz = \frac{2}{3}(h+\delta\zeta)^3 \overline{u}_x \overline{u}_{xx}$$

$$+ (h+\delta\zeta)^2 \left[\overline{uu}_x h_{xx} + 2\overline{u}_x^2 h_x + \overline{uu}_{xx} h_x\right]$$
$$+ (h+\delta\zeta) \left[2\overline{u}^2 h_x h_{xx} + 4\overline{u} h_x^2 \overline{u}_x\right] + O(\mu^2). \quad (2.67)$$

The turbulent shear stress term remains the same as given before by (2.48). The final term in (2.54), which is the net shear stress along the vertical sides of the water column due to the mean flow, becomes

$$\int_{-h}^{\delta\zeta} \frac{\partial^2}{\partial x^2} \int_z^{\delta\zeta} u \frac{\partial}{\partial x} \int_{-h}^{z} u \, dz \, dz \, dz = \int_{-h}^{\delta\zeta} \frac{\partial^2}{\partial x^2} \int_z^{\delta\zeta} \overline{u} \frac{\partial}{\partial x} \int_{-h}^{z} \overline{u} \, dz \, dz \, dz + D_{uw} + O(\mu^2), \quad (2.68)$$

with

$$D_{uw} \equiv \int_{-h}^{\delta\zeta} \frac{\partial^2}{\partial x^2} \int_z^{\delta\zeta} \left[(u_r - \overline{u}_r) \frac{\partial}{\partial x} \int_{-h}^{z} \overline{u} \, dz + (\overline{u} + u_r - \overline{u}_r) \frac{\partial}{\partial x} \int_{-h}^{z} (u_r - \overline{u}_r) \, dz\right] dz \, dz. \quad (2.69)$$

The first part of this term is

$$\int_{-h}^{\delta\zeta} \frac{\partial^2}{\partial x^2} \int_z^{\delta\zeta} \overline{u} \frac{\partial}{\partial x} \int_{-h}^{z} \overline{u} \, dz \, dz \, dz = (h+\delta\zeta)^3 \left[\overline{u}_x \overline{u}_{xx} + \frac{1}{3}\overline{uu}_{xxx}\right]$$
$$+ (h+\delta\zeta)^2 \left[2\delta\overline{uu}_{xx}\zeta_x + 2(h+\delta\zeta)_x \overline{u}_x^2 + 2\overline{uu}_{xx} h_x + \frac{5}{2}\overline{u} h_{xx} \overline{u}_x + \delta\overline{u}\zeta_{xx}\overline{u}_x + \frac{1}{2}\overline{u}^2 h_{xxx}\right] + (h+\delta\zeta)\left[\delta\overline{u}^2\zeta_{xx}h_x + 6\delta\overline{u}\zeta_x h_x \overline{u}_x + \delta^2\overline{u}\zeta_x^2\overline{u}_x + 2\delta\overline{u}^2 h_{xx}\zeta_x\right] + O(\mu^2). \quad (2.70)$$

Substituting (2.56)-(2.70) into (2.54), the momentum equation becomes

$$\overline{u}_t + \delta\overline{uu}_x + \zeta_x - \mu^2\left[\frac{1}{3}h^2\overline{u}_{xxt} + \frac{1}{2}hh_{xx}\overline{u}_t + hh_x\overline{u}_{xt}\right] + \delta\mu^2\left[-\frac{1}{3}h^2\overline{uu}_{xxx} - h\zeta_x\overline{u}_{xt} + \frac{1}{3}h^2\overline{u}_x\overline{u}_{xx} - \frac{2}{3}h\zeta\overline{u}_{xxt} - \frac{3}{2}hh_{xx}\overline{uu}_x - \frac{1}{2}hh_{xxx}\overline{u}^2 - hh_x\overline{uu}_{xx} - \zeta h_x\overline{u}_{xt} - h_x\zeta_x\overline{u}_t - \frac{1}{2}\zeta h_{xx}\overline{u}_t\right] + \delta^2\mu^2\left[\frac{1}{6}\zeta^2\overline{u}_{xxt} - \frac{1}{3}h\zeta\overline{u}_x\overline{u}_{xx} - \frac{1}{3}h\overline{u}_{xx}(\zeta\overline{u})_x + h\left(\zeta\overline{u}_x^2\right)_x - \frac{1}{2}\left(\zeta^2\overline{u}_{xt}\right)_x - \frac{2}{3}h\left(\zeta\overline{uu}_{xx}\right)_x - \zeta_x h_{xx}\overline{u}^2 - \zeta h_x\overline{uu}_{xx} - \frac{1}{2}\zeta h_{xxx}\overline{u}^2 - \frac{3}{2}\zeta h_{xx}\overline{uu}_x - \zeta_x h_x\overline{uu}_x\right] + \delta^3\mu^2\left[-\frac{1}{3}\zeta^2\overline{uu}_{xxx} - \zeta\zeta_x\overline{uu}_{xx} + \zeta\zeta_x\overline{u}_x^2\right.$$

$$+\frac{1}{3}\zeta^2\overline{u}_x\overline{u}_{xx}\Big] + \left[\delta\left(\Delta M\right)_x + \mu^2\left(\Delta P\right)_{xxt} - \mu^2 D_s + \delta\mu^2\left(\Delta M_1\right)_x\right.$$
$$\left.+\delta\mu^2 D_w + \delta\mu^2 D_{uw}\right]\left(h+\delta\zeta\right)^{-1} = O(\mu^4). \tag{2.71}$$

The linear dispersion characteristic of this model is the same as that of the weakly non-linear model described in the previous subsection. As before, the enhancement of the dispersion characteristics is obtained by applying the linear operator given by (2.50). This leads to the enhanced momentum equation

$$\begin{aligned}
&\overline{u}_t + \delta\overline{u}\overline{u}_x + \zeta_x + \mu^2\left[\left(B-\frac{1}{3}\right)h^2\overline{u}_{xxt} - \frac{1}{2}hh_{xx}\overline{u}_t - hh_x\overline{u}_{xt}\right] + B\mu^2h^2\zeta_{xxx}\\
&+\delta\mu^2\left[-\frac{1}{3}h^2\overline{u}\overline{u}_{xxx} - h\zeta_x\overline{u}_{xt} + \frac{1}{3}h^2\overline{u}_x\overline{u}_{xx} - \frac{2}{3}h\zeta\overline{u}_{xxt} - \frac{3}{2}hh_{xx}\overline{u}\overline{u}_x\right.\\
&\left.-\frac{1}{2}hh_{xxx}\overline{u}^2 - hh_x\overline{u}\overline{u}_{xx} - \zeta h_x\overline{u}_{xt} - h_x\zeta_x\overline{u}_t - \frac{1}{2}\zeta h_{xx}\overline{u}_t + Bh^2\left(\overline{u}\overline{u}_x\right)_{xx}\right]\\
&+\delta^2\mu^2\left[\frac{1}{6}\zeta^2\overline{u}_{xxt} - \frac{1}{3}h\zeta\overline{u}_x\overline{u}_{xx} - \frac{1}{3}h\overline{u}_{xx}\left(\zeta\overline{u}\right)_x + h\left(\zeta\overline{u}_x^2\right)_x - \frac{1}{2}\left(\zeta^2\overline{u}_{xt}\right)_x\right.\\
&\left.-\frac{2}{3}h\left(\zeta\overline{u}\overline{u}_{xx}\right)_x - \zeta_x h_{xx}\overline{u}^2 - \zeta h_x\overline{u}\overline{u}_{xx} - \frac{1}{2}\zeta h_{xxx}\overline{u}^2 - \frac{3}{2}\zeta h_{xx}\overline{u}\overline{u}_x - \zeta_x h_x\overline{u}\overline{u}_x\right]\\
&+\delta^3\mu^2\left[-\frac{1}{3}\zeta^2\overline{u}\overline{u}_{xxx} - \zeta\zeta_x\overline{u}\overline{u}_{xx} + \zeta\zeta_x\overline{u}_x^2 + \frac{1}{3}\zeta^2\overline{u}_x\overline{u}_{xx}\right] + \left[\delta\left(\Delta M\right)_x + \mu^2\left(\Delta P\right)_{xxt}\right.\\
&\left.-\mu^2 D_s + \delta\mu^2\left(\Delta M_1\right)_x + \delta\mu^2 D_w + \delta\mu^2 D_{uw}\right]\left(h+\delta\zeta\right)^{-1} = O(\mu^4).
\end{aligned} \tag{2.72}$$

The continuity equation (2.53) along with the momentum equation (2.72) form the fully non-linear (up to $O(\mu^2)$) Boussinesq type model which includes the breaking characteristics of the waves.

2.3 Stokes-type analysis for horizontal bottom.

The characteristics of the various formulations of the Boussinesq type models on a horizontal bottom and in the shoaling region have been analyzed extensively by various researchers (see, e.g., Madsen and Sørensen 1993; Wei and Kirby 1998; Madsen and Schäffer 1998a; Gobbi *et al.* 1999). The analyses include linear shoaling properties, energy transfer to the higher harmonics, triad interactions and wave-current interactions. In this study, the primary focus is on modeling the shallow

water breaking waves and therefore an extensive analysis of the deep-water characteristics is not performed. The analysis below shows some of the shallow water characteristics (before breaking) of the model described above.

Stokes-type perturbation analysis has been utilized by various researchers (see, e.g., Madsen and Sørensen 1993; Madsen and Schäffer 1998a; Gobbi *et al.* 1999) to analyze the behavior of the equations of wave propagation. For shallow water models such as the Boussinesq type models, it has become customary to perform such an analysis to establish the deep-water limit of applicability of the particular form of the equations. Furthermore, although the Stokes theory is known not to be particularly suited to describe shallow water waves, it provides a clear indication of how the different formulations of the Boussinesq equations differ from each other.

A perturbation approach yields expressions for the amplitudes of the second and third harmonics as well as that of the amplitude correction to the linear dispersion for the particular set of equations. These are then compared to the results from the third-order Stokes theory. Madsen and Schäffer (1998b) as well as Gobbi *et al.* (1999) show that retaining terms up to $O(\mu^4)$ result in an extended domain of applicability (up to $kh \sim 6$) for the Boussinesq type equations. Further, they also show that such a model is more accurate in the shallow water regime than a model which only retains terms up to $O(\mu^2)$.

In the present case, the primary interest was in modeling of breaking waves in shallow water. Hence, only terms up to $O(\mu^2)$ have been retained. On the other hand, it is still relevant to establish the region of validity for the sets of equations under consideration here. It is also noted that in order for the Stokes approximation to be valid, this type of analysis is actually based on the assumption that $O(\delta) \ll 1$ and $\mu^2 \sim O(1)$.

The Stokes third-order theory for regular waves gives the water surface elevation as

$$\zeta = a_1 \cos\theta + \delta a_2 \cos 2\theta + \delta^2 a_3 \cos 3\theta, \tag{2.73}$$

where $\theta = kx - \omega t$, a_1 is the amplitude of the primary wave, a_2 is the amplitude of the second harmonic and a_3 is the amplitude of the third harmonic. The first-order

dispersion relation is the one given by linear theory, which in non-dimensional form is

$$\frac{\omega_0^2}{k^2 h} = \frac{\tanh \kappa}{\kappa}, \tag{2.74}$$

where $\kappa = \mu k h$. The Padé [2,2] expansion for (2.74) (Madsen and Schäffer 1998a) is

$$\frac{\omega_0^2}{k^2 h} = \frac{1 + \frac{1}{15}\kappa^2}{1 + \frac{2}{5}\kappa^2}. \tag{2.75}$$

The results of the third-order Stokes theory are (Skjelbreia and Hendrickson 1961; Whitham 1974)

$$a_2 = \frac{1}{4}\frac{a_1^2}{h}\kappa \coth\kappa(3\coth^2\kappa - 1), \tag{2.76a}$$

$$a_3 = \frac{3}{64}\frac{a_1^3}{h^2}\kappa^2 \frac{(1 + 8\coth^6\kappa)}{\sinh^6\kappa}, \tag{2.76b}$$

$$\omega_{13} = \frac{1}{16}\frac{a_1^2}{h^2}\kappa^2 \frac{(9\tanh^4\kappa - 10\tanh^2\kappa + 9)}{\tanh^4\kappa}, \tag{2.76c}$$

where ω_{13} is the third order amplitude correction to the first order dispersion relation, so that the dispersion relation reads

$$\omega = \omega_0(1 + \delta^2\omega_{13}). \tag{2.76d}$$

The series expansions for a_2, a_3 and ω_{13} from $\kappa = 0$ obtained from (2.76a)-(2.76c) are

$$a_2 = \frac{3}{4}\frac{a_1^2}{h}\frac{1}{\kappa^2}\left(1 + \frac{2}{3}\kappa^2 + \frac{7}{45}\kappa^4 + O(\kappa^6)\right), \tag{2.77a}$$

$$a_3 = \frac{27}{64}\frac{a_1^3}{h^2}\frac{1}{\kappa^4}\left(1 + \frac{5}{3}\kappa^2 + \frac{64}{45}\kappa^4 + O(\kappa^6)\right), \tag{2.77b}$$

$$\omega_{13} = \frac{9}{16}\frac{a_1^2}{h^2}\frac{1}{\kappa^2}\left(1 + \frac{2}{9}\kappa^2 + \frac{113}{135}\kappa^4 + O(\kappa^6)\right). \tag{2.77c}$$

For the Boussinesq type equations, following the procedure given by Madsen and Schäffer (1998b), weakly non-linear solutions of the form

$$\zeta = a_1\cos\theta + \delta a_2\cos 2\theta + \delta^2 a_3\cos 3\theta, \tag{2.78a}$$

$$U = u_1\cos\theta + \delta u_2\cos 2\theta + \delta^2 u_3\cos 3\theta \tag{2.78b}$$

are sought. U stands for the volume flux in the weakly non-linear equations and the depth-averaged velocity in the fully non-linear equations.

2.3.1 Analysis of the weakly non-linear equations.

The continuity and momentum equations for the case of no wave breaking and horizontal bottom is, from (2.8) and (2.51),

$$\zeta_t + Q_x = 0, \tag{2.79a}$$

$$Q_t + (h + \delta\zeta)\zeta_x + \delta\left(\frac{Q^2}{h}\right)_x + \mu^2\left(B - \frac{1}{3}\right)h^2 Q_{xxt} + \mu^2 B h^3 \zeta_{xxx} = O(\delta^2, \delta\mu^2). \tag{2.79b}$$

Substituting (2.78) into (2.79) results in the following asymptotic system of equations in δ:

$$(u_1 k - a_1\omega)\sin\theta + 2\delta\,(u_2 k - a_2\omega)\sin 2\theta + 3\delta^2\,(u_3 k - a_3\omega)\sin 3\theta = O(\delta^3), \tag{2.80a}$$

$$\begin{aligned}
&\left[u_1\omega - a_1 kh - \left(B - \frac{1}{3}\right)\mu^2 u_1\omega\mu^2 k^2 h^2 + B a_1 \mu^2 k^3 h^3\right]\sin\theta \\
&+ \delta\left[2u_2\omega - 8\left(B - \frac{1}{3}\right)u_2\omega\mu^2 k^2 h^2 - 2a_2 kh + 8B a_2\mu^2 k^3 h^3 - u_1\frac{k}{h} - \frac{1}{2}a_1^2 k\right]\sin 2\theta \\
&+ \delta^2\left\{\left[3u_3\omega - 3a_3 kh + 27B a_3\mu^2 k^3 h^3 - 27B u_3\omega\mu^2 k^2 h^2 - 3u_1 u_2\frac{k}{h} - \frac{3}{2}a_1 a_2 k\right.\right. \\
&\left.\left. + 9u_2\omega\mu^2 k^2 h^2 + \frac{3}{4}a_1 u_1^2\frac{k}{h^2}\right]\sin 3\theta + \left[-u_1 u_2\frac{k}{h} + \frac{3}{4}u_1^2 a_1\frac{k}{h^2} - \frac{1}{2}a_1 a_2 k\right]\sin\theta\right\} \\
&= O(\delta^3).
\end{aligned} \tag{2.80b}$$

The coefficients of the powers of δ in (2.80a) gives the relation between u_1, u_2, u_3 and a_1, a_2, a_3. Substituting these relations in (2.80b) and equating like powers in δ gives, at the lowest order, the linear dispersion relation

$$\frac{\omega_0^2}{k^2 h} = \frac{1 - B\kappa^2}{1 - \left(B - \frac{1}{3}\right)\kappa^2}. \tag{2.81}$$

Comparing this result with (2.75) indicates that $B = -1/15$ gives an exact match between the result from the Boussinesq theory and the Padé [2,2] approximation of the result from the Stokes linear theory. Figure 2.1 shows the ratio of the result from the Boussinesq theory and the exact result given by (2.74) for the case of $B = 0$ and for $B = -1/15$. It is evident that $B = -1/15$ does indeed yield a much better

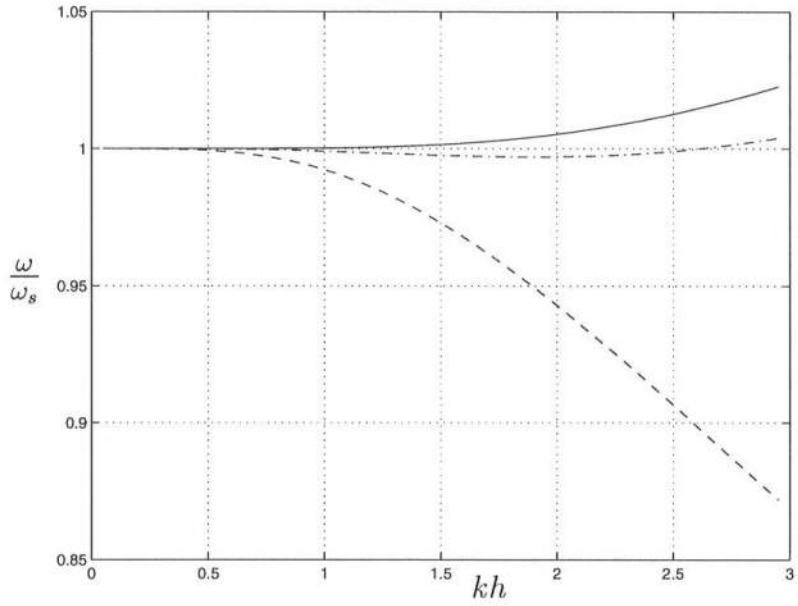

Figure 2.1: Ratio of the linear dispersion relation from the Boussinesq equations to the linear theory for $B = 0$ (– – –), $B = -1/15$ (———) and for Nwogu (1993) (–·–·–).

agreement. At $kh = 3$, the error is only about 2% whereas for the classical version of the Boussinesq equation where $B = 0$, the error is about 13%.

The figure also shows the linear dispersion relation for the extended formulation of Nwogu (1993) which is a different form of the Boussinesq equations. This model is based on the velocity u_α at the reference depth z_α in the water column. The reference depth is chosen such that the dispersion relation most closely approximates the dispersion relation using linear theory. The linear dispersion relation given by the $\zeta - u_\alpha$ model is

$$\frac{\omega_0^2}{k^2 h} = \frac{1 - (\alpha + 1/3)\kappa^2}{1 - \alpha\kappa^2}, \tag{2.82}$$

where $\alpha = z_\alpha^2/2 + z_\alpha = -0.39$ yields the best fit to the linear dispersion relation. This relation is also valid for the fully non-linear model of Wei *et al.* (1995). It is seen that the dispersion characteristics of the $\zeta - u_\alpha$ model is better than that of the $\zeta - \overline{u}$ model. Further improvements to the dispersion characteristics of both models

can be obtained by retaining terms up to $O(\mu^4)$ (Madsen and Schäffer 1998a; Gobbi *et al.* 1999).

At $O(\delta)$, (2.80b) gives the amplitude of the second harmonic as

$$a_2 = \frac{3}{4}\frac{a_1^2}{h}\frac{1}{\kappa^2}\left[1 + \left(\frac{1}{9} - B\right)\kappa^2\right]. \tag{2.83}$$

At $O(\delta^2)$ in (2.80b), secular terms exist. These terms are eliminated by accounting for the amplitude correction to the dispersion relation as given by (2.76d), which gives

$$\omega_{13} = \frac{9}{16}\frac{a_1^2}{h^2}\frac{1}{\kappa^2}\left[\frac{1 + 2\left(\frac{1}{9} - B\right)\kappa^2 + \left(\frac{1}{9} - B\right)^2\kappa^4}{1 + \left(\frac{1}{3} - 2B\right)\kappa^2 + B\left(B - \frac{1}{3}\right)\kappa^4}\right]. \tag{2.84}$$

The series expansion, with $B = -1/15$ reads

$$\omega_{13} = \frac{9}{16}\frac{a_1^2}{h^2}\frac{1}{\kappa^2}\left(1 - \frac{1}{9}\kappa^2 + \frac{23}{405}\kappa^4\right). \tag{2.85}$$

Finally, the non-secular terms give

$$a_3 = \frac{27}{64}\frac{a_1^3}{h^2}\frac{1}{\kappa^4}\left[1 + 2\left(\frac{1}{9} - B\right)\kappa^2 + \left(\frac{1}{9} - B\right)^2\kappa^4\right]. \tag{2.86}$$

Comparing (2.83), (2.85) and (2.86) for $B = -1/15$ to the Stokes solutions given by (2.77) show that the results from the Boussinesq equations are correct only to the lowest order. The coefficients of κ^2 are significantly smaller for all cases (see also Madsen and Sørensen 1993).

Figure 2.2 shows the comparisons between the full expressions for the weakly non-linear case and the results from the Stokes expansion, for the case of $B = 0$. For $kh \simeq 0.5$, the error, when compared to the third order Stokes theory, in the estimate of a_2 and a_3 is about 15% and for ω_{13} it is about 30%. This implies that the energy transferred to the higher harmonics will be significantly less in the case of the weakly non-linear Boussinesq equations. The magnitudes of the errors increase dramatically for waves in deeper water. No significant improvement in the non-linear characteristics is noticed even for the enhanced ($B = -1/15$) weakly non-linear equations (figure 2.3). It should be noted here that the non-linear characteristics of

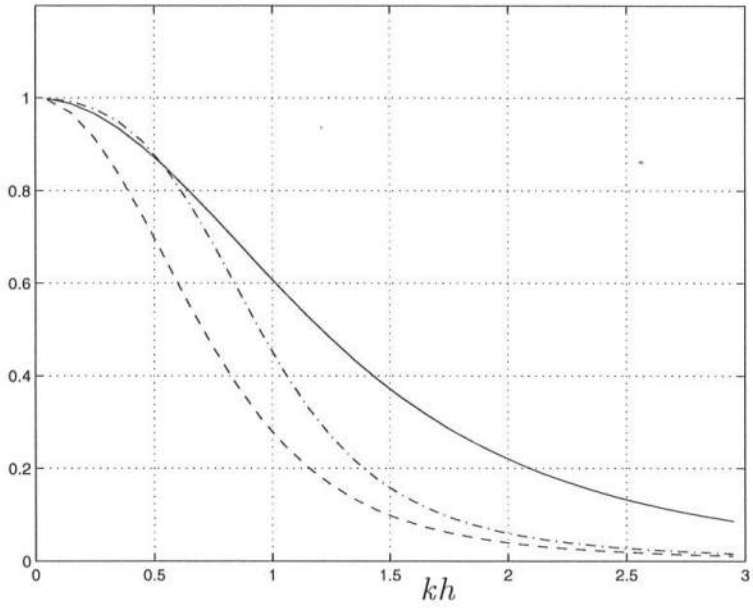

Figure 2.2: Non-Linear characteristics of the weakly non-linear Boussinesq equations in comparison to the third order Stokes theory. a_2/a_2^s (———), a_3/a_3^s (– – –) and $\omega_{13}/\omega_{13}^s$ (–·–·–).

the weakly non-linear $\zeta - Q$ model differ substantially from that of the weakly non-linear $\zeta - \overline{u}$ model, which have also been derived by Madsen and Schäffer (1998b). The perturbation analysis of the enhanced weakly non-linear $\zeta - \overline{u}$ model give the expressions

$$a_2 = \frac{3}{4}\frac{a_1^2}{h}\frac{1}{\kappa^2}\left[1 + \frac{17}{15}\kappa^2 + \frac{16}{225}\kappa^4\right], \tag{2.87a}$$

$$a_3 = \frac{27}{64}\frac{a_1^3}{h^2}\frac{1}{\kappa^4}\left[1 + \frac{142}{45}\kappa^2 + \frac{1483}{675}\kappa^4 + O(\kappa^6)\right], \tag{2.87b}$$

$$\omega_{13} = \frac{9}{16}\frac{a_1^2}{h^2}\frac{1}{\kappa^2}\left[1 + \frac{5}{9}\kappa^2 + \frac{14}{225}\kappa^4 + O(\kappa^6)\right]. \tag{2.87c}$$

2.3.2 Analysis of the fully non-linear equations.

We proceed as in the previous case and look for a perturbation solution that result in an asymptotic system of equations. Only the results are shown for this case. Substituting (2.78) into (2.53) and (2.72), omitting the terms which describe

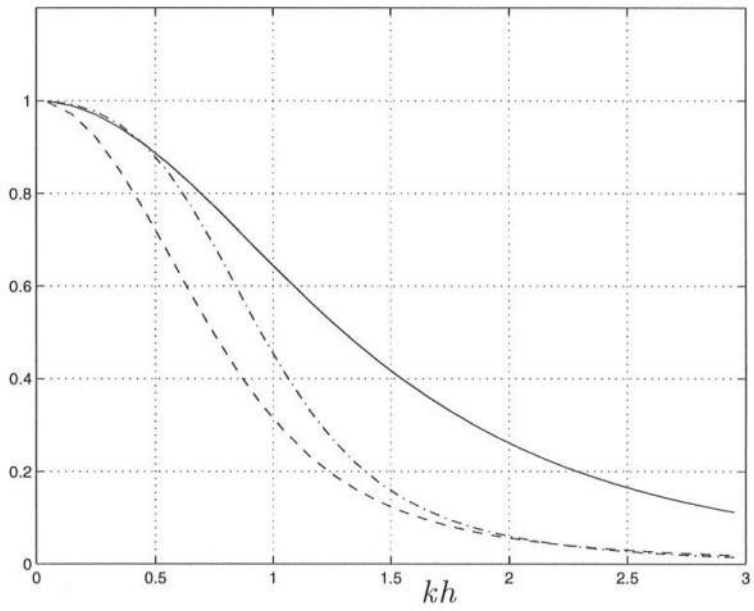

Figure 2.3: Non-Linear characteristics of the enhanced weakly non-linear Boussinesq equations in comparison to the third order Stokes theory. a_2/a_2^s (———), a_3/a_3^s (– – –) and $\omega_{13}/\omega_{13}^s$ (–·–·–).

breaking, and proceeding as before yields the second and third order characteristics as

$$a_2 = \frac{3}{4}\frac{a_1^2}{h}\frac{1}{\kappa^2}\left[1 + \left(\frac{1}{3} - 5B\right)\kappa^2 + \left(4B^2 - \frac{1}{3}B\right)\kappa^4\right], \tag{2.88a}$$

$$a_3 = \frac{27}{64}\frac{a_1^3}{h^2}\frac{1}{\kappa^4}\left[1 + \left(\frac{2}{3} - 15B\right)\kappa^2 + \left(\frac{1}{9} - \frac{35}{9}B + 63B^2\right)\kappa^4 + O(\kappa^6)\right], \tag{2.88b}$$

$$\omega_{13} = \frac{9}{16}\frac{a_1^2}{h^2}\frac{1}{\kappa^2}\left[\frac{1 + \left(\frac{2}{9} - 6B\right)\kappa^2 + \left(\frac{7}{27} - \frac{17}{9}B + 9B^2\right)\kappa^4 + O(\kappa^6)}{1 + \left(\frac{1}{3} - B\right)\kappa^2}\right], \tag{2.88c}$$

With $B = 0$, which corresponds to the fully non-linear Boussinesq model based on $\overline{u}$, the series expansions for (2.88) around $\kappa = 0$ are

$$a_2 = \frac{3}{4}\frac{a_1^2}{h}\frac{1}{\kappa^2}\left[1 + \frac{1}{3}\kappa^2\right], \tag{2.89a}$$

$$a_3 = \frac{27}{64}\frac{a_1^3}{h^2}\frac{1}{\kappa^4}\left[1 + \frac{2}{3}\kappa^2 + \frac{1}{9}\kappa^4 + O(\kappa^6)\right], \tag{2.89b}$$

$$\omega_{13} = \frac{9}{16}\frac{a_1^2}{h^2}\frac{1}{\kappa^2}\left[1 - \frac{1}{9}\kappa^2 + \frac{8}{27}\kappa^4 + O(\kappa^6)\right]. \tag{2.89c}$$

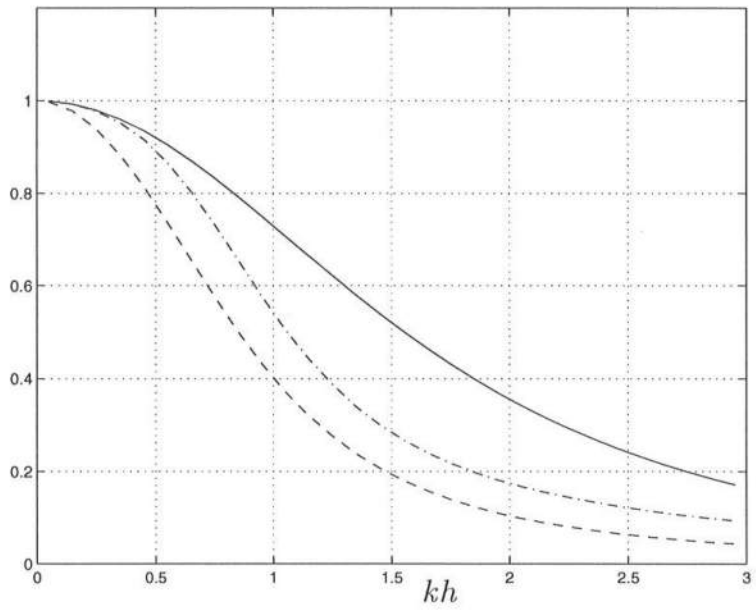

Figure 2.4: Non-Linear characteristics of the fully non-linear Boussinesq equations in comparison to the third order Stokes theory. a_2/a_2^s (———), a_3/a_3^s (– – –) and $\omega_{13}/\omega_{13}^s$ (–·–·–).

Comparing to the Stokes results given by (2.77), it is seen that the results from the fully non-linear equations are slightly better than that from the weakly non-linear equations even though formally they are accurate only up to the lowest order. This is illustrated in figure 2.4 which show the comparisons between the full expressions given by (2.88) for the case of $B = 0$ and (2.77). For $kh \simeq 0.5$, the error now in the estimate of a_2 is about 8%, of a_3, about 12% and of ω_{13}, a little more than 20%. In effect, the error is about halved for smaller values of kh when using the fully non-linear version (up to $O(\mu^2)$) of the Boussinesq equations even without the enhancement. Madsen and Schäffer (1998a) show results for the case when only terms up to $O(\delta\mu^2)$ are retained. The variations of a_2, a_3 and ω_{13} are quite similar. However, slightly better results are obtained by retaining the $O(\delta^2\mu^2)$ terms. Also worth mentioning is the fact that the $O(\delta^3\mu^2)$ terms in the equations do not enter

into the analysis here. These terms only contribute to the fourth harmonic (a_4) which is not considered here.

With $B = -1/15$, the series expansions for (2.88) become

$$a_2 = \frac{3}{4}\frac{a_1^2}{h}\frac{1}{\kappa^2}\left[1 + \frac{2}{3}\kappa^2 + \frac{1}{25}\kappa^4\right], \tag{2.90a}$$

$$a_3 = \frac{27}{64}\frac{a_1^3}{h^2}\frac{1}{\kappa^4}\left[1 + \frac{5}{3}\kappa^2 + \frac{439}{675}\kappa^4 + O(\kappa^6)\right], \tag{2.90b}$$

$$\omega_{13} = \frac{9}{16}\frac{a_1^2}{h^2}\frac{1}{\kappa^2}\left[1 + \frac{2}{9}\kappa^2 + \frac{227}{675}\kappa^4 + O(\kappa^6)\right]. \tag{2.90c}$$

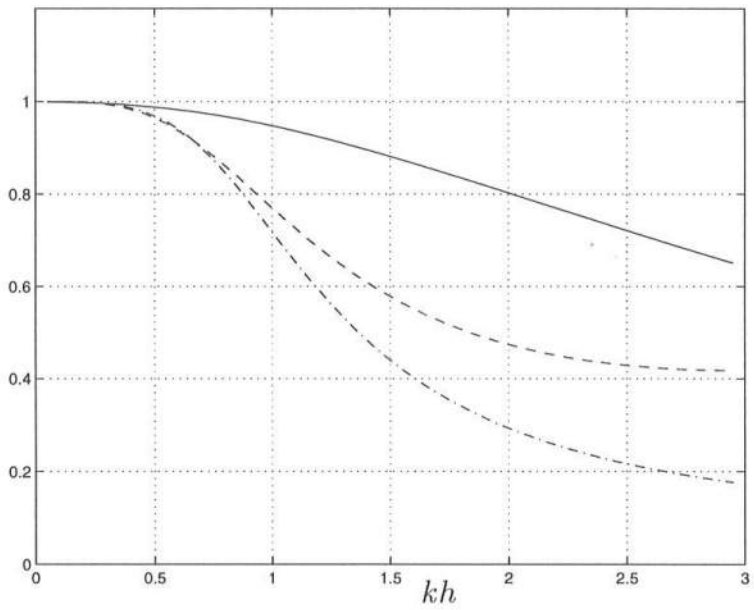

Figure 2.5: Non-Linear characteristics of the enhanced fully non-linear Boussinesq equations in comparison to the third order Stokes theory. a_2/a_2^s (———), a_3/a_3^s (– – –) and $\omega_{13}/\omega_{13}^s$ (–·–·–).

The results from the enhanced equations are formally accurate up to $O(\kappa^2)$. Figure 2.5 show the comparisons between the full expressions given by (2.88) for the case of $B = -1/15$ and (2.77). In this case, the agreement is very good up to $kh \leq 0.5$, with the error reaching only about 5% even for ω_{13}. In contrast to the situation for the weakly non-linear equations, there is a significant improvement in the second and third order solutions.

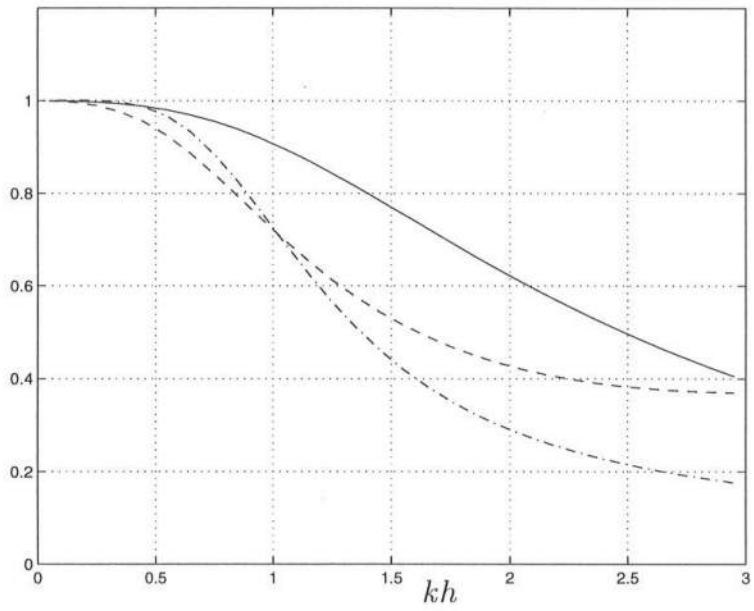

Figure 2.6: Non-Linear characteristics of the enhanced fully non-linear Boussinesq equations (without using continuity equation to replace ζ_t in the momentum equations) in comparison to the third order Stokes theory. a_2/a_2^s (———), a_3/a_3^s (– – –) and $\omega_{13}/\omega_{13}^s$ (–·–·–).

The applicability of the analysis can be pointed out effectively by considering the fully non-linear momentum equation when the time derivatives of ζ are retained in (2.62). Mathematically, the resulting equation is exactly equivalent to (2.53). However, the perturbation analysis for the enhanced equations ($B = -1/15$) gives

$$a_2 = \frac{3}{4}\frac{a_1^2}{h}\frac{1}{\kappa^2}\left[1 + \frac{28}{45}\kappa^2 + \frac{1}{27}\kappa^4\right], \tag{2.91a}$$

$$a_3 = \frac{27}{64}\frac{a_1^3}{h^2}\frac{1}{\kappa^4}\left[1 + \frac{23}{15}\kappa^2 + \frac{1177}{2025}\kappa^4 + O(\kappa^6)\right], \tag{2.91b}$$

$$\omega_{13} = \frac{9}{16}\frac{a_1^2}{h^2}\frac{1}{\kappa^2}\left[1 + \frac{4}{15}\kappa^2 + \frac{119}{405}\kappa^4 + O(\kappa^6)\right]. \tag{2.91c}$$

In this case, the results are very different from (2.90). The coefficients of κ^2, although very close to that in (2.77), are formally wrong. Figure 2.6 show the results. It is obvious that the higher order results (especially for a_2) have much larger errors than that is seen in figure 2.5. Thus, the form of the equations influences the results

drastically. Therefore, it stands to reason that deep-water characteristics of the model can be improved by modifying the form of the equations in a mathematically consistent manner. Such improvements have been obtained for Boussinesq equations accurate to $O(\mu^4)$ by Madsen and Schäffer (1998a).

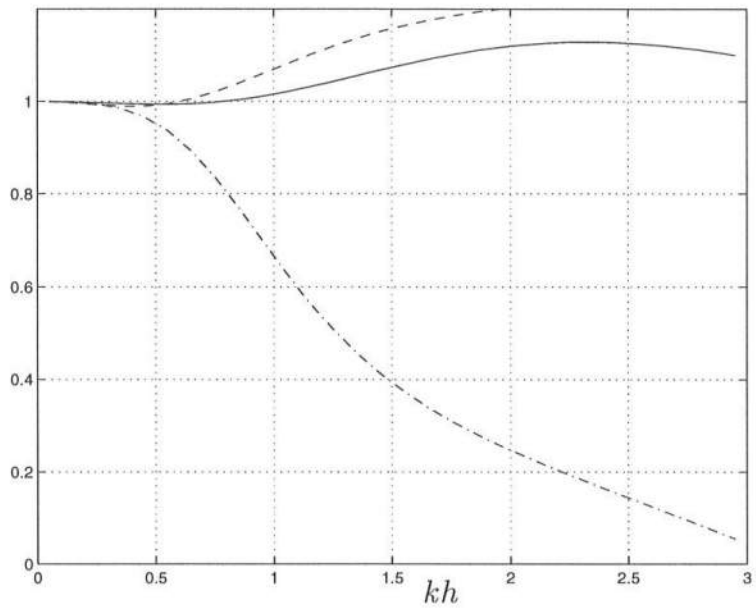

Figure 2.7: Non-linear characteristics of the Wei *et al.* (1995) equations in comparison to the third order Stokes theory. a_2/a_2^s (———), a_3/a_3^s (– – –) and $\omega_{13}/\omega_{13}^s$ (–·–·–).

Finally, figure 2.7 show the results from the fully non-linear model of Wei *et al.* (1995). This model, as mentioned before, is based on the $\zeta - u_\alpha$ formulation, where u_α is the velocity at some location inside the water column. This location is chosen such that the linear dispersion characteristic matches that given by linear wave theory as closely as possible (figure 2.1). For this model, the energy transfer to the higher harmonics is larger than that predicted by the Stokes third order theory and the amplitude correction to the dispersion relation is smaller.

Figures 2.2-2.7 show that the $\zeta - Q$ and the $\zeta - \overline{u}$ versions of the Boussinesq equations transfer less energy to the higher harmonics than the $\zeta - u_\alpha$ version. The consequence of this is that the shoaling of the waves is under-predicted by the present

model and is over-predicted by the Wei *et al.* (1995) model. However, as shall be seen later for the fully non-linear equations, this inaccuracy in the representation of the shoaling waves is very small even at the location where breaking starts in shallow water.

Chapter 3

EVALUATION OF THE BREAKING TERMS.

In the previous chapter, the governing equations that describe waves which shoal and break were derived. The terms in the equations specific to the breaking process are functions of the vorticity generated by the breaking waves. The distribution of vorticity has to be determined before these terms can be evaluated.

The process of breaking for quasi-steady breakers has been documented by Lin and Rockwell (1994). It was found that the breaking causes an abrupt change in the slope of the free surface at the toe of the "roller". In this region, there is a sudden change in the velocity profile, which represents a change from the flow in the interior region of the wave. The discontinuous slope of the free surface, along with the flow separation serves as a source of vorticity. Essentially, we can say that the vorticity is generated by the "roller", which rides along on the front side of the wave crest. This vorticity then spreads downward and backward in the water column to the interior region of the wave. This spreading results in an increase in the magnitude of the instantaneous orbital velocities, especially in the front part of the wave. The equation that describes this process is the vorticity transport equation, which can be solved if the proper boundary conditions can be specified.

Yu (1996) arrived at a parameterized vorticity distribution based on the measurements of Lin and Rockwell (1994) for the vorticity in a spilling breaker. This distribution was then applied at the mean water line. While consistent with the Boussinesq approximation, this turns out to be a major source of inaccuracy. Furthermore, the measurements of Lin and Rockwell (1994) give only a few instantaneous vorticity patterns for a quasi-steady roller, which is not enough for a reliable calculation of the ensemble averaged vorticity in the breaking wave. A numerical

calibration, which is likely to depend on different wave conditions, was therefore used to determine the magnitude of the vorticity at the boundary.

Ideally, a larger set of measurements for multiple wave conditions is necessary to avoid these problems. At present, such a data set is lacking. Therefore other methods have to be used to obtain the boundary condition for the vorticity.

When viewed in a coordinate system moving at the wave speed, we do know that breaking waves have flow patterns, especially around the roller region, that are very similar to that observed in hydraulic jumps (see, e.g., Peregrine and Svendsen 1978; Madsen and Svendsen 1983; Svendsen and Madsen 1984). The absolute velocities and the bottom boundary layer would of course be different under this coordinate transformation. On the other hand, the turbulent stresses, the surface profile, the velocity profile and the vorticity do not change with the change in coordinate system.

One of the difficulties has been to obtain reliable measurements of the flow inside the jump, which, particularly in the turbulent front, usually includes strong entrainment of air bubbles. One of the pioneering studies by Rouse *et al.* (1959) bypassed this problem by conducting the measurements in a wind tunnel in which the free surface was replaced by a smooth wall with the shape of the mean water surface in a jump. Though this also removed the important effect of gravity and surface penetrating turbulence, the study gave useful results and insights, and its careful analysis of the measurements set the standards for many later investigations. Rouse *et al.* (1959) used the then novel technique of hot wire anemometry. Later, improved versions of this experimental technique made it possible to also obtain measurements in real jumps in water (see Resch and Leutheusser 1972; Resch *et al.* 1976).

Also, Laser Doppler Velocimetry has been used both in regular hydraulic jumps (Kirby *et al.* 1995) and in the closely related problem of breaking waves trailing hydrofoils (Battjes and Sakai 1981). The technique of Particle Image Velocimetry (PIV) was pioneered for waves breaking behind an airfoil by Duncan (1981) and later used for the same problem by Lin and Rockwell(1994, 1995), and for the flow far downstream of a hydraulic jump by Hornung *et al.* (1995).

The similarity between hydraulic jumps and breaking waves was the original motivation for the experiments of Bakunin (1995). Since this similarity only exists for jumps of relatively small Froude number, the experiments were carried out for relatively weak jumps with $\mathcal{F} = 1.38$, 1.46 and 1.56. Thus, these measurements provide an excellent set of data from which the breaking wave parameters can be obtained.

In this chapter, the vorticity transport equation is derived in section 3.1 and the solution method is described. The experimental setup for the measurements in the hydraulic jumps is briefly described in section 3.2 along with some of the basic analysis of the experimental results. The final section of the chapter discusses the results for the roller thickness, the shear stresses, the vorticity and the eddy viscosity in the jumps. A more detailed analysis can be found in Svendsen *et al.* (1998).

3.1 The 2-D vorticity transport equation.

The Reynolds equations in two dimensions are

$$\frac{\partial \hat{u}}{\partial \hat{t}} + \hat{u}\frac{\partial \hat{u}}{\partial \hat{x}} + \hat{w}\frac{\partial \hat{u}}{\partial \hat{z}} = -\frac{1}{\rho}\frac{\partial \hat{p}}{\partial \hat{x}} + \frac{1}{\rho}\left(\frac{\partial \hat{\tau}_{xx}}{\partial \hat{x}} + \frac{\partial \hat{\tau}_{zx}}{\partial \hat{z}}\right), \tag{3.1a}$$

$$\frac{\partial \hat{w}}{\partial \hat{t}} + \hat{u}\frac{\partial \hat{w}}{\partial \hat{x}} + \hat{w}\frac{\partial \hat{w}}{\partial \hat{z}} = -\frac{1}{\rho}\frac{\partial \hat{p}}{\partial \hat{z}} + \frac{1}{\rho}\left(\frac{\partial \hat{\tau}_{xz}}{\partial \hat{x}} + \frac{\partial \hat{\tau}_{zz}}{\partial \hat{z}}\right), \tag{3.1b}$$

where $\hat{u}$ and $\hat{w}$ are the ensemble averaged horizontal and vertical velocities, $\hat{p}$ is the ensemble averaged pressure and $\hat{\tau}_{xz}$ and $\hat{\tau}_{zz}$ are the Reynolds stresses based on the ensemble averaged velocities. If we express the Reynolds stress $\hat{\tau}_{ij}$ in terms of an eddy viscosity $\hat{\nu}_t$, then $\hat{\tau}_{ij}$ can be written as

$$\hat{\tau}_{ij} = \rho\left[\hat{\nu}_t\left(\frac{\partial \hat{u}_i}{\partial \hat{x}_j} + \frac{\partial \hat{u}_j}{\partial \hat{x}_i}\right) - \frac{2}{3}k\delta_{ij}\right], \tag{3.2}$$

where k is the turbulent kinetic energy and δ_{ij} is the Kronecker delta. The pressure p is eliminated from equations (3.1a) and (3.1b) to give

$$\frac{\partial \hat{\omega}}{\partial \hat{t}} + \hat{u}\frac{\partial \hat{\omega}}{\partial \hat{x}} + \hat{w}\frac{\partial \hat{\omega}}{\partial \hat{z}} = \frac{1}{\rho}\left[\frac{\partial^2}{\partial \hat{x}\partial \hat{z}}\left(\hat{\tau}_{xx} - \hat{\tau}_{zz}\right) - \left(\frac{\partial^2}{\partial \hat{x}^2} - \frac{\partial^2}{\partial \hat{z}^2}\right)\hat{\tau}_{zx}\right]. \tag{3.3}$$

If we assume the eddy viscosity $\hat{\nu}_t$ is a constant, (3.3) reduces to

$$\frac{\partial \hat{\omega}}{\partial \hat{t}} + \hat{u}\frac{\partial \hat{\omega}}{\partial \hat{x}} + \hat{w}\frac{\partial \hat{\omega}}{\partial \hat{z}} = \hat{\nu}_t\left(\frac{\partial^2 \hat{\omega}}{\partial \hat{x}^2} + \frac{\partial^2 \hat{\omega}}{\partial \hat{z}^2}\right). \tag{3.4}$$

At the free surface, in the region that does not include the roller, we neglect the small vorticity due to viscous effects. In the roller region, the measurements from hydraulic jumps shown in the later sections of this chapter indicate that the free surface vorticity will also be close to zero. However, strong vorticity is generated inside the roller region. We approximate this vorticity generated by the vorticity at the "dividing" region between the roller and the interior. This situation is illustrated in figure 3.1.

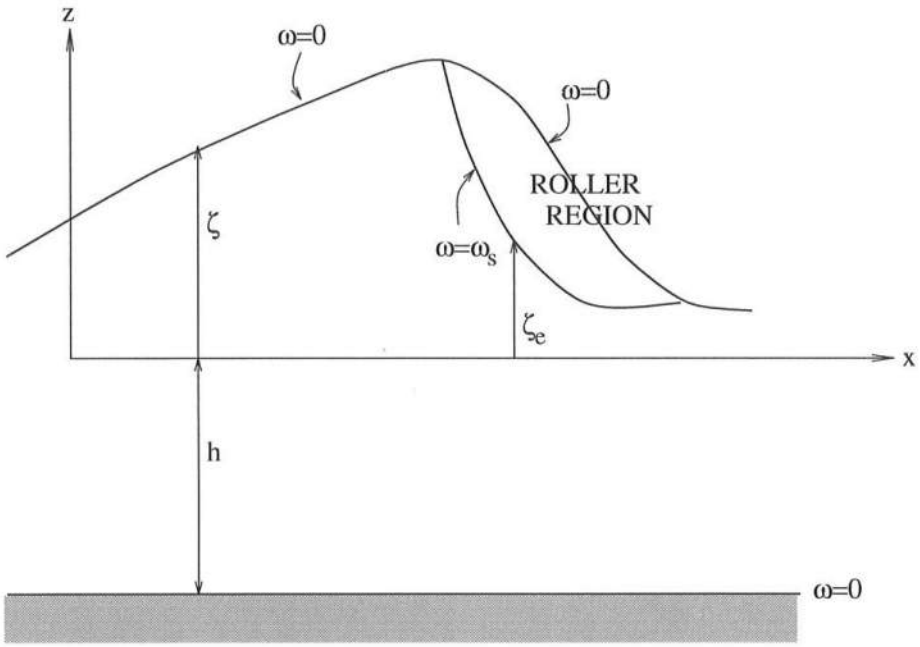

Figure 3.1: Sketch of boundary conditions for the vorticity.

Then, the boundary conditions for vorticity are

$$\hat{\omega}(\hat{z} = \hat{\zeta}_e, \hat{t}) = \hat{\omega}_s(x, t), \tag{3.5a}$$

$$\hat{\omega}(\hat{z} = -\hat{h}, \hat{t}) = 0, \tag{3.5b}$$

and the initial condition is

$$\hat{\omega}(\hat{z}, \hat{t} = 0) = 0, \tag{3.5c}$$

where ζ_e is the lower edge of the roller. Note that in the region where there is no roller, we have $\zeta_e = \zeta$. This also implies, from the discussion above, that $\omega_s = 0$ when $\zeta_e = \zeta$. As mentioned before, the bottom boundary condition of zero vorticity is consistent with the assumption of free-slip at the bottom. The values of ζ_e and ω_s (the vorticity at ζ_e) are discussed later in this chapter. The effect of assuming constant eddy viscosity will be discussed later in conjunction with the model results.

The scales given by (2.1b)-(2.1f) are used to non-dimensionalize (3.4) and we get

$$\frac{\partial \omega}{\partial t} + \delta u \frac{\partial \omega}{\partial x} + \delta w \frac{\partial \omega}{\partial z} = \nu_t \left(\mu^2 \frac{\partial^2 \omega}{\partial x^2} + \frac{\partial^2 \omega}{\partial z^2} \right). \tag{3.6}$$

Finite-difference methods can be used to solve (3.6) numerically. However, the water depths in the surf zone are quite small. To resolve the vorticity distribution over the water column without the use of sophisticated techniques, very fine grid sizes are required. This in turn influences the size of the time steps required for the finite-difference scheme used to solve the Boussinesq equations. Rather than attempt to adapt more efficient numerical methods in this study, we try to obtain analytical solutions to (3.6).

In the surf zone, we generally have $\mu \ll O(1)$ and therefore we omit all terms of $O(\mu^2)$ in the vorticity equation. Furthermore, it will be shown later that the h_x terms in the $O(\mu^2)$ non-linear terms can be omitted with very little effect on the wave shoaling (see also section 1, Chapter 2). The same can be expected for the breaking terms. Therefore, in the following considerations, we limit ourselves to the case where $h_x \sim O(\mu^2)$.

To obtain the analytical solution, we first change the coordinate system from (x, z, t) to (x, σ, t) where

$$x = x, \quad t = t, \quad \sigma = \frac{h + z}{h + \delta \zeta_e}, \tag{3.7}$$

which transforms the domain from $-h \leq z \leq \zeta_e$ to $0 \leq \sigma \leq 1$. Then, in the new coordinate system

$$\frac{\partial \omega}{\partial t} = \frac{\partial \sigma}{\partial t} \frac{\partial \omega}{\partial \sigma} + \frac{\partial \omega}{\partial t} = -\frac{\delta \sigma}{h + \delta \zeta_e} \frac{\partial \zeta_e}{\partial t} \frac{\partial \omega}{\partial \sigma} + \frac{\partial \omega}{\partial t}, \tag{3.8a}$$

$$\frac{\partial \omega}{\partial z} = \frac{\partial \sigma}{\partial z}\frac{\partial \omega}{\partial \sigma} = \frac{1}{h+\delta\zeta_e}\frac{\partial \omega}{\partial \sigma}, \tag{3.8b}$$

$$\frac{\partial^2 \omega}{\partial z^2} = \left(\frac{\partial \sigma}{\partial z}\right)^2 \frac{\partial \omega}{\partial \sigma} = \frac{1}{(h+\delta\zeta_e)^2}\frac{\partial^2 \omega}{\partial \sigma^2}, \tag{3.8c}$$

$$\frac{\partial \omega}{\partial x} = \frac{\partial \sigma}{\partial x}\frac{\partial \omega}{\partial \sigma} + \frac{\partial \omega}{\partial x} = -\frac{\delta\sigma}{h+\delta\zeta_e}\frac{\partial \zeta_e}{\partial x}\frac{\partial \omega}{\partial \sigma} + \frac{\partial \omega}{\partial x} + O(h_x). \tag{3.8d}$$

Equations (3.8a)-(3.8c) are now substituted into (3.6), which gives

$$\frac{\partial \omega}{\partial t} - \delta\left[\frac{\sigma}{h+\delta\zeta_e}\frac{\partial \zeta_e}{\partial t}\right]\frac{\partial \omega}{\partial \sigma} + \delta u\frac{\partial \omega}{\partial x} - \delta^2\frac{u\sigma}{h+\delta\zeta_e}\frac{\partial \zeta_e}{\partial x}\frac{\partial \omega}{\partial \sigma} + \delta\left[\frac{w}{h+\delta\zeta_e}\right]\frac{\partial \omega}{\partial \sigma} = \frac{\nu_t}{(h+\delta\zeta_e)^2}\frac{\partial^2 \omega}{\partial \sigma^2} + O(\mu^2, h_x). \tag{3.9}$$

The boundary conditions (3.5a)-(3.5c) in the new coordinate system are

$$\omega(\sigma = 1, t) = \omega_s(x, t), \tag{3.10a}$$

$$\omega(\sigma = 0, t) = 0, \tag{3.10b}$$

and the initial condition is

$$\omega(\sigma, t = 0) = 0. \tag{3.10c}$$

The governing equation for vorticity (3.9) with the boundary conditions (3.9)-(3.10c) is easier to solve if the boundary conditions can be homogenized. This is accomplished by redefining the dependent variable ω

$$\omega = \Omega + \sigma\omega_s. \tag{3.11}$$

Equation (3.9) then transforms to

$$\frac{\partial \Omega}{\partial t} + \sigma\frac{\partial \omega_s}{\partial t} - \delta\frac{\omega_s\sigma}{h+\delta\zeta_e}\frac{\partial \zeta_e}{\partial t} - \delta\left[\frac{\sigma}{h+\delta\zeta_e}\frac{\partial \zeta_e}{\partial t} - \frac{w}{h+\delta\zeta_e}\right]\left(\frac{\partial \Omega}{\partial \sigma} + \omega_s\right) + \delta u\frac{\partial \Omega}{\partial x} + \delta u\sigma\frac{\partial \omega_s}{\partial x} = \frac{\nu_t}{(h+\delta\zeta_e)^2}\frac{\partial^2 \omega}{\partial \sigma^2} + O(\delta^2, \mu^2, h_x), \tag{3.12}$$

and the new boundary conditions are

$$\Omega(\sigma = 1, t) = 0, \tag{3.13a}$$

$$\Omega(\sigma = 0, t) = 0, \tag{3.13b}$$

and the initial condition is

$$\Omega(\sigma, t = 0) = 0. \tag{3.13c}$$

We now assume Ω to have a solution of the form

$$\Omega = \omega^{(1)} + \delta\omega^{(2)} + \delta^2\omega^{(3)} + \cdots . \tag{3.14}$$

Now, (3.14) is substituted into (3.12) and terms of the same order in δ are collected. This gives the following first and second order boundary value problems in δ:
$O(1)$ problem:

$$\frac{\partial\omega^{(1)}}{\partial t} - \kappa\frac{\partial^2\omega^{(1)}}{\partial\sigma^2} = -\sigma\frac{\partial\omega_s}{\partial t}, \tag{3.15a}$$

where $\kappa = \nu_t/h^2$, with the boundary conditions

$$\omega^{(1)}(\sigma = 1, t) = 0, \tag{3.15b}$$

$$\omega^{(1)}(\sigma = 0, t) = 0, \tag{3.15c}$$

and the initial condition

$$\omega^{(1)}(\sigma, t = 0) = 0. \tag{3.15d}$$

The solution to this system of equations is obtained by first expressing the right hand side of (3.15a) in term of a half-range sine expansion so that

$$-\sigma\frac{\partial\omega_s}{\partial t} = \sum_{n=1}^{\infty} F_n^{(1)} \sin n\pi\sigma, \tag{3.16}$$

which gives

$$\begin{aligned} F_n^{(1)} &= 2\int_0^1 -\sigma\frac{\partial\omega_s}{\partial t}\sin n\pi\sigma \; d\sigma \\ &= (-1)^n\frac{2}{n\pi}\frac{\partial\omega_s}{\partial t}. \end{aligned} \tag{3.17}$$

We now look for solutions to $\omega^{(1)}$ of the form

$$\omega^{(1)} = \sum_{n=1}^{\infty} G_n^{(1)} \sin n\pi\sigma. \tag{3.18}$$

Note that (3.18) satisfies the boundary conditions. Equations (3.18) and (3.16) are substituted into (3.15a), which gives

$$\sum_{n=1}^{\infty} \left[\frac{\partial G_n^{(1)}}{\partial t} + \kappa n^2 \pi^2 G_n^{(1)} - F_n^{(1)} \right] \sin n\pi\sigma = 0, \tag{3.19}$$

which, to be true for all σ, implies that

$$\frac{\partial G_n^{(1)}}{\partial t} + \kappa n^2 \pi^2 G_n^{(1)} - F_n^{(1)} = 0. \tag{3.20}$$

The solution to the ordinary differential equation (3.20), after substituting for $F_n^{(1)}$ from (3.17), is

$$G_n^{(1)}(t) \equiv (-1)^n \frac{2}{n\pi} \int_0^t \frac{\partial \omega_s}{\partial \tau} e^{n^2\pi^2\kappa(\tau - t)} \, d\tau. \tag{3.21}$$

$O(\delta)$ problem:

At this order the governing equation can be written as

$$\frac{\partial \omega^{(2)}}{\partial t} - \kappa \frac{\partial^2 \omega^{(2)}}{\partial \sigma^2} = F^{(2)}, \tag{3.22a}$$

where

$$\begin{aligned} F^{(2)} =& 2\kappa \frac{\zeta_e}{h} \frac{\partial^2 \omega^{(1)}}{\partial \sigma^2} + 2\omega_s \frac{\sigma}{h} \frac{\partial \zeta_e}{\partial t} + \frac{\sigma}{h} \frac{\partial \zeta_e}{\partial t} \frac{\partial \omega^{(1)}}{\partial \sigma} - u^{(1)} \frac{\partial \omega^{(1)}}{\partial \sigma} - u^{(1)} \sigma \frac{\partial \omega_s}{\partial x} \\ & - \frac{w^{(1)}}{h} \left(\frac{\partial \omega^{(1)}}{\partial \sigma} + \omega_s \right), \end{aligned} \tag{3.22b}$$

with the superscripts on u and w referring to the solutions obtained from the first order equation. The boundary conditions are

$$\omega^{(2)}(\sigma = 1, t) = 0, \tag{3.22c}$$

$$\omega^{(2)}(\sigma = 0, t) = 0, \tag{3.22d}$$

and the initial condition is

$$\omega^{(2)}(\sigma, t = 0) = 0. \tag{3.22e}$$

The solution to (3.22) is obtained as in the $O(1)$ case,

$$\omega^{(2)} = \sum_{n=1}^{\infty} G_n^{(2)} \sin n\pi\sigma, \tag{3.23}$$

where

$$G_n^{(2)} = \int_0^t F_n^{(2)} e^{n^2\pi^2\kappa(\tau - t)}\, d\tau, \tag{3.24}$$

$$F_n^{(2)} = 2\int_0^1 F^{(2)} \sin n\pi\sigma\, d\sigma. \tag{3.25}$$

In the expression for $F_n^{(2)}$, $F^{(2)}$ is evaluated from the solution to the $O(1)$ equation. Thus, the total expression for vorticity is

$$\omega = \sigma\omega_s + \sum_{n=1}^{\infty} \left[G_n^{(1)} + G_n^{(2)}\right] \sin n\pi\sigma, \tag{3.26}$$

from which the expressions for the breaking terms are calculated (Appendix B). Now, to obtain a solution for the breaking waves, the magnitude ω_s of the vorticity generated by the breaking process, the boundary where it is applicable and the magnitude of the eddy viscosity is needed. This is obtained from the analysis of measurements in hydraulic jumps detailed below.

3.2 Analysis of hydraulic jump data

The measurements used in this study were reported by Bakunin (1995). The experimental set-up is shown schematically in figure 3.2 which also shows the definition of the basic geometrical parameters for the jumps. In the following the depth h_1 refers to the minimum depth in front of the jump where depth averaged velocity is U_1. The depth h_2 refers to the depth sufficiently far downstream of the jump where the conditions are largely uniform and h_0 is the water depth at the first measurement location. The coordinate system is defined such that $z = 0$ at the bottom and $x = 0$ at the toe of the roller.

The jumps were generated downstream of an undershot weir in a closed circuit hydraulic flume by adjusting the discharge, the downstream overflow weir, and the height of the undershot weir. The bottom was made of smooth steel and the walls of glass.

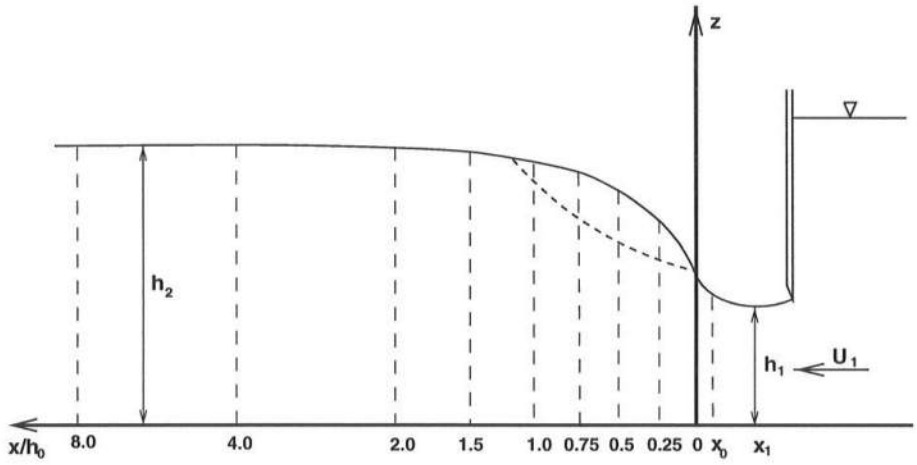

Figure 3.2: Sketch of experimental setup for the hydraulic jump measurements and definition of parameters.

Measurements were taken with a 2D Laser Doppler Velocimeter (LDV) placed outside the glass walls and operated in back scattering mode. The signal was processed using burst spectrum analyzers, leading to an average data rate of 1000 Hz, which was subsequently bin-averaged to a 200 Hz rate.

The surface elevation was measured simultaneously by means of a capacitance wave gage, sampled at 100 Hz. The outer diameter of the wire was $1mm$, which is believed to be small enough to make the surface disturbances generated around the wire, by the wire itself, negligible in comparison to the elevations in the jump. The vertical lines in figure 3.2 indicate verticals along which a large number of measurements were taken. In the following analysis the origin of the horizontal x-axis was placed at the toe of the turbulent front and the distances of the measuring sections from the toe are as indicated in the figure. The position of the toe was determined by measuring the average distance to the measuring station at x_0. Further details of the experimental setup may be found in Bakunin (1995).

Detailed measurements were performed for three different jumps. The measured identification parameters for the jumps (the depth h_0 at the only measuring section in the front of the jump, and the mean velocity U_0 at h_0) are given in Table 3.1. For the third hydraulic jump, no measurements were taken at $x/h_0 = 0.25$.

Table 3.1: Measured identification parameters for the jumps.

Jump No.	h_0 (m)	U_0 (m/s)
1	0.072	0.95
2	0.064	1.06
3	0.059	1.16

As will be seen shortly, the jumps correspond to relatively small values of the Froude number ($\mathcal{F} = 1.38, 1.46, 1.56$). These small values were chosen because they correspond to ratios between maximum and minimum depths in the jumps that are similar to the depth ratios for surf zone waves. Hence, such jumps provide the best similarity with nearshore breaking waves which was an important part of the motivation for the experiments. For completeness we notice that these values were large enough to make all the jumps turbulent. Only the smallest of the jumps showed a weak tendency of undular behavior downstream of the turbulent front.

The scale of the experiments was also chosen small enough to minimize the entrainment of air bubbles at the turbulent front, which highly facilitated the LDV measurements and made it possible to measure well into the surface roller. As indicated by Banner and Phillips (1974) and later by Peregrine and Svendsen (1978) the generation of turbulence at the front of a hydraulic jump or breaking wave can exist without air entrainment. On the other hand the jumps were large enough and the turbulence strong enough to render capillary forces negligible.

3.2.1 Volume Flux and Froude Number

The first goal is to ensure that the interpretation of measured velocities satisfy the conservation laws for mass and momentum throughout the jump. In order to

achieve this an analytical curve-fit is developed for the measured horizontal velocities along each of the verticals in the dataset. The verticals were divided into four regions and the following approximations used:

1. In the wall region, from the bottom ($z = 0$) to the first measurement location in the vertical, $z = z_1$ ($\sim$1 mm above the bottom), we used

$$u(z) = u_1(\frac{z}{z_1})^{1/7}. \tag{3.27}$$

2. In the boundary layer $z_1 \leq z \leq \delta$, where δ is displacement thickness determined from the data,

$$u = u_1 + C\ \log(\frac{z}{z_1}), \tag{3.28}$$

where C is found by least square fit to the measured values in the boundary layer.

3. In the middle region, $\delta < z < z_2$, the velocities are nearly constant. This region constitutes the largest part of the depth. A fourth-order polynomial was used in a least squares fit subject to continuity constraints in velocity and velocity gradients at the boundaries to region (2) and (4).

4. In the upper region, $z_2 < z < h$, which includes the roller region a third-order polynomial was used. This is the region with the largest velocity variation. As mentioned, the constraints in the least square fit were continuity in velocity and velocity gradient at the connection to region (3) and zero gradient at the mean free surface corresponding to zero (or small) shear stress there.

The original measurement values and the corresponding curve-fitted velocity profiles are shown in figure 3.3. At each vertical section, the figure also shows the measured position of the mean free surface (marked with a +) and the lower limit of the roller (marked with a $\circ$), which is to be determined later.

It is seen that the curve-fitted profiles represent the measurements with high accuracy. In the following, this is further verified by using the measured velocities to determine the mean volume flux ($\overline{Q}$) in the jump

$$\overline{Q} = \int_{-B/2}^{B/2} \int_0^h u\ dz\ dy, \tag{3.29}$$

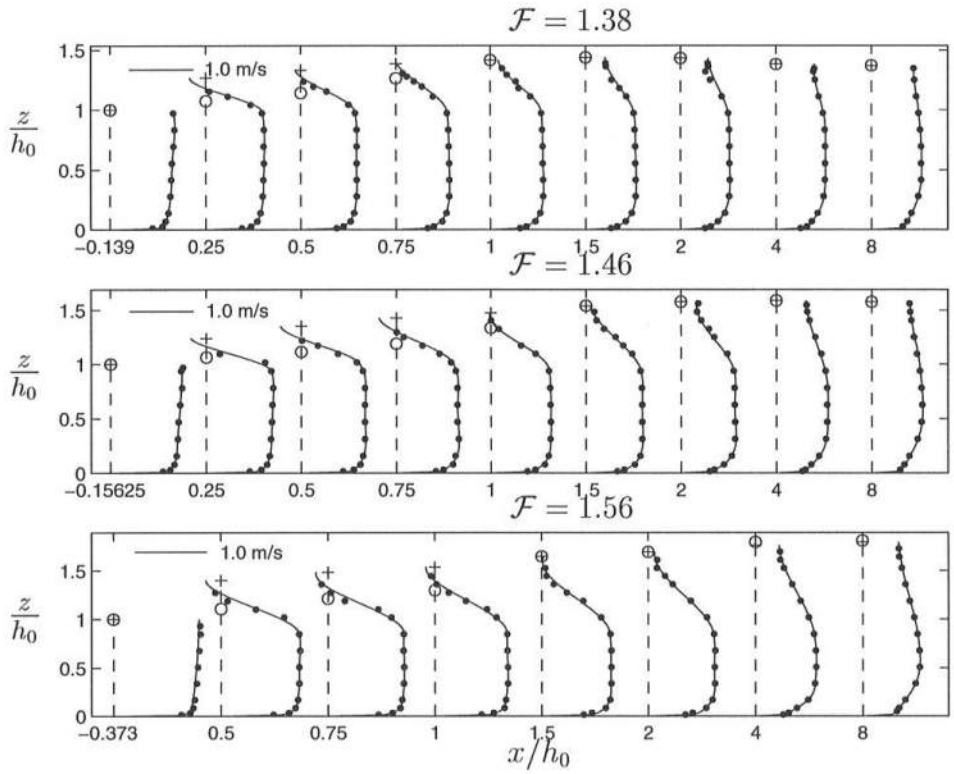

Figure 3.3: Measured horizontal velocities (•) and curve fits to the velocity (———), the mean water surface (+) and the calculated location of the dividing streamline (○) for all three jumps.

where B is the total width of the channel. No measurements of the lateral velocity variations were taken during the experiments, but it was found that the boundary layers along the glass side walls gave non-negligible reductions in the total volume flux. This effect was compensated for by assuming that the side wall boundary layers are similar to the boundary layer along the smoothly painted steel bottom. Hence, the integral over the cross-section in (3.29) was evaluated as

$$\overline{Q} = (B - 2\delta) \int_0^h u \, dz, \tag{3.30}$$

where δ was determined from the vertical profiles. Figure 3.4 shows the variation of the total discharge in the three jumps found by (3.30). We see that for each jump

the value for the discharge stays within 0.05% of a mean value. Knowing that Q is a constant we therefore define the mean volume flux as

$$\overline{Q} = \frac{1}{L} \int_L Q \, dx, \tag{3.31}$$

where L is the length of the jump. In the following, this mean value is used as the discharge for each jump. These values are

Jump No. 1: $\overline{Q} = 20.80 \; l/s$

Jump No. 2: $\overline{Q} = 20.54 \; l/s$

Jump No. 3: $\overline{Q} = 20.32 \; l/s$

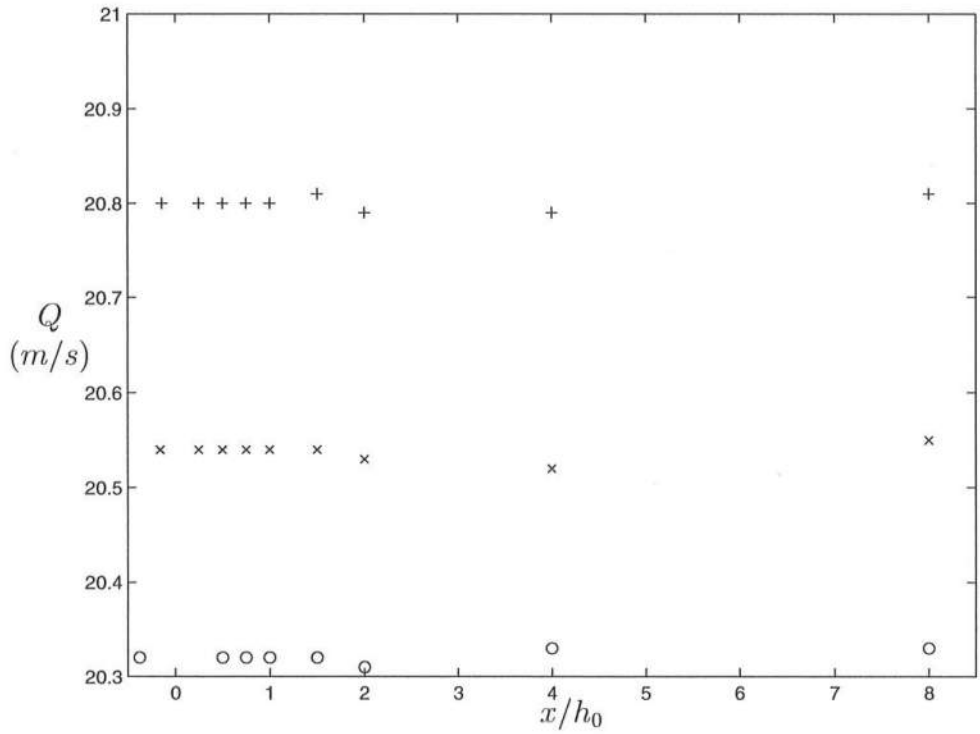

Figure 3.4: Variation for computed volume fluxes $Q(x)$. $+$ is for $\mathcal{F} = 1.38$, $\times$ is for $\mathcal{F} = 1.46$ and $\circ$ is for $\mathcal{F} = 1.56$.

With $\overline{Q}$ known, it is possible to calculate the Froude number

$$\mathcal{F} = \frac{\overline{Q}}{(B - 2\delta)h\sqrt{gh}} \tag{3.32}$$

for the jump, which however requires specification of h. In the experiments, the jumps were generated behind an undershot weir. The contraction of the cross section at the weir created a weak depression in the water surface which resulted in a minimum water depth at some distance downstream of the weir (see figure 3.2). From this minimum position, the water surface again curved slightly upward so that the surface had a non-zero slope at the mean position of the actual toe of the jump. The first cross-section where measurements were taken ($x = x_0$ in figure 3.2) was at distances of 10 mm, 10 mm and 22 mm, respectively, upstream of the mean position of the toe for jumps 1, 2 and 3, respectively. The water depth at that position was h_0 (table 3.1). The slope of the mean water surface at this first measurement section can be estimated from the values of the vertical mean velocities w at the point. They are shown in figure 3.5. We see that even at the surface the vertical velocity w at section x_0 is small in comparison to the horizontal velocity shown in figure 3.3.

Since the actual measurement position in front of the jump is somewhat arbitrary, we choose to use the minimum depth (h_1) as the reference depth for each jump. This makes it possible to determine the deviation from hydrostatic pressure in the front of the jump and the effect this has on the momentum balance. The depth h_1 was not measured directly. Therefore, it was estimated by assuming that the mean water surface between the weir and the toe can be approximated by a second order Taylor expansion of the surface elevation around the minimum at x_1. The slope of the free surface at $x = x_1$ is zero. Therefore, this expansion can be written as

$$h(x) = h(x_1) + \frac{(x - x_1)^2}{2R_s}, \tag{3.33}$$

where R_s is the radius of curvature of the surface at x_1. The non-static pressure gives rise to a relatively small correction ($1.7\% - 6.3\%$ in the momentum balance, see table 3.4). Thus, it is expected that this is a sufficiently accurate approximation. The values of R_s and x_1 will be determined from the measurements at x_0 as follows.

The surface slope dh/dx at the first measuring section (x_0) is determined by the value

$$\frac{dh}{dx} = \tan\theta = w_s/u_s \qquad \text{at} \quad z = h_0 \tag{3.34}$$

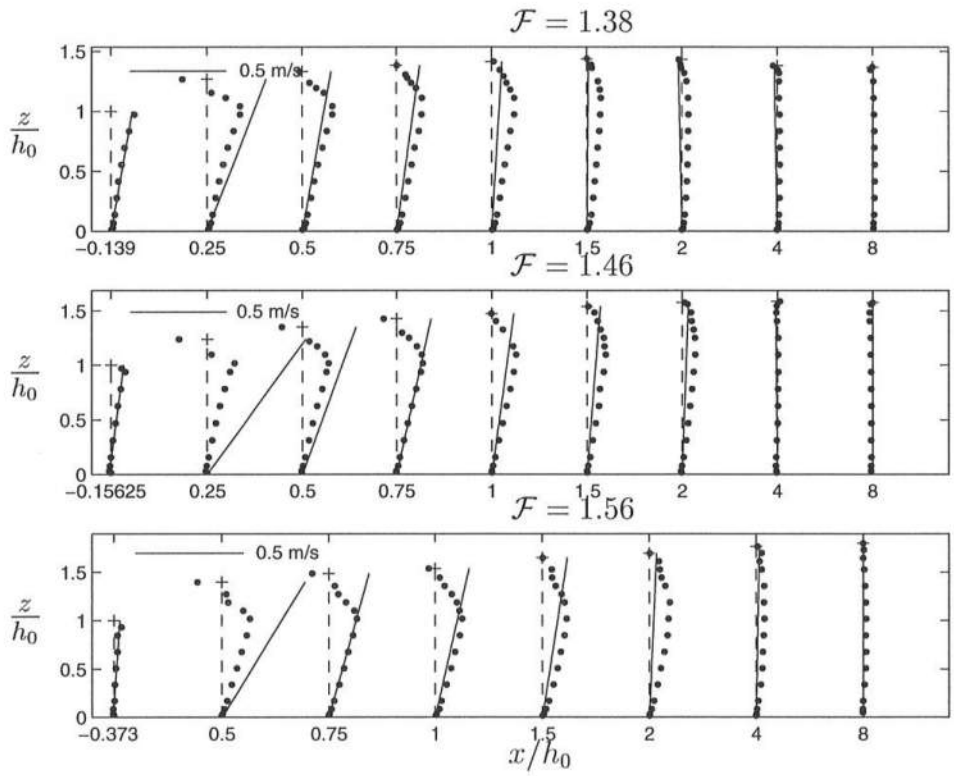

Figure 3.5: Measured values of the vertical velocities w (•). The solid lines indicate $w = uzh_x/h$ (Equation 3.47).

using a best fit for the measured values for w. Here w_s and u_s denote the surface values of u and w. Then R_s between the weir and the toe of the jump is given by

$$R_s = \frac{x_0 - x_1}{w_s/u_s}, \tag{3.35}$$

and we get

$$h_1 = h_0 - \frac{1}{2}(x_0 - x_1)\frac{w_s}{u_s}. \tag{3.36}$$

The values of h_0, R_s and h_1 are shown in Table 3.2.

The values of $\mathcal{F}(\overline{Q})$ calculated on the basis of $\overline{Q}$ and h_1 are shown in Table 3.3 (column 1) along with the Froude number $\mathcal{F}_0(\overline{Q})$ obtained by using the measured depth h_0 at x_0 directly (column 2). We see that the two values of $\mathcal{F}$ differ substantially, which indicates the importance of the difference between h_0 and h_1.

Table 3.2: Values of the depth at the measuring location in front of the jump (h_0), the radius of curvature of the surface (R_s) and the estimated minimum depth in front of the jump (h_1).

Jump No.	h_0 (m)	R_s (m)	h_1 (m)
1	0.072	1.087	0.063
2	0.064	2.437	0.060
3	0.059	5.894	0.057

Table 3.3: Measured and calculated Froude numbers for the jumps using equation (3.32) with $h = h_1$ (column 1), with $h = h_0$ (column 2), equation (3.37) with $h = h_1$ (column 3) and equation (3.43).

Jump No.	$\mathcal{F}(\overline{Q})$	$\mathcal{F}_0(\overline{Q})$	$\mathcal{F}'$	$\mathcal{F}(3.43)$
1	1.378	1.128	1.416	1.371
2	1.464	1.326	1.500	1.472
3	1.562	1.484	1.652	1.621

3.2.2 Momentum Balance in the Jump

Determination of the correct Froude number is also of interest in connection with the overall momentum balance in the jump. The momentum balance gives the connection between the Froude number and the conjugate depth (h_1) and the depth far downstream of the jump (h_2). In classical hydraulics, the assumptions of depth uniform velocities and hydrostatic pressure at both h_1 and h_2 lead to the well known expression

$$\mathcal{F}'^2 = \frac{1}{2}\xi(\xi + 1), \tag{3.37}$$

where $\xi \equiv h_2/h_1$. The results for $\mathcal{F}'$ determined from the calculated value of h_1 and the measured value of h_2 (at $x/h_0 = 8$) are also given in Table 3.3. These values again differ substantially from the value of $\mathcal{F}$ determined by (3.32). The reason is

that the two basic assumptions behind (3.37) are not satisfied. The velocity u is not uniform over depth and the pressure is not hydrostatic, in particular not at x_1.

To determine the correct expression for the momentum balance, we introduce the Reynolds decomposition

$$u = \widetilde{u} + u', \quad \widetilde{u} = \frac{1}{T}\int_0^T u\, dt, \tag{3.38}$$

$$w = \widetilde{w} + w', \quad \widetilde{w} = \frac{1}{T}\int_0^T w\, dt, \tag{3.39}$$

where T is the length of the time series. The momentum equation for constant density in the general form for a control volume covering vertical sections at h_1 and h_2 then becomes

$$\int_{A_1} \left[\rho\left(\widetilde{u}^2 + \widetilde{u'^2}\right) + p\right]\, dA - \int_{A_2} \left[\rho\left(\widetilde{u}^2 + \widetilde{u'^2}\right) + p\right]\, dA - \int_{x_1}^{x_2} (B + 2h)\tau_b\, dx = 0, \tag{3.40}$$

where $\widetilde{u}$ represents the ensemble averaged velocity, u' is the turbulent fluctuations and τ_b is the bottom friction. In the following, we will omit the $\overline{()}$ over the ensemble averaged velocity except where ambiguous. There are no measurements available to estimate the side wall friction directly. However, the estimates of the volume flux, based on the assumption that the side wall friction is equal to the bottom friction, show that this assumption is reasonable.

Introducing a momentum correction factor (α) and a pressure correction factor (κ) defined by

$$\alpha \equiv \frac{A}{Q^2}\int_A \left(u^2 + \widetilde{u'^2}\right)\, dA \tag{3.41a}$$

and

$$\kappa \equiv \frac{2}{\rho g h^2 B}\int_A p\, dz \tag{3.41b}$$

respectively, where $A = hB$, (3.40) can be written

$$\alpha_1 \frac{\overline{Q}^2}{g h_1^3 B^2} + \frac{1}{2}\kappa_1 = \alpha_2 \frac{\overline{Q}^2}{g h_1^3 B^2}\,\frac{1}{\xi} + \frac{1}{2}\kappa_2 \xi^2 + \tau', \tag{3.42}$$

where

$$\tau' \equiv \frac{1}{gh_1^2} \int_{x_1}^{x_2} (B + 2h)\tau_b \, dx.$$

Solving with respect to $\mathcal{F}^2 = \overline{Q}^2/(gh_1^3B^2)$ then gives

$$\mathcal{F}^2 = \frac{1}{2}\xi \frac{\kappa_2\xi^2 - \kappa_1 + \tau'}{\alpha_1\xi - \alpha_2}. \tag{3.43}$$

Svendsen *et al.* (1998) showed that τ', the contribution from the bottom friction, is negligible for the present measurements. Evaluation of $\mathcal{F}$ from (3.43) requires determination of the α and κ coefficients. The α's are determined directly from the definition (3.41a) by assuming the integration across the channel can be approximated by

$$\int_A \left(u^2 + \widetilde{u'^2}\right) \, dA \sim (B - 2\delta') \int_0^h u^2 \, dz, \tag{3.44}$$

where δ' is the momentum thickness determined for the vertical profiles and defined by

$$\delta' = \int_0^h \frac{u}{U}\left(1 - \frac{u}{U}\right) \, dz, \tag{3.45}$$

where the contribution from u' is neglected. The curve-fitted velocities are used for the evaluation of (3.44) and the values are shown in table 3.4.

The pressure coefficient κ_1 is determined by realizing that

$$p(z) = \rho g(h - z) - \rho\left(w^2 + \widetilde{w'^2}\right) + \frac{\partial}{\partial x}\left[\int_z^h \rho\left(uw + \widetilde{u'w'}\right) dz\right]. \tag{3.46}$$

It turns out that in (3.46) the contributions from the turbulent fluctuations are negligible.

The assumption of the linear variation of w/u in the region in front of the jump gives

$$\frac{w}{u} = \frac{z}{h}\frac{dh}{dx}, \qquad \frac{dh}{dx} = \frac{x - x_1}{R_s}, \tag{3.47}$$

where R_s is given by (3.34). Introducing the dynamic pressure p_D defined by

$$p_D \equiv p - \rho g(h - z) \tag{3.48}$$

and substituting (3.46) and (3.47) in (3.48), we can write p_D as

$$\begin{aligned} p_D(z) &= -\rho U^2 \frac{z^2}{h^2}\left(\frac{dh}{dx}\right)^2 + \frac{d}{dx}\left(\frac{1}{2h}\rho U^2(h^2-z^2)\frac{dh}{dx}\right) \\ &= -\rho U^2 \frac{z^2}{h^2}\left(\frac{dh}{dx}\right)^2 + \frac{1}{2}\rho\frac{\overline{Q}^2}{B^2}\frac{d}{dx}\left(\frac{h^2-z^2}{h^3}\frac{dh}{dx}\right). \end{aligned} \tag{3.49}$$

We then get, after some algebra

$$\int_0^h p_D(z)dz = \frac{1}{3}\rho\frac{\overline{Q}^2}{B^2}h\frac{d}{dx}\left(\frac{1}{h}\frac{dh}{dx}\right) \tag{3.50}$$

and hence from (3.41b)

$$\kappa = 1 + \frac{2}{3}\frac{\overline{Q}^2}{ghB^2}\frac{d}{dx}\left(\frac{1}{h}\frac{dh}{dx}\right). \tag{3.51}$$

At h_1 we have $dh/dx = 0$ and, as (3.47) shows, $d^2h/dx^2 = R_s^{-1}$ so that κ_1 becomes

$$\kappa_1 = 1 + \frac{2}{3}\mathcal{F}^2\frac{h_1}{R_s}. \tag{3.52}$$

It is emphasized that this result assumes (3.47) applies, which we see from figure 3.5 is not the case in the central part of the jump. This will be discussed in further detail later in connection with the analysis of the momentum variation between sections 1 and 2.

The values of κ_1 calculated from (3.52) are also shown in Table 3.4.

For the section at h_2 ($x/h_0 = 8$), we have no information from which κ_2 can be determined. However, since this is far downstream of the jump where dh/dx is close to zero, we assume $\kappa_2 \sim 1.0$.

The values of the correction factors along with the measured values of ξ (also listed in Table 3.1) are then used to determine $\mathcal{F}_1^2$ from (3.43) and these values are also given in Table 3.4. We see that these results for $\mathcal{F}_1$ are in much closer agreement with $\mathcal{F}_1$ values determined directly from the measurements using (3.32). The results for jumps 1 and 2 are, in fact, remarkably similar. The agreement between $\mathcal{F}$ by (3.43) and $\mathcal{F}$ by (3.32) gives basis for expecting that (3.43) includes the major mechanisms active in the jump. On the other hand, the significant difference

Table 3.4: Values of $\xi, \alpha_1, \alpha_2, \kappa_1$ and κ_2.

Jump No.	$\xi = \frac{h_2}{h_1}$	α_1	α_2	κ_1	κ_2
1	1.565	1.0129	1.0194	1.063	1.00
2	1.680	1.0127	1.0260	1.037	1.00
3	1.889	1.0124	1.0360	1.017	1.00

between these values and $\mathcal{F}'$ determined from the classical expression (3.37) indicates that effects of non-uniform velocities and non-hydrostatic pressure are important.

In all, these results underscore the importance of the seemingly small deviations in the experiments from the ideal conditions usually assumed in classical hydraulics.

3.2.3 Momentum variation inside the jump

In general, we should expect the momentum flux M to be constant through all vertical sections of the jump. When integrating over depth to determine the momentum flux, notice that the turbulent fluctuations of the free surface are included so that the instantaneous depth $h(x,t) = \tilde{h}(x) + h'(x,t)$. A related problem has been discussed recently by Brocchini and Peregrine (1996) when defining mean shorelines of waves on beaches. Hence the velocity part of the momentum flux becomes

$$\int_0^{\tilde{h}+h'} \widetilde{(\tilde{u}+u')^2}\, dz = \int_0^{\tilde{h}} (\tilde{u}^2 + \widetilde{u'^2})\, dz + \int_{\tilde{h}}^{h'} \widetilde{(\tilde{u}+u')^2}\, dz. \tag{3.53}$$

Here the last term can be approximated by $2\tilde{u}\widetilde{u'h'} + \widetilde{h'u'^2}$ where the value of the variables are taken near the surface. Not enough information is available to precisely assess the value of these terms. However, we know that $h' \ll \tilde{h}$ even near the toe of the roller. Furthermore u' which gives the main contribution to the turbulent part of the first integral in (3.53) is smaller at the surface than near the lower edge of the roller. Hence it is expected that these terms will be smaller than $\int_0^{\tilde{h}} \widetilde{u'^2}\, dz$, which in turn gives negligible contributions to the overall momentum flux, as we will see

shortly. Hence in the following we omit the terms due to the turbulent fluctuations of the free surface.

Omitting the $\tilde{()}$ over the ensemble averaged quantities except when ambiguous we can write the total momentum flux as

$$M(x) = \int_0^{h(x)} \rho \left(u^2 + \widetilde{u'^2} \right) \, dz + \int_0^{h(x)} p \, dz, \tag{3.54}$$

where $\rho\widetilde{u'^2}$ is the turbulent normal stress. We use the term M_1 for the momentum flux through the section at h_1 and $M(x)$ should then satisfy

$$M(x) = M_1 - \int_{x_1}^{x} \left(1 + \frac{2h}{B} \right) \tau_w \, dx. \tag{3.55}$$

Here the wall friction τ_w has been determined by a simple friction factor formula

$$\tau_w = \frac{1}{8} \rho f U^2, \tag{3.56}$$

where f is the friction coefficient. Since the roughness of both the bottom and the sides of the flume is very small, f is set to 0.01 (see, e.g., Henderson, 1966).

Estimates of the contribution from the wall shear stresses show that the term involving τ_w in (3.55) is $O(10^{-3} \cdot \rho U^2 h_1)$ for all three Froude numbers. Hence, the wall friction is negligible in comparison to the other contributions to M.

For the calculation of M, the pressure $p(z)$ is determined from (3.46). In that expression, w, w', uw and $\widetilde{u'w'}$ were measured directly. The contribution to p from $\widetilde{u'w'}$ is small but that is not the case for uw near the front of the jump. The total contribution from p can be written

$$\int_0^{h(x)} p \, dz = \frac{1}{2} \rho g h(x)^2 - \int_0^{h} \rho \left(w^2 + \widetilde{w'^2} \right) \, dz + \int_0^{h} \frac{\partial}{\partial x} \left(\int_z^{h} (\rho uw + \widetilde{u'w'}) \, dz \right) \, dz. \tag{3.57}$$

Here the inner integral in the last term can be evaluated directly from measured quantities, but only along the verticals where measurements were taken. In order to obtain the x-derivatives in that term, spline approximations were developed for the values of the integral of $uw + \widetilde{u'w'}$ in (3.57).

Figure 3.6 shows the contribution from the main terms in (3.54), with (3.57) substituted, for the x positions where measurements were taken. We see that by far the most important terms are the u^2 and the p-contributions, whereas the effect of the turbulent normal stresses is only about 1%. The $\widetilde{u'w'}$ contributions to the pressure variation turn out to be small. On the other hand the w^2 and the uw contributions to $p(z)$ are of some importance, in particular in the roller region.

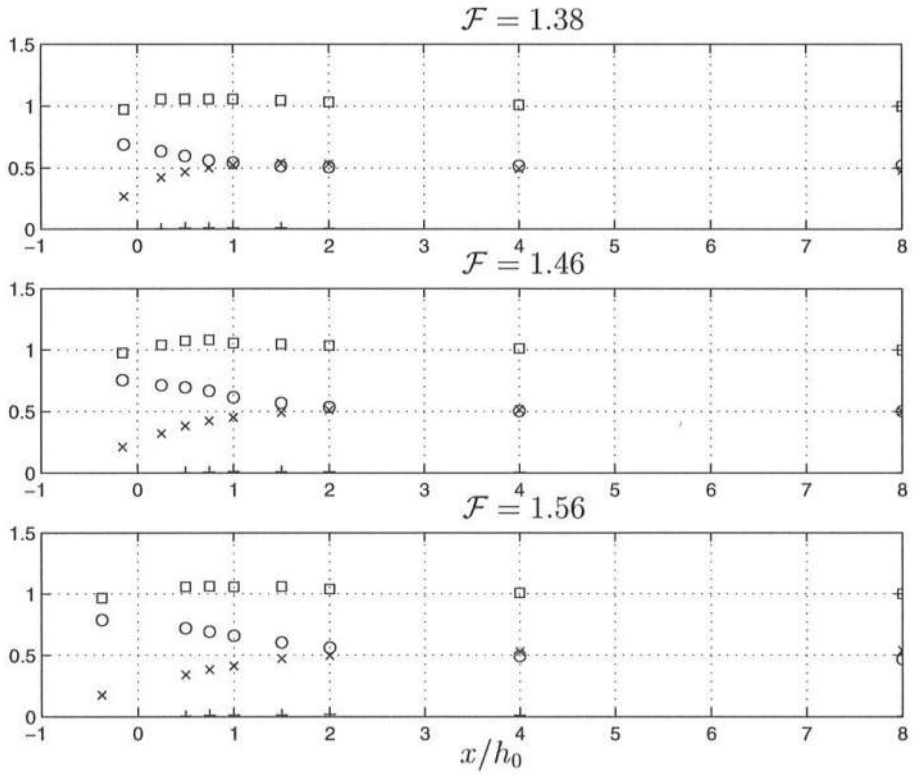

Figure 3.6: Calculated momentum flux $M(x)/M_2$ along the jump where M_2 is the momentum flux at $x/h_0 = 8$. $\square$ is the total momentum, $\times$ is the pressure contribution, $\circ$ is the velocity contribution and $+$ is the turbulent normal stresses.

The values of $M(x)$ itself are also shown and we see that M is constant to within 5%, with the largest errors occurring in the roller region.

A possible reason for the inaccuracies in M is associated with the fact that the measurements of $h(x)$ plays an important role in the results for M, and there

is no information as to how the capacitance wave gages function for a surface with large turbulent fluctuations as in the front of the jump.

So for all practical purposes, the momentum flux M may be approximated by

$$M = \rho\alpha(x)\frac{Q^2}{h(x)} + \frac{1}{2}\rho g\kappa(x)h(x)^2, \tag{3.58}$$

where $\alpha(x)$ and $\kappa(x)$ represent the local values of the momentum and pressure correction factors defined by (3.41a) and (3.41b), respectively. The values of $\alpha(x)$ and $\kappa(x)$ found by the procedure described above are shown in figure 3.7. It is emphasized that while the $\alpha(x)$-values in this are fairly accurate, various checks show that the values of $\kappa(x)$ are somewhat less accurate.

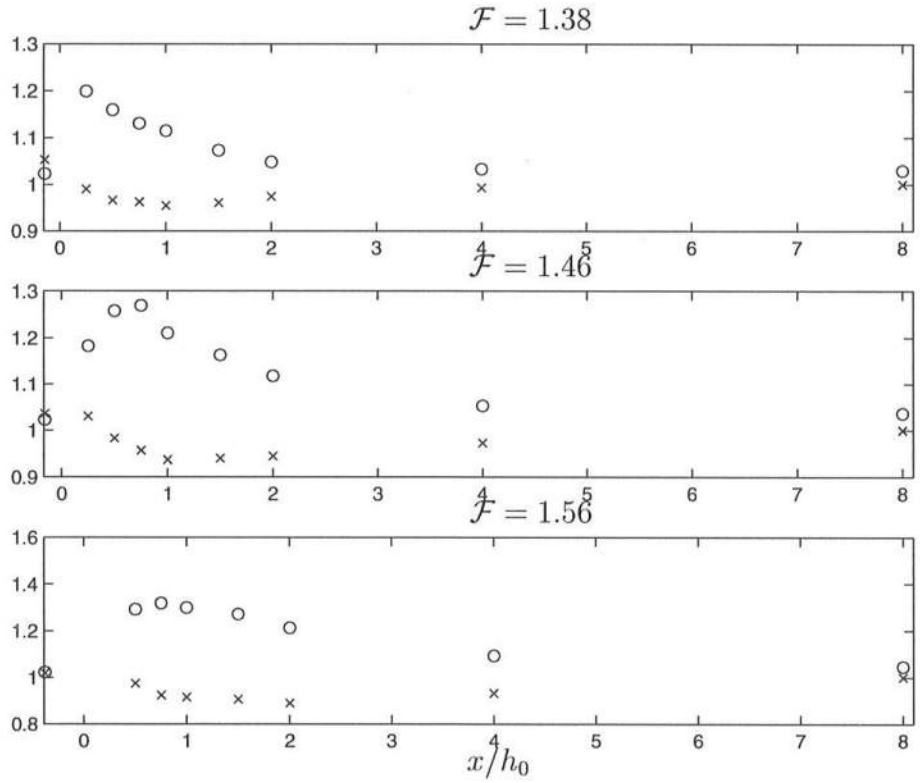

Figure 3.7: α ($\circ$) and κ ($\times$) values for the three hydraulic jumps.

It is essential for the connection to breaking waves to realize that $(\alpha - 1)$ and $(\kappa - 1)$ represent the difference between the actual flow and the flow according to a non-linear shallow water (NSW) model. This difference is obviously generated by the turbulent front with the roller, in addition to the vertical accelerations represented by the curvature of the streamlines. In the NSW model, the momentum flux anywhere between the vertical sections 1 and 2 is smaller than the actual momentum flux. This momentum deficit ΔM defined by

$$\Delta M \equiv M - M_{NSW} \tag{3.59}$$

is therefore determined as

$$\Delta M = \rho \left((\alpha - 1) \frac{Q^2}{h(x)} + \frac{1}{2} g (\kappa - 1) h(x)^2 \right). \tag{3.60}$$

The ΔM is generated by the breaking front and is just large enough to make M constant through the jump and hence prevent the front from steepening further. If we imagined a situation where the combined effects of α and κ were insufficient to create the necessary enhancement of the momentum, the NSW-model would obviously cause the front to steepen further. This would increase the breaking intensity and hence ΔM (see also Svendsen and Madsen 1984). The principle of artificially adding ΔM has been used by Schäffer *et al.* (1992) to establish a Boussinesq model for breaking waves. It can also be shown that the effect of adding an artificial eddy viscosity term to the Boussinesq equations is the same as that of adding the ΔM term (Svendsen *et al.* 1996).

The variation of ΔM determined from the measurements is shown in figure 3.8 along with the surface elevation ζ. The horizontal coordinate is x/h_0 and we see that while the maximum of ΔM is close to the toe and inside the roller region, the magnitude of ΔM remains large much further downstream of the end of the actual roller. It has been shown (see, e.g., Svendsen *et al.* 1996) that this shape of ΔM, with a maximum inside the roller region, is essential for a wave model to simulate breaking.

3.2.4 Variation of the roller thickness.

The accurate curve-fits for the horizontal velocity profiles combined with the information about the volume flux in the jump make it possible to determine the

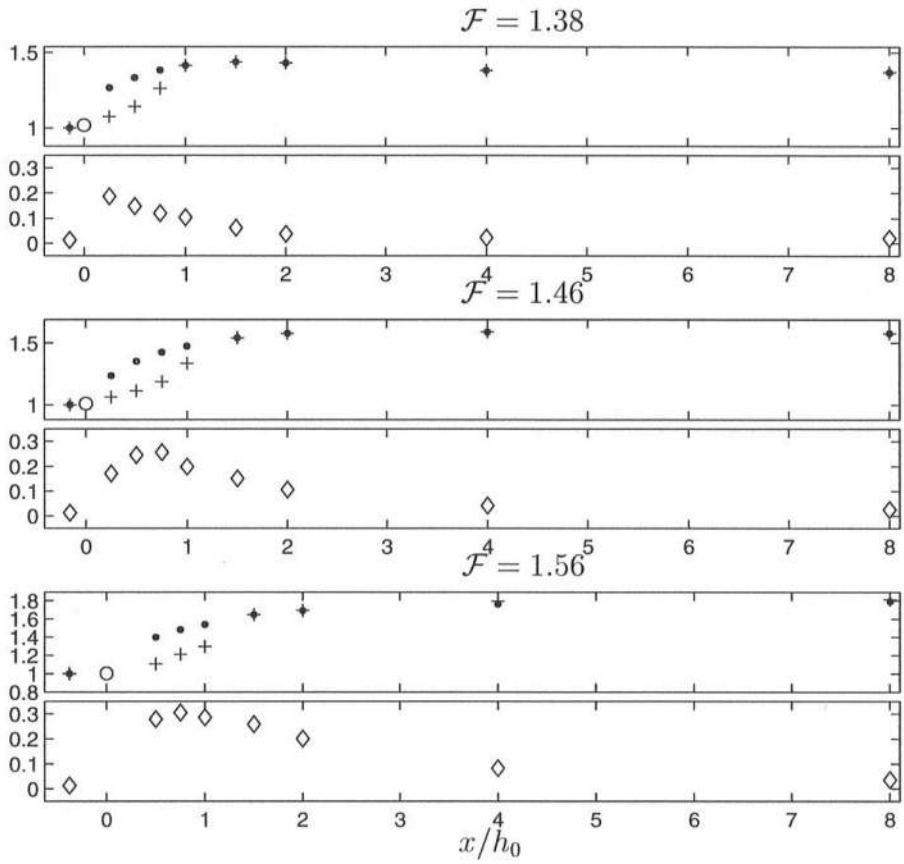

Figure 3.8: The variation of the surface elevation η ($\bullet$) and ΔM ($\diamond$) along with the location of the dividing streamline ($+$) and the calculated water depth at the toe of the jump ($\circ$).

lower limit of the roller, because the net volume flux over the roller is zero. Hence, the height h_r of the roller above the bottom satisfies the equation

$$\overline{Q} = \int_0^{h_r} u \, dz. \tag{3.61}$$

The thickness of the roller is accordingly given by

$$e = h - h_r. \tag{3.62}$$

The values of $e(x)$ found this way have been used to indicate the lower boundary of the roller $\circ$'s in figure 3.3.

An approximate value for the length ℓ_r of the roller can be obtained by interpolation between the verticals. Figure 3.9 shows that there is a reasonable similarity for the variation of $e(x)/h_2\sqrt{\xi}$ versus x/ℓ_r for all three jumps. It is interesting to notice that the roller ends well before the depth reaches its maximum downstream value.

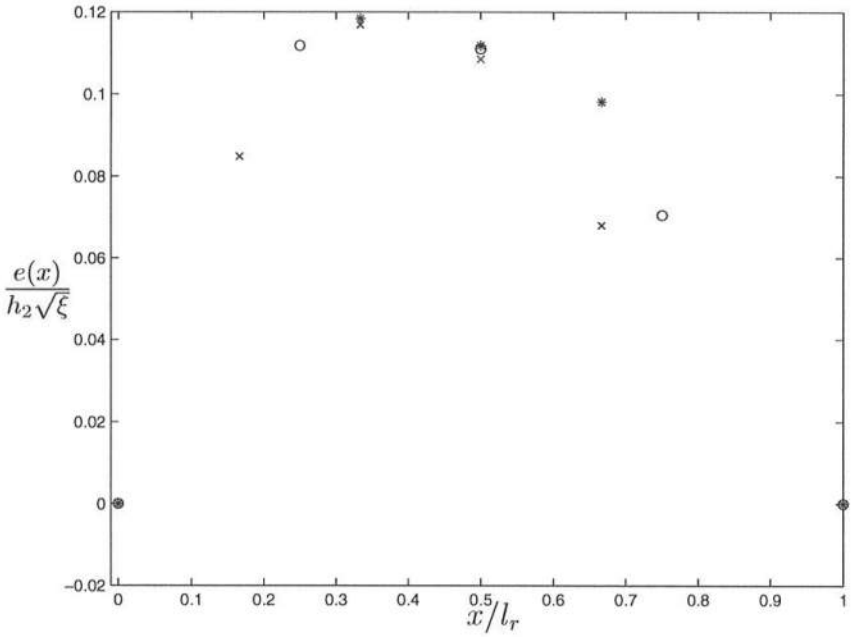

Figure 3.9: Non-dimensional roller thickness $e(x)/h_2\sqrt{\xi}$ versus x/ℓ_r. $\circ$ jump no 1, $\times$ jump no 2, $\star$ jump no 3.

Another important aspect of the flow is the generated turbulent stresses. The measured data provide information for $\widetilde{u_i'u_j'}$ for all the same points for which mean velocities were obtained. Figure 3.10 shows the measured values of $\widetilde{u'w'}$. As expected, the stresses are particularly large in the region underneath and inside the roller. Although measurements were not obtained from the uppermost part of the roller itself, we can get a fair estimate of the τ_{yx}-variation by assuming the shear stresses along the mean water surface are close to zero.

Figure 3.11 shows, when measured in terms of ρU_1^2 versus x/ℓ_r, the shear stresses along the dividing streamline in the three hydraulic jumps largely exhibit

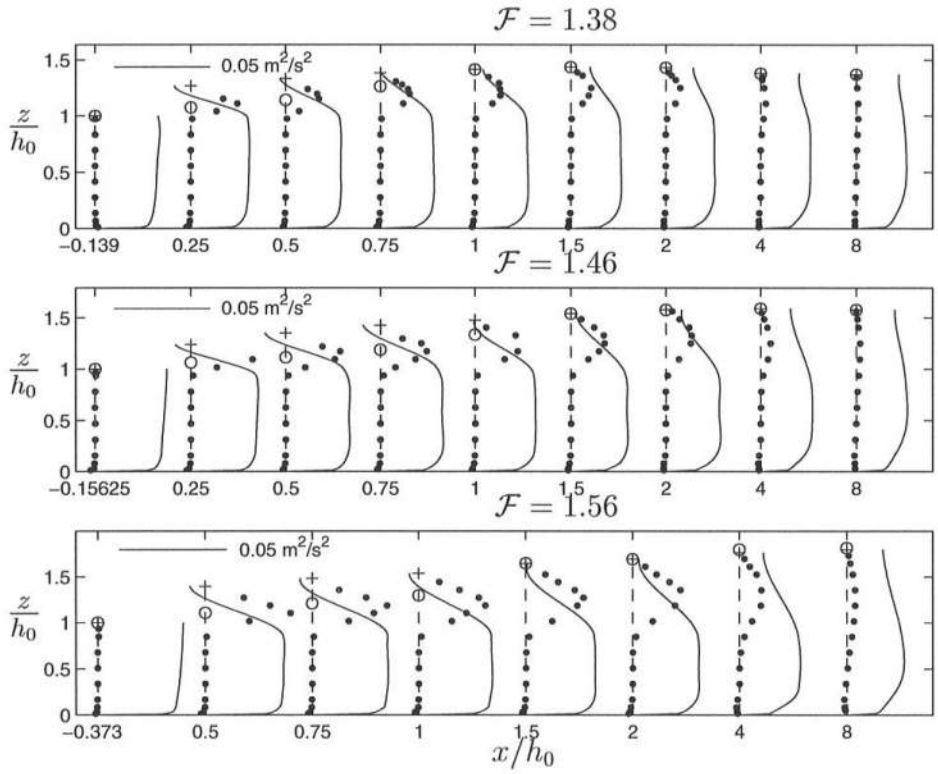

Figure 3.10: Measured values of $\widetilde{u'w'}$ (•), the curve fits for the velocity (———), the mean water surface (+) and the dividing streamline (○).

the same variation over the length of the roller. This similarity is equivalent to the similarity found for the variation of the vertical roller thickness e (see figure 3.8) and may not apply for jumps with significantly larger $\mathcal{F}$ values.

3.2.5 Vorticity, Stresses and Eddy Viscosity

It is also of significant interest to analyze the development of the vorticity in the flow. The vorticity

$$\omega = \frac{\partial u}{\partial z} - \frac{\partial w}{\partial x} \tag{3.63}$$

is obtained from the curve-fitted measured velocities. Since measurements were obtained only along a few verticals, it requires some care to determine $\partial w/\partial x$. However, the vertical velocities are small and vary relatively slowly in the x direction.

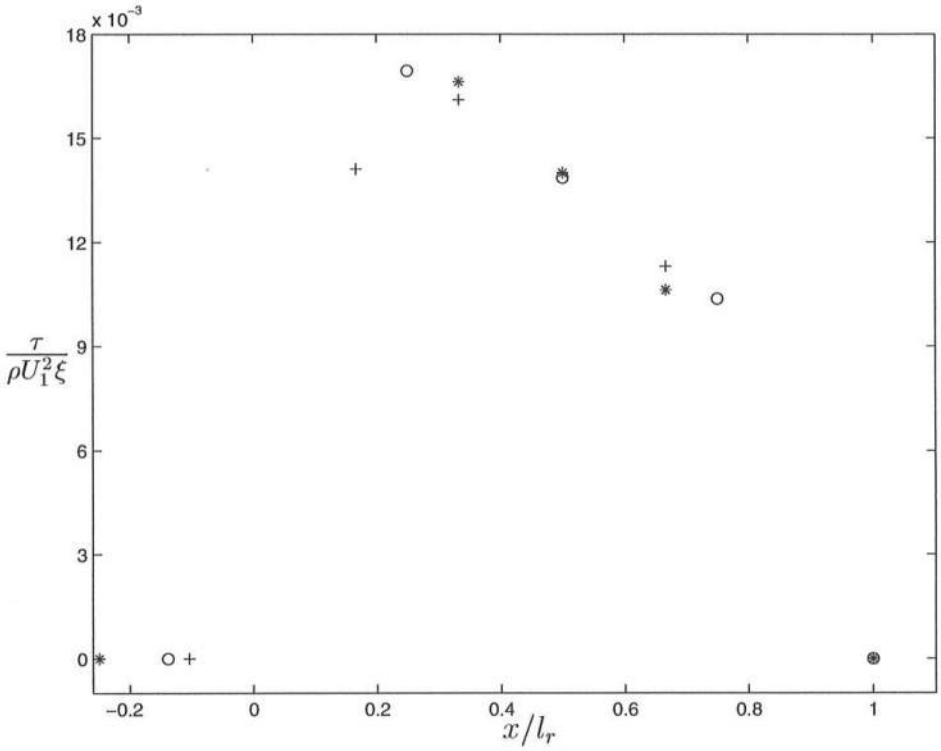

Figure 3.11: Non-dimensional shear stresses along the lower limit of the roller for all three jumps. ∘ jump no 1, × jump no 2, ⋆ jump no 3

Therefore, the values of $\partial w/\partial x$ were negligible in comparison to $\partial u/\partial z$. Figure 3.12 shows the vorticity along the verticals where measurements were taken.

Qualitatively, these results confirm the patterns for the breaking waves behind a hydrofoil found by Lin and Rockwell (1994) (for those of their cases where capillary effects are negligible). A quantitative comparison is difficult because generating conditions for the two flows are very different.

It is clear that vorticity generation is initiated at the toe of the turbulent front where the high speed flow along the incoming free surface streamline meets the fluid slowly moving down along the surface of the roller. Because of its high speed, the incoming flow seems to continue undisturbed over a short distance underneath the roller. By careful observation, one gets the impression that the first very short part of the roller essentially floats on the incoming high speed fluid over what seems to be

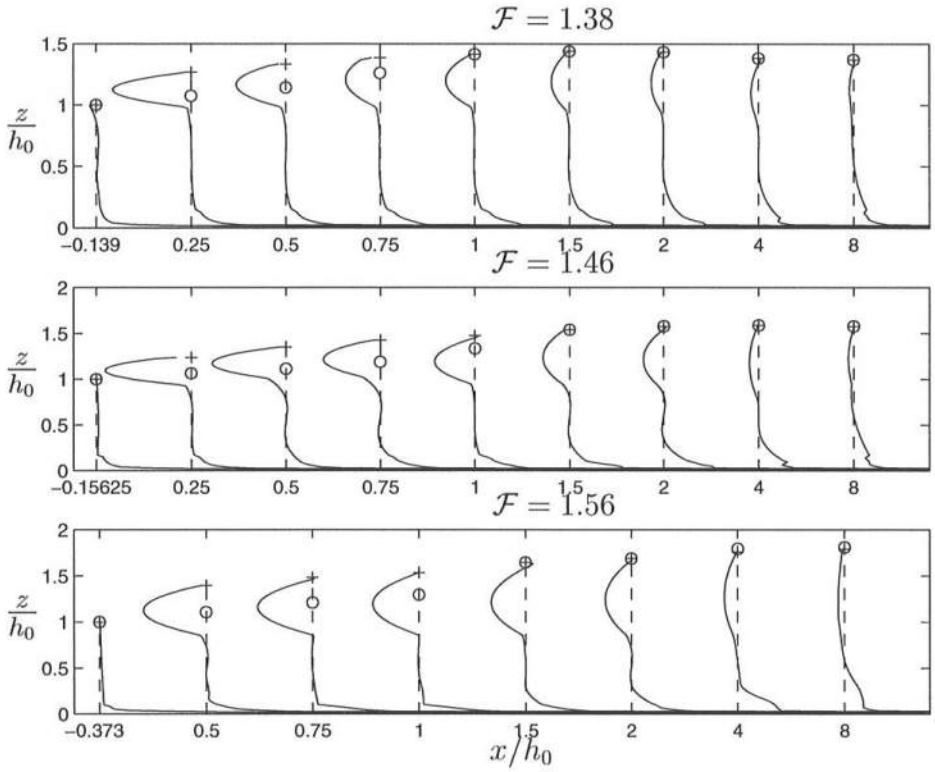

Figure 3.12: The vorticity distributions determined from the measurements.

a very thin highly aerated layer where all the shear is located. Another interesting feature, apparent from the figure, is that the vorticity generated by the roller and by the bottom boundary layer are clearly demarcated except far downstream of the jump. For a wave, the boundary layer is expected to be smaller than that observed in steady hydraulic jumps (see Cox *et al.* 1995). Thus, by omitting the effects of the bottom boundary, as we have in the model, no significant error would be introduced in the breaking model.

The momentum balance for the flow around the toe was discussed by Svendsen and Madsen (1984). They pointed out that, in spite of the fact that theoretically the shear at the toe becomes infinitely large, the shear stress must for dynamical reasons remain bounded at the toe (and in fact must go to zero as $e \to 0$). This can be accomplished by assuming that the effective (turbulent) viscosity ν_t goes to

zero faster than the shear. In accordance with the fact that both the length scale ℓ and the kinetic energy k per unit mass must start at zero values at the toe, we can think of ν_t as being $\ell\sqrt{k}$.

A small distance further into the roller, the incoming flow becomes unstable and the mean incoming streamline becomes the center in a flow pattern that has resemblances of a mixing layer (Peregrine and Svendsen 1978). As the mixing develops, the magnitude of the fluctuations develop to a size that is comparable to the thickness of the roller and they start interacting with the free surface. This occurs in the central part of the roller which is undoubtedly the area where the strongest production of turbulence takes place.

It is interesting that, along the streamline that divides the roller with recirculating flow from the rest of the essentially unidirectional flow, the vorticity in all the three jumps seems to follow the same dimensionless variation. This is illustrated in figure 3.13 which shows values of $\omega' = \omega h_2 \xi / U_1$ versus x/ℓ_r where ℓ_r is the roller length. The value of ω' increases rapidly from the toe to a maximum which is reached already about 10% of ℓ_r into the roller. From there the vorticity decreases almost linearly to the zero value at the end of the roller where the dividing streamline meets the free surface.

To some extent this confirms that the flow has many resemblances with a shear layer positioned along the streamline. We see from figure 3.10 and figure 3.12 that along most of the roller both the shear stresses and the vorticity are maximum along the dividing streamline. This leads to the interpretation that the center for vorticity generation is along the dividing streamline that forms the lower limit of the roller. Figure 3.13 indicates that the strength of that generating process decreases linearly over most of the roller length. From this generating source of decreasing strength the vorticity would spread downward (and upward) by diffusive mechanisms (mainly turbulent mixing). We therefore expect that from some point downstream the maximum vorticity would be found at a level below the dividing streamline (i.e. "inside" the flow). This is confirmed by the measurements. Towards the rear of the roller the maximum values of both ω (figure 3.12) and $\widetilde{u'w'}$ (figure 3.10) occur below the lower limit of the roller. Notice that the reason why no equivalent maximum

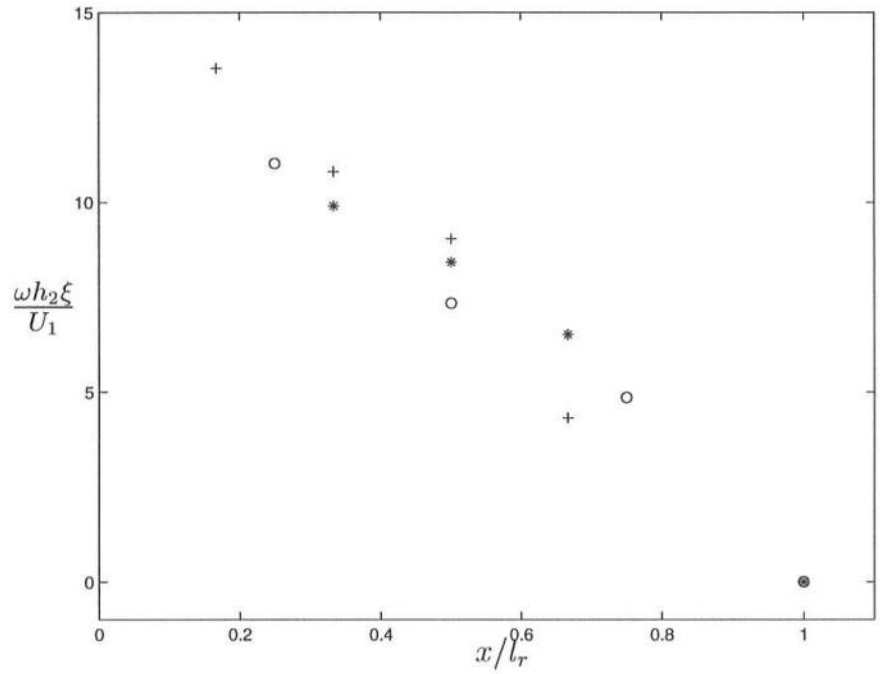

Figure 3.13: Dimensionless vorticity $\omega' = \omega h_2 \xi / U_1$ versus x/ℓ_r along the lower limit of the roller for all three jumps. ∘ jump no 1, × jump no 2, ⋆ jump no 3.

forms above (i.e. inside the roller) is probably because the roller turbulence is so strong that equilibrium between the source strength and the zero vorticity along the free surface is established almost instantly.

Hence, this model differs from a traditional shear layer in that vorticity generation essentially stops at or before the end of the roller. Downstream from that point the vorticity distribution is essentially formed by the diffusion of vorticity away from the maximum inside the flow towards both the surface and the bottom boundaries and upward from the bottom boundary layer. Eventually - sufficiently far downstream - the flow will attain the characteristics of a (nearly) uniform open channel flow dominated by the bottom generated turbulence and friction. Note however from figure 3.12 that even at $x/h_1 = 8$ this point of equilibrium is not quite reached. There is still residual vorticity from the roller, and the bottom boundary layer still has only spread over 40–50% of the full depth.

While the results for the vorticity for the upper part of the roller are based on the extrapolations of the curve-fitted velocity profiles, we see that the variations of ω over the roller are reasonable. In particular, the assumption of a zero velocity gradient at the surface, which lead to a zero vorticity there, appears in accordance with the vorticity profiles as a whole. In reality, neither the velocity gradients (i.e. the vorticities) nor the shear stresses will be exactly zero at the mean water surface. This is due to the turbulent fluctuations of the free surface which give non-zero contributions to the averages at the mean surface. This problem was discussed by Brocchini and Peregrine (1998) but the available measurements do not provide sufficient information to analyze the details. Even so, it is expected that the contributions are relatively insignificant in comparison to the stresses and vorticity in the lower part of the roller.

It is also seen that in spite of the smooth bottom, the bottom boundary layer produces a fair amount of vorticity, and a fair amount of turbulent kinetic energy. Finally, with the shear stress at the bottom of the roller scaling as $\tau/\rho U_1^2$ and the vorticity being close to $\partial u/\partial z$ and scaling as $\omega h_2 \xi / U_1$, one may expect that the eddy viscosity along the roller bottom scales as $\nu_t / U_1 h_2 \xi$. Figure 3.14 shows that there is considerable variability in the magnitude of ν_t. Such variability for related quantities such as the turbulent kinetic energy and the turbulent length scale has been observed in the surf zone (Cox *et al.* 1995). We can also express ν_t as

$$\hat{\nu}_t = \nu_t' U_1 h_2 \xi = \nu_t' \mathcal{F} \xi^2 h_1 \sqrt{g h_1}, \tag{3.64}$$

where the $\hat{()}$ denotes the dimensional quantity. Traditionally, the eddy viscosity is scaled as

$$\hat{\nu}_t = \nu_t h \sqrt{gh}, \tag{3.65}$$

which gives $\nu_t \simeq \nu_t' \mathcal{F} \xi^2$. For surf zone waves, $\xi \sim 2$ which gives a Froude number $\mathcal{F} \sim 1.75$. Thus, ν_t obtained from the hydraulic jump measurements is $0.021 h\sqrt{gh}$ and $0.046 h\sqrt{gh}$ which is the same range usually obtained in the surf zone (Cox *et al.* 1995).

It is also possible from the measurements of velocities and shear stresses to get an estimate for a value of the eddy viscosity ν_t over the entire vertical at each x where

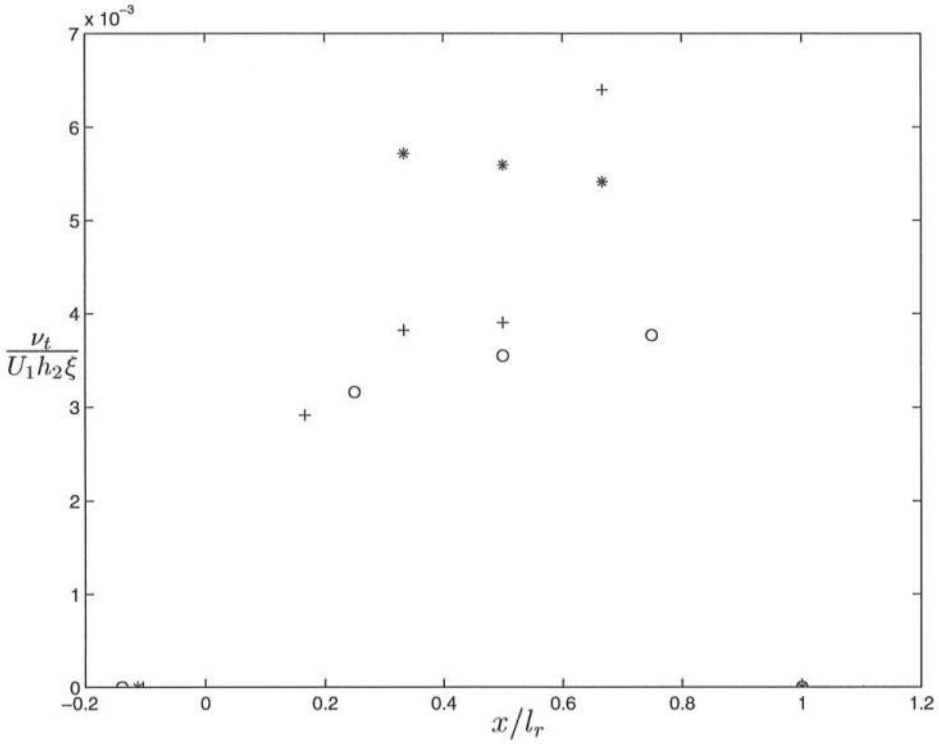

Figure 3.14: The dimensionless eddy viscosity $\nu_t/U_1 h_2 \xi$ versus x/ℓ_r along the lower limit of the roller for all three jumps. ∘ jump no 1, + jump no 2, ⋆ jump no 3.

measurements were taken. Assuming ν_t is defined by the equation $\tau_{zx} = \rho\nu_t \partial u/\partial z$ we get the values shown in figure 3.15 for ν_t. To avoid the singularities at $\tau = 0$ in the computation for this figure, we have set $\nu_t = 0$ when τ becomes sufficiently small. There is no clear relationship for the vertical distribution of eddy viscosity, which can be discerned from the figure. It does indicate that the value is reasonably constant in the region where significant shear stresses are present and decreases with the magnitude of the shear stress.

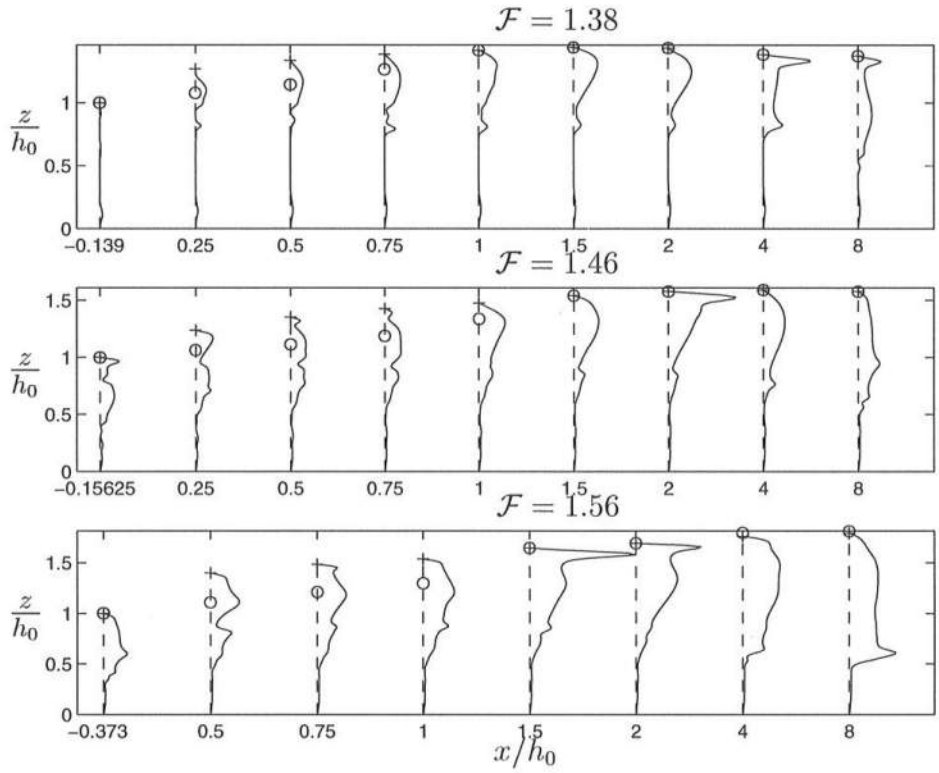

Figure 3.15: The eddy viscosity variations (———) determined from the measured shear stresses and the calculated vertical velocity gradients.

Chapter 4

NUMERICAL SOLUTION TO THE GOVERNING EQUATIONS.

In the preceding chapters, the modified Boussinesq equations that describe waves breaking in shallow water were presented. These equations are non-linear partial differential equations involving three variables. No analytical methods have been developed thus far to solve these equations. Instead, numerical methods have to be employed to get approximate solutions.

A variety of numerical methods is available to solve these types of equations. In general, finite-difference schemes are preferred over other methods. This is in part due to the ease of implementation for practical purposes.

Peregrine (1967) used a simple second-order finite difference scheme for Boussinesq equations to study the propagation of solitary waves. The scheme used central difference techniques to evaluate the spatial derivatives and a simple forward stepping scheme for the time derivatives. The truncation errors that result from this scheme have the same form as the dispersive term in the equation. Hence, small values of the grid spacing Δx and time step Δt were required to obtain accurate results.

Abbot *et al.* (1973) developed a more sophisticated scheme to solve the Boussinesq equations. This method (System 21, Jupiter) used a second-order time-centered implicit scheme. The truncation errors due to the finite differencing, which have the same mathematical form as the terms in the original equations, are substituted back into the model. This back-substitution technique improved the accuracy of the scheme. Subsequently, adaptations of this method have been used by various researchers (see, e.g., Karambas *et al.* 1990, Madsen *et al.* 1991).

A space-staggered and time-staggered scheme was used by Brocchini *et al.* (1992). This scheme involved calculation of the variables at staggered half-steps in time. The method is also a mixture of an explicit scheme (for the continuity equation) and an implicit scheme (for the momentum equation).

Wei *et al.* (1995) used a predictor-corrector scheme based on the third-order Adams-Bashforth predictive method and the fourth-order Adams-Moulton corrective step. The spatial differencing is such that the truncation errors do not have any third derivatives. This means that back substitution is not necessary to improve the accuracy of the model. This scheme was adapted by Yu (1996) to solve the Boussinesq equations with wave breaking. Gobbi *et al.* (1999) extended this scheme to a fifth-order predictor and a sixth-order corrector scheme to solve Boussinesq equations accurate up to $O(\mu^4)$.

In all these models, at each time step a tridiagonal matrix system is used to solve for either the volume flux (or velocity) in the momentum equation or the surface elevation in the continuity equation. The use of a tridiagonal system stabilizes the scheme without affecting the computational time.

For the model described herein, the predictor-corrector scheme of Wei *et al.* (1995) is adapted. This is an explicit scheme; hence more convenient to apply. The numerical scheme is described in the first section. A linear stability analysis is also performed for the particular form of the Boussinesq equations used here.

For actual applications of the model, boundary conditions are required at both the offshore and shoreward boundary. Again, a number of methods are available for incorporating these boundary conditions, each with its own particular advantages and disadvantages. In the present version of the model, we have a shelf at the shoreward boundary with a small water depth and a sponge layer to absorb the breaking waves at this location. The boundary conditions are described in the next section. This includes the generation mechanism at the offshore boundary, the absorption mechanism close to the shoreline and the boundary conditions for the vorticity transport equation.

4.1 The finite difference scheme.

The first- and third-order spatial derivative terms are discretized using the standard five-point central difference scheme in the interior of the domain. For the first-order derivatives, this leads to truncation errors of $O(\Delta x^4/\mu^2)$ relative to the dispersive terms, where Δx is the size of the spatial grid. The dispersive terms, which are third-order derivatives, give truncation errors of $O(\Delta x^2)$ relative to the original dispersive terms.

The governing equations are written in a form that makes it convenient to apply the numerical scheme. The continuity and momentum equations are written as

$$\zeta_t = E \tag{4.1a}$$

$$U_t = F \tag{4.1b}$$

For the weakly nonlinear model (which is a $\zeta - Q$ version) given by (2.8) and (2.51)

$$E = -Q_x, \tag{4.2a}$$

$$U = Q + \left(B - \frac{1}{2}\right) h^2 (Q)_{xx} + \frac{h^3}{6}\left(\frac{Q}{h}\right)_{xx}, \tag{4.2b}$$

$$F = -g(h+\zeta)\zeta_x - \left(\frac{Q^2}{h+\zeta}\right)_x - Bgh^2 h\,(\zeta_x)_{xx} - (\Delta M)_x - (\Delta P)_{xxt} + D_s + F_{sp}, \tag{4.2c}$$

where F_{sp} is the term that includes the effect of the absorbing boundary at the shoreline. This term will be discussed later in this chapter. For the fully non-linear model (which is a $\zeta - \overline{u}$ version) given by (2.53) and (2.72)

$$E = -\left[(h+\zeta)\,\overline{u}\right]_x, \tag{4.3a}$$

$$U = \overline{u} + \left[\left(B - \frac{1}{3}\right) h^2 \overline{u}_{xx} - \frac{1}{2} h h_{xx} \overline{u} - h h_x \overline{u}_x\right], \tag{4.3b}$$

$$F = F'(\zeta, \overline{u}) + F^t(\zeta, \overline{u}_t) + F^b + F_{sp}, \tag{4.3c}$$

where

$$F' = -\overline{u}\overline{u}_x - g\zeta_x - B\mu^2 h^2 \zeta_{xxx}$$

$$\frac{1}{3}h^2\overline{uu}_{xxx} - \frac{1}{3}h^2\overline{u}_x\overline{u}_{xx} + \frac{3}{2}hh_{xx}\overline{uu}_x + \frac{1}{2}hh_{xxx}\overline{u}^2 + hh_x\overline{uu}_{xx}$$
$$- Bh^2\left(\overline{uu}_x\right)_{xx} + \frac{1}{3}h\zeta\overline{u}_x\overline{u}_{xx} + \frac{1}{3}h\overline{u}_{xx}\left(\zeta\overline{u}\right)_x - h\left(\zeta\overline{u}_x^2\right)_x + \frac{2}{3}h\left(\zeta\overline{uu}_{xx}\right)_x$$
$$+ \zeta_x h_{xx}\overline{u}^2 + \zeta h_x\overline{uu}_{xx} + \frac{1}{2}\zeta h_{xxx}\overline{u}^2 + \frac{3}{2}\zeta h_{xx}\overline{uu}_x + \zeta_x h_x\overline{uu}_x$$
$$+ \frac{1}{3}\zeta^2\overline{uu}_{xxx} + \zeta\zeta_x\overline{uu}_{xx} - \zeta\zeta_x\overline{u}_x^2 - \frac{1}{3}\zeta^2\overline{u}_x\overline{u}_{xx}, \tag{4.3d}$$

$$F^t = h\zeta_x\overline{u}_{tx} + \frac{2}{3}h\zeta(\overline{u}_t)_{xx} - \zeta h_x(\overline{u}_t)_x + h_x\zeta_x\overline{u}_t + \frac{1}{2}\zeta h_{xx}\overline{u}_t$$
$$- \frac{1}{6}\zeta^2(\overline{u}_t)_{xx} + \frac{1}{2}\left(\zeta^2(\overline{u}_t)_x\right)_x, \tag{4.3e}$$

$$F^b = -\left(\Delta M\right)_x - \left(\Delta P\right)_{xxt} + D_s - \left(\Delta M_1\right)_x + D_w + D_{uw}. \tag{4.3f}$$

Notice that in the numerical scheme for the fully non-linear set of equations, the linear terms involving $\partial/\partial t$ are included in U in the numerical scheme, whereas the non-linear terms involving $\partial/\partial t$ are retained (F^t) in the right hand side of the numerical equation. This facilitates the use of a tridiagonal system to solve for $\overline{u}$, at every time step, using the value obtained for U. As mentioned before, the use of this tridiagonal system makes the numerical procedure more stable.

The fourth-order Adams-Bashforth-Moulton (ABM) (Press *et al.* 1992) time-stepping scheme at the predictor stage reads, for (4.1),

$$\zeta_i^{n+1} = \zeta_i^n + \frac{\Delta t}{12}\left[23E_i^n - 16E_i^{n-1} + 5E_i^{n-2}\right], \tag{4.4a}$$

$$U_i^{n+1} = U_i^n + \frac{\Delta t}{12}\left[23F_i^n - 16F_i^{n-1} + 5F_i^{n-2}\right]. \tag{4.4b}$$

At the corrector stage, the equation reads

$$\zeta_i^{n+1} = \zeta_i^n + \frac{\Delta t}{24}\left[9E_i^{n+1} + 19E_i^n - 5E_i^{n-1} + E_i^{n-2}\right], \tag{4.5a}$$

$$U_i^{n+1} = U_i^n + \frac{\Delta t}{24}\left[9F_i^{n+1} + 19F_i^n - 5F_i^{n-1} + F_i^{n-2}\right]. \tag{4.5b}$$

This time stepping scheme is accurate to $O(\Delta t)^3$ at the predictor stage and up to $O(\Delta t)^4$ at the corrector stage. Notice that in the fully non-linear model, the time derivatives of $\overline{u}$ in F^t are solved explicitly. Consistent with the accuracy of the ABM scheme mentioned above, the u_t term in F_t is evaluated at the predictor stage as

$$(\overline{u}_t)_i^n = \frac{1}{2\Delta t}\left[3\overline{u}_i^n - 4\overline{u}_i^{n-1} + \overline{u}_i^{n-2}\right], \tag{4.6a}$$

$$(\overline{u}_t)_i^{n-1} = \frac{1}{2\Delta t}\left[\overline{u}_i^n - \overline{u}_i^{n-2}\right], \tag{4.6b}$$

$$(\overline{u}_t)_i^{n-2} = -\frac{1}{2\Delta t}\left[3\overline{u}_i^{n-2} - 4\overline{u}_i^{n-1} + \overline{u}_i^n\right], \tag{4.6c}$$

and at the corrector stage

$$(\overline{u}_t)_i^{n+1} = \frac{1}{6\Delta t}\left[11\overline{u}_i^{n+1} - 18\overline{u}_i^n + 9\overline{u}_i^{n-1} - 2\overline{u}_i^{n-2}\right], \tag{4.7a}$$

$$(\overline{u}_t)_i^{n} = \frac{1}{6\Delta t}\left[2\overline{u}_i^{n+1} + 3\overline{u}_i^n - 6\overline{u}_i^{n-1} + \overline{u}_i^{n-2}\right], \tag{4.7b}$$

$$(\overline{u}_t)_i^{n-1} = -\frac{1}{6\Delta t}\left[2\overline{u}_i^{n-2} + 3\overline{u}_i^{n-1} - 6\overline{u}_i^n + \overline{u}_i^{n+1}\right], \tag{4.7c}$$

$$(\overline{u}_t)_i^{n-2} = -\frac{1}{6\Delta t}\left[11\overline{u}_i^{n-2} - 18\overline{u}_i^{n-1} + 9\overline{u}_i^n - 2\overline{u}_i^{n+1}\right]. \tag{4.7d}$$

The truncation errors for the time derivatives in the predictor step are $O(\Delta t^2)$ and at the corrector step $O(\Delta t^3)$. At the corrector stage, the value of F^t has to be computed anew at every iteration.

For the spatial derivatives in the interior region, a five-point central difference scheme is used to calculate the first- and third-order derivatives and a three-point scheme is used to calculate the second-order derivatives (Anderson *et al.* 1984). For the continuity equation, one-sided schemes are used to evaluate the derivatives at the boundary. Thus, if N is the total number of grid points in the domain,

$$(w_x)_1 = \frac{1}{12\Delta x}\left[-25w_1 + 48w_2 - 36w_3 + 16w_4 - 3w_5\right], \tag{4.8a}$$

$$(w_x)_2 = \frac{1}{12\Delta x}\left[-3w_1 - 10w_2 + 18w_3 - 6w_4 + w_5\right], \tag{4.8b}$$

$$(w_x)_i = \frac{1}{12\Delta x}\left[-w_{i+2} + 8w_{i+1} - 8w_{i-1} + w_{i-2}\right], \tag{4.8c}$$

$$(i = 3, 4, \cdots, N-3, N-2),$$

$$(w_x)_{N-1} = -\frac{1}{12\Delta x}\left[-3w_N - 10w_{N-1} + 18w_{N-2} - 6w_{N-3} + w_{N-4}\right], \tag{4.8d}$$

$$(w_x)_N = -\frac{1}{12\Delta x}\left[-25w_N + 48w_{N-1} - 36w_{N-2} + 16w_{N-3} - 3w_{N-4}\right], \tag{4.8e}$$

where $w = (h+\zeta)\overline{u}$. The truncation errors in this scheme are $O(\Delta x^4)$. However, in the momentum equation, use of the one-sided schemes leads to instabilities in the results after a short time. This is true especially for the fully non-linear equations when the incoming waves at the boundary have high non-linearity. Therefore, a

lower order spatial difference scheme is used at the boundary for the momentum equation. Thus,

$$(w_x)_1 = \frac{1}{2\Delta x}\left[3w_1 - 4w_2 + w_3\right], \tag{4.9a}$$

$$(w_x)_2 = \frac{1}{2\Delta x}\left[w_3 - w_1\right], \tag{4.9b}$$

$$(w_x)_i = \frac{1}{12\Delta x}\left[-w_{i+2} + 8w_{i+1} - 8w_{i-1} + w_{i-2}\right], \tag{4.9c}$$

$$(i = 3, 4, \cdots, N-3, N-2),$$

$$(w_x)_{N-1} = -\frac{1}{2\Delta x}\left[w_{N-2} - w_N\right], \tag{4.9d}$$

$$(w_x)_N = -\frac{1}{2\Delta x}\left[3w_{N-2} - 4w_{N-1} + w_N\right], \tag{4.9e}$$

where w denotes the variables $\{\zeta, \overline{u}, h\}$ subject to finite differencing. The truncation errors are $O(\Delta x^2)$ at the boundaries and $O(\Delta x^4)$ in the interior region. For the second derivatives, a three-point finite difference scheme is used in the interior region and four-point one-sided schemes are used at the boundaries.

$$(w_{xx})_1 = \frac{1}{(\Delta x)^2}\left[2w_1 - 5w_2 + 4w_3 - w_4\right], \tag{4.10a}$$

$$(w_{xx})_i = \frac{1}{(\Delta x)^2}\left[w_{i+1} - 2w_i + w_{i-1}\right], \tag{4.10b}$$

$$(i = 2, 3, \cdots, N-2, N-1),$$

$$(w_{xx})_N = -\frac{1}{(\Delta x)^2}\left[2w_N - 5w_{N-1} + 4w_{N-2} - w_{N-3}\right]. \tag{4.10c}$$

The truncation errors are of $O(\Delta x^2)$ in the entire domain. And finally for the third-order derivatives, five-point schemes which have truncation errors of $O(\Delta x^2)$ are

$$(w_{xxx})_1 = \frac{1}{(\Delta x)^2}\left[(w_x)_1 - 2(w_x)_2 + (w_x)_3\right], \tag{4.11a}$$

$$(w_{xxx})_2 = \frac{1}{(\Delta x)^2}\left[(w_x)_3 - 2(w_x)_2 + (w_x)_1\right], \tag{4.11b}$$

$$(w_{xxx})_i = \frac{1}{2\Delta x^3}\left[w_{i+2} - 2w_{i+1} + 2w_{i-1} - w_{i-2}\right], \tag{4.11c}$$

$$(i = 3, 4, \cdots, N-3, N-2),$$

$$(w_{xxx})_{N-1} = \frac{1}{(\Delta x)^2}\left[(w_x)_N - 2(w_x)_{N-1} + (w_x)_{N-2}\right], \tag{4.11d}$$

$$(w_{xxx})_N = \frac{1}{(\Delta x)^2}\left[(w_x)_N - 2(w_x)_{N-1} + (w_x)_{N-2}\right]. \tag{4.11e}$$

The value of U at each time level is obtained from the solution to the momentum equation. Once U is determined, we then need to solve (4.2b) or (4.3b) to obtain Q or $\overline{u}$ respectively. For the fully non-linear model, we discretize the ODE (4.3b) using (4.10) for the second derivative of $\overline{u}$ and a simple three-point central difference scheme for the first derivative of $\overline{u}$ to give

$$U_i^{n+1} = A_{i-1}\overline{u}_{i-1}^{n+1} + B_i\overline{u}_i^{n+1} + C_{i+1}\overline{u}_{i+1}^{n+1}, \tag{4.12}$$

where

$$A_i = \left(B - \frac{1}{3}\right)\frac{h_i^2}{\Delta x^2} + \frac{h_i(h_x)_i}{2\Delta x}, \tag{4.13a}$$

$$B_i = \left(1 - \frac{1}{2}h_i(h_{xx})_i\right) - 2\left(B - \frac{1}{3}\right)\frac{h_i^2}{\Delta x^2}, \tag{4.13b}$$

$$C_i = \left(B - \frac{1}{3}\right)\frac{h_i^2}{\Delta x^2} - \frac{h_i(h_x)_i}{2\Delta x}. \tag{4.13c}$$

This tridiagonal system is solved using the LU-decomposition method (Press *et al.* 1992). Equation (4.12) is solved at each time step $(n+1)$ to give the value of $\{\overline{u}_i^{n+1}\}$. This value of $\overline{u}$ is used to calculate the water surface elevation from the continuity equation. The procedure to obtain Q from (4.2b) for the weakly non-linear equations is exactly the same.

In the momentum equation, the value of $\overline{u}$ is prescribed at the boundaries. Therefore, U is evaluated only for $i = 2, 3, \cdots, N-2, N-1$. The continuity equation gives the water surface elevation at every point including the boundaries.

4.1.1 Time-integration of the vorticity solution.

The analytical expression for the vorticity was given previously by (3.26) as

$$\omega = \sigma\omega_s + \sum_{n=1}^{\infty}\left[G_n^{(1)} + G_n^{(2)}\right]\sin n\pi\sigma, \tag{4.14}$$

where $G_n^{(1)}$ and $G_n^{(2)}$ are integrals in time. These integrals have to be solved at each time step. The general form for either quantity is written as

$$G_n(t) = \int_0^t F_n e^{n^2\pi^2\kappa(\tau-t)}\, d\tau. \tag{4.15}$$

At time $t + dt$,

$$\begin{aligned} G_n(t+dt) &= \int_0^{t+dt} F_n e^{n^2\pi^2\kappa(\tau-t-dt)}\, d\tau \\ &= e^{-n^2\pi^2\kappa dt} G_n(t) + \int_t^{t+dt} F_n e^{n^2\pi^2\kappa(\tau-t-dt)}\, d\tau. \end{aligned} \tag{4.16}$$

The second term is integrated numerically. The direct trapezoidal method for discrete integration is quite inaccurate for evaluating this expression. The reason for the inaccuracy is that in that method, the entire integrand would be approximated with a linear polynomial between t and $t + dt$. To use more points for increased accuracy implies that the values at the previous time steps will have to be stored. Instead, a more efficient integration scheme is used in which only the quantity F_n is approximated by a linear function

$$F_n(\tau) = m\tau + c. \tag{4.17}$$

We now substitute (4.17) into the integral in (4.16) and solve to get

$$\begin{aligned} G_n(t+dt) &= e^{-\alpha_2 dt} G_n(t) + \frac{e^{-\alpha_2(t+dt)}}{\alpha_2^2} \left[e^{\alpha_2\tau}\left(\alpha_2 F_n(\tau) - m\right)\right]_t^{t+dt} \\ &= e^{-\alpha_2 dt} G_n(t) + \frac{F_n(t+dt) - m}{\alpha_2^2} - e^{-\alpha_2 dt}\frac{F_n(t) - m}{\alpha_2^2}, \end{aligned} \tag{4.18}$$

where $\alpha_2 = n^2\pi^2\kappa$ and $m = (F_n(t+dt) - F_n(t))/dt$. This expression is evaluated at each time step to update the vorticity at each x-location.

4.1.2 Linear stability analysis.

The governing equations are a system of non-linear partial differential equations and the discretization scheme is complex. The classical methods for stability analysis are not sufficient in this case. Yu (1996) chose to determine the stability of the scheme by numerical experiments. Linear stability analysis for the $\zeta - u_\alpha$

model was performed by Wei and Kirby (1998) for the same scheme given above. The model equations are slightly different in this case and some insight into the model can be gained by performing a linear stability analysis. The stability analysis, obtained by applying the method of von Neumann (Twizell 1984), is performed on a horizontal bottom for the $\zeta - \overline{u}$ version of the model. The linearized governing equations are

$$\zeta_t = E = h\overline{u}_x, \tag{4.19}$$

$$U_t = F = -g\zeta_x - Bgh^2\zeta_{xxx}, \tag{4.20}$$

where

$$U = \overline{u} + \alpha h^2 \overline{u}_{xx}, \tag{4.21}$$

$$\alpha = B - \frac{1}{3}. \tag{4.22}$$

The range of stability for the predictor scheme and corrector scheme taken separately will be different than that obtained by a combination of the two. Furthermore, the range of stability also depends on the number times the corrector step is performed for one time step. For actual applications of the model, the number of iterations is a function of the relative error at any given time, and hence may be different at each time step. The stability range is expected to be larger for more number of iterations, i.e., if the corrector step is used more than once. In this study, the stability analysis is performed for the case of one predictor stage and one corrector stage.

At the predictor stage, the discretized equations are expressed as

$$\zeta_j^{(n+1)*} = \zeta_j^n + \frac{\Delta t}{12}\left[23E_j^n - 16E_j^{n-1} + 5E_j^{n-2}\right], \tag{4.23}$$

$$U_j^{(n+1)*} = U_j^n + \frac{\Delta t}{12}\left[23F_j^n - 16F_j^{n-1} + 5F_j^{n-2}\right], \tag{4.24}$$

where $(n+1)*$ corresponds to the predicted values; n, $n-1$ and $n-2$ are the temporal locations at which the values of ζ and $\overline{u}$ are available. At any given point in space and time, ζ and $\overline{u}$ are expressed in terms of their Fourier component

$$\zeta_j^n = \zeta_0 \exp\left[i(kj\Delta x - \omega n\Delta t)\right], \tag{4.25}$$

$$\overline{u}_j^n = \overline{u}_0 \exp\left[i(kj\Delta x - \omega n\Delta t)\right], \tag{4.26}$$

where j and n refers to the spatial and temporal grid points, $i = \sqrt{-1}$, k is the wave number and ω is the frequency. From (4.25) and (4.26),

$$\begin{aligned} U_j^n &= \overline{u}_j^n + \frac{\alpha h^2}{\Delta x^2}\left(\overline{u}_{j+1}^n - 2\overline{u}_j^n + \overline{u}_{j-1}^n\right) \\ &= \overline{u}_j^n \left[1 - \frac{4\alpha h^2}{\Delta x^2}\sin^2\left(\frac{k\Delta x}{2}\right)\right], \end{aligned} \tag{4.27}$$

$$\begin{aligned} \left(\overline{u}_x\right)_j^n &= \frac{1}{12\Delta x}\left[-\overline{u}_{j+2}^n + 8\overline{u}_{j+1}^n - 8\overline{u}_{j-1}^n + \overline{u}_{j-2}^n\right] \\ &= \frac{i\sin\left(k\Delta x\right)}{3\Delta x}\left[4 - \cos\left(k\Delta x\right)\right]\overline{u}_j^n, \end{aligned} \tag{4.28}$$

$$\left(\zeta_x\right)_j^n = \frac{i\sin\left(k\Delta x\right)}{3\Delta x}\left[4 - \cos\left(k\Delta x\right)\right]\zeta_j^n, \tag{4.29}$$

$$\begin{aligned} \left(\zeta_{xxx}\right)_j^n &= \frac{1}{\Delta x^3}\left[\overline{u}_{j+2}^n - 2\overline{u}_{j+1}^n + 2\overline{u}_{j-1}^n - \overline{u}_{j-2}^n\right] \\ &= -\left[\frac{4i\sin\left(k\Delta x\right)}{\Delta x^3}\sin^2\left(k\Delta x\right)\right]\zeta_j^n. \end{aligned} \tag{4.30}$$

Substituting these expressions into (4.23) and (4.24) results in

$$\zeta_j^{(n+1)*} = \zeta_j^n + p\left(46\overline{u}_j^n - 32\overline{u}_j^{n-1} + 10\overline{u}_j^{n-2}\right), \tag{4.31}$$

$$\overline{u}_j^{(n+1)*} = \overline{u}_j^n + q\left(46\zeta_j^n - 32\zeta_j^{n-1} + 10\zeta_j^{n-2}\right), \tag{4.32}$$

where

$$p = -\frac{ih\Delta t}{24\Delta x}\sin k\Delta x\left[\frac{4 - \cos\left(k\Delta x\right)}{3}\right], \tag{4.33}$$

$$q = -\frac{ig\Delta t}{24\Delta x}\frac{\sin k\Delta x}{r}\left[\frac{4 - \cos\left(k\Delta x\right)}{3} - \frac{4Bh^2}{\Delta x^2}\sin^2\left(\frac{k\Delta x}{2}\right)\right], \tag{4.34}$$

$$r = 1 - \frac{4\alpha h^2}{\Delta x^2}\sin^2\left(\frac{k\Delta x}{2}\right). \tag{4.35}$$

The corrector step is

$$\zeta_i^{n+1} = \zeta_i^n + \frac{\Delta t}{24}\left[9E_i^{(n+1)*} + 19E_i^n - 5E_i^{n-1} + E_i^{n-2}\right], \tag{4.36}$$

$$U_i^{n+1} = U_i^n + \frac{\Delta t}{24}\left[9F_i^{(n+1)*} + 19F_i^n - 5F_i^{n-1} + F_i^{n-2}\right], \tag{4.37}$$

where $(n+1)*$ corresponds to the value obtained from the predictor step. Following the same procedure as for the predictor step gives

$$\zeta_j^{n+1} = \zeta_j^n + p\left(9\overline{u}_j^{(n+1)*} + 19\overline{u}_j^n - 5\overline{u}_j^{n-1} + \overline{u}_j^{n-2}\right), \tag{4.38}$$

$$\overline{u}_j^{n+1} = \overline{u}_j^n + q\left(9\zeta_j^{(n+1)*} + 19\zeta_j^n - 5\zeta_j^{n-1} + \zeta_j^{n-2}\right), \tag{4.39}$$

where p and q have been previously defined. We now substitute (4.31) and (4.32) into (4.38) and (4.39) which yields

$$\zeta_j^{n+1} = r_1\zeta_j^n + r_2\zeta_j^{n-1} + r_3\zeta_j^{n-2} + 28p\overline{u}_j^n - 5p\overline{u}_j^{n-1} + p\overline{u}_j^{n-2}, \tag{4.40}$$

$$\overline{u}_j^{n+1} = r_1\overline{u}_j^n + r_2\overline{u}_j^n + r_3\overline{u}_j^n + 28q\zeta_j^n - 5q\zeta_j^{n-1} + q\zeta_j^{n-2}, \tag{4.41}$$

where

$$r_1 = 1 + 414pq, \qquad r_2 = -288pq, \qquad r_3 = 90pq. \tag{4.42}$$

Equations (4.40) and (4.41) are now combined into one matrix equation

$$\Phi^{n+1} = A\Phi^n, \tag{4.43}$$

where

$$\Phi^{n+1} = \left\{\zeta^{n+1}, \overline{u}^{n+1}, \zeta^n, \overline{u}^n, \zeta^{n-1}\overline{u}^{n-1}\right\}^T, \tag{4.44}$$

$$\Phi^n = \left\{\zeta^n, \overline{u}^n, \zeta^{n-1}, \overline{u}^{n-1}, \zeta^{n-2}, \overline{u}^{n-2}\right\}^T, \tag{4.45}$$

and

$$A = \begin{bmatrix} r_1 & 28p & r_2 & -5p & r_3 & p \\ 28q & r_1 & -5q & r_2 & q & r_3 \\ 1 & 0 & 0 & 0 & 0 & 0 \\ 0 & 1 & 0 & 0 & 0 & 0 \\ 0 & 0 & 1 & 0 & 0 & 0 \\ 0 & 0 & 0 & 1 & 0 & 0 \end{bmatrix} \tag{4.46}$$

is the amplification matrix. For any given values of p and q, A has six eigenvalues $(\lambda_k,\ k = 1, \cdots, 6)$. The condition for stability is that the magnitudes of all six

eigenvalues of A ($|\lambda_k|$) should be less than one. The eigenvalues are functions of the three parameters: the ratio of the water depth to the grid size $h/\Delta x$, the Courant number $C_r = \sqrt{gh}\Delta t/\Delta x$ and the dimensionless wave number $k\Delta x$. It is not very convenient to obtain analytical expressions for the eigenvalues. Therefore, the stability range is obtained numerically.

Figure 4.1 shows the variation of the magnitudes of the eigenvalues as a function of the Courant number and the wave number for $h/\Delta x = 1$. It is clear that only the first two eigenvalues, which are complex conjugates, leads to instabilities and that too only for certain values of the parameters C_r, $k\Delta x$ and $h/\Delta x$. Therefore, to assess the stability range at this point, we will concentrate on the first eigenvalue.

Figure 4.2(a) shows the variation of $|\lambda_1|$ at four different cross sections in figure 4.1(a). The value of $h/\Delta x$ is fixed at one and the four lines correspond to the values $k\Delta x/\pi = 1/5$, $2/5$, $1/2$ and $3/5$. The value of $|\lambda_1|$ reaches its maximum when $k\Delta x/\pi = 1/2$. Therefore, the region where $|\lambda_1|$ is less than one for $k\Delta x/\pi = 1/2$ is the range for which the scheme is stable. Figure 4.2(b) shows the value of $|\lambda_1|$ for $k\Delta x/\pi = 1/2$ and values of $h/\Delta x$ corresponding to 0.01, 0.1, 5, 10. For $C_r \leq 0.9$, the value of $|\lambda_1|$ is less than one. The stability range does not change much when $h/\Delta x$ is decreased from 0.1 to 0.01. So we can conclude that the scheme, when one predictor step and one corrector step is used, is stable for $C_r \leq 0.9$. This value is slightly different from the one obtained by Wei and Kirby (1998) where the stability range was $C_r \leq 0.8$.

Note, however, that this range is valid only for the linearized governing equations. Furthermore, the analysis above only accounts for the interior of the domain, where central difference schemes are used to compute the derivatives. At the boundaries, where one-sided schemes are also used, the stability criteria may be different. Thus, this analysis only provides a necessary condition for the stability of the numerical scheme. In actual applications, where the non-linear terms are included and the corrector scheme is used more than once, the scheme appears stable for $C_r \leq 0.6$.

4.1.3 Iteration scheme.

The linear stability analysis showed that the numerical solution technique is stable for the linearized governing equations provided that a Courant number less

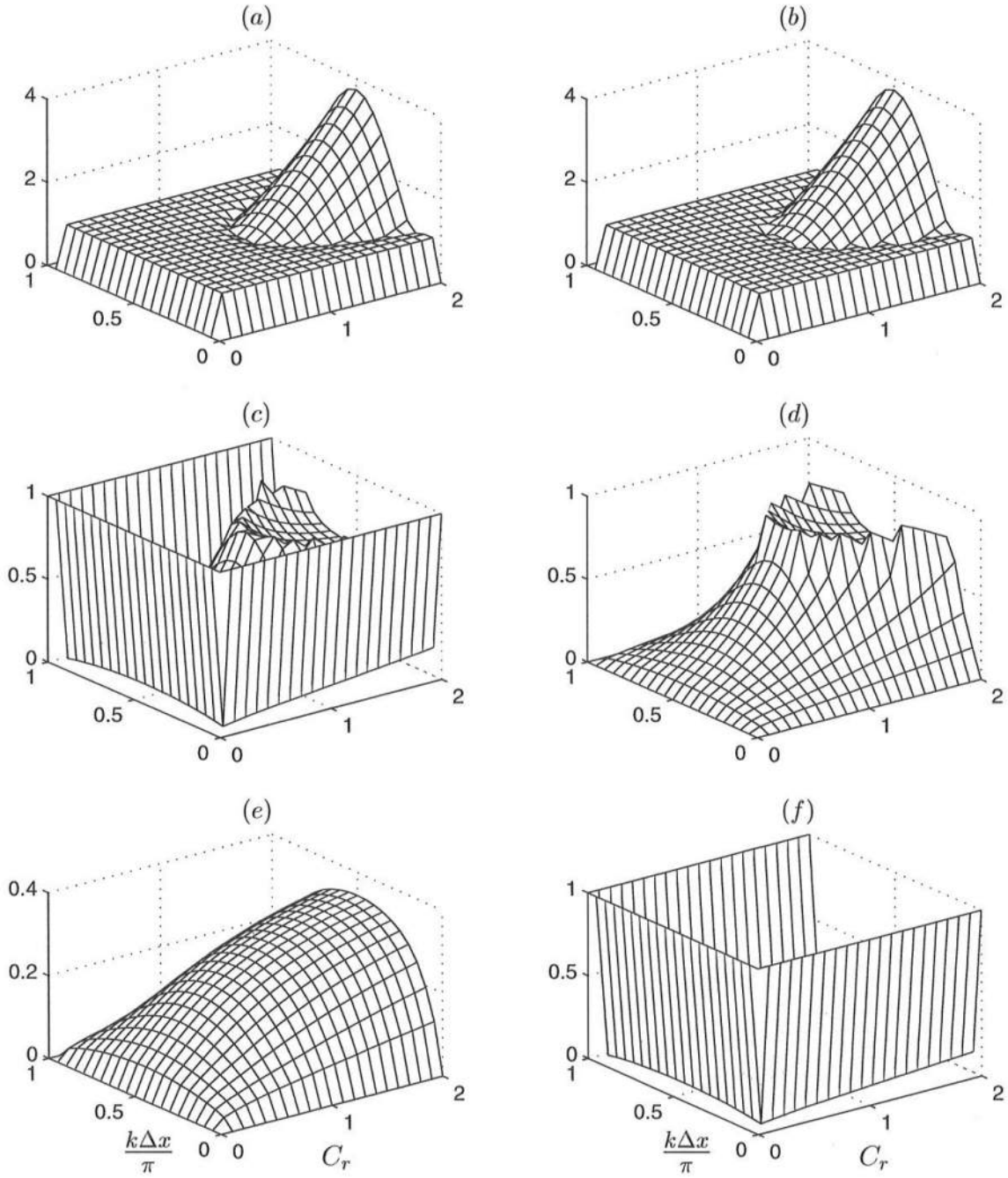

Figure 4.1: Magnitudes of the six eigenvalues λ_k, $k = 1, \cdots, 6$ as a function of the Courant number (C_r) and the dimensionless wave number ($k\Delta x$) for $h/\Delta x = 1$.

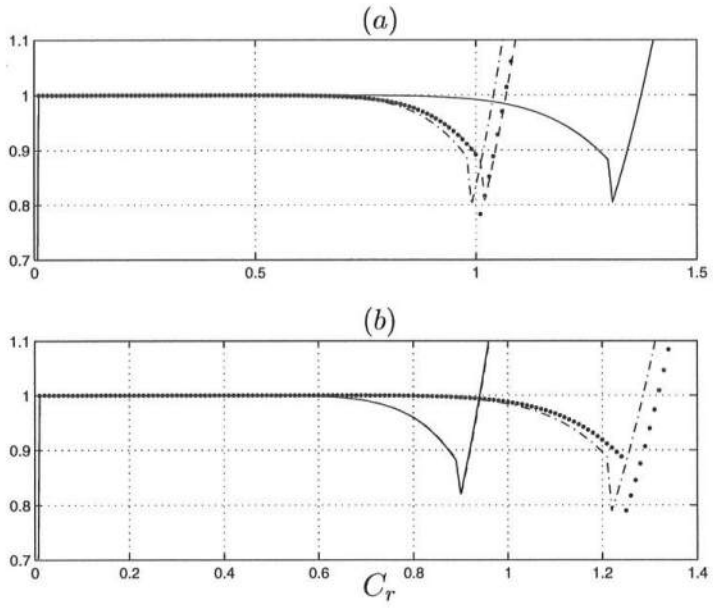

Figure 4.2: Magnitudes of the first eigenvalue λ_1 as a function of the Courant number (C_r): (a) $h/\Delta x = 1$, $k\Delta x/\pi = 1/5$ (———), $k\Delta x/\pi = 2/5$ (– – –), $k\Delta x/\pi = 1/2$ (–·–·–), $k\Delta x/\pi = 3/5$ (·····). (b) $k\Delta x/\pi = 1/2$, $h/\Delta x = 0.01$ (———), $h/\Delta x = 0.1$ (– – –), $h/\Delta x = 5$ (–·–·–), $h/\Delta x = 0.1$ (·····)

than 0.9 is used. The analysis assumed that for every predictive step, there is only one corrective step. In real applications using the non-linear equations, the range of stability is drastically reduced if the corrector step is used only once. Therefore, an iterative scheme is used so that the corrector step is repeated a number of times. To provide a bound on the number of times the step is iterated, an relative error estimate is defined as

$$e_r = \frac{\sum_{i=1}^{N} |w_i - w_i^*|}{\sum_{i=1}^{N} |w_i|}, \tag{4.47}$$

where N is the total number of grid points in space and w is the dependent variable and w^* denotes the previous calculated value using the corrector step. The error is calculated separately for the dependent variables ζ and $\overline{u}$. The scheme is iterated until the relative error is less than 10^{-4} for both of the dependent variables. In

the event that the denominator is zero, the absolute error is used to determine the number of iterations required.

Typically, for the weakly non-linear solutions, the error is less than the maximum specified after using just one corrector step. For the fully non-linear equations, the number of iterations is dependent on the Courant number. If a Courant number of 0.5 is used, generally the solutions converge after about three iterations.

4.1.4 Numerical filtering.

The non-linear terms in the equations cause generation of high frequency noise during the solution procedure. The noises are wave-like with a wave length of $2\Delta x$ where Δx is the spatial grid size. These high harmonic waves, if left unchecked, can grow very large and eventually destabilizes the computations. Various methods have been used to control the growth of these waves.

In this study, the numerical filtering technique of Shapiro (1970) is used. For a one dimensional model, Shapiro (1970) starts with a simple smoothing element

$$\overline{Z}_i = \frac{S}{2} Z_{i-1} + (1 - S) Z_i + \frac{S}{2} Z_{i+1}, \tag{4.48}$$

where the $\overline{Z}_i$'s are the smoothed values, the Z_i's are the raw values and S is the weight. The amplification factor for this filter is obtained by expressing the the raw values in terms of it Fourier components

$$Z_i = A \cos(k x_i + \phi) \tag{4.49}$$

and obtaining the amplitude of the smoothed function($\overline{A}$) from (4.48). The amplification factor is then

$$R(k) = \frac{\overline{A}}{A} = 1 - 2S \sin^2 \frac{k\Delta x}{2}. \tag{4.50}$$

It is easily seen that the choice of $S = 1/2$ gives $R = 0$ for waves of length $2\Delta x$. The amplification factor $(- - -)$ is shown in figure 4.3. Unfortunately, using this three-point scheme also damps some of the longer waves in the domain. Using (4.48) as the basis, higher order schemes can easily be constructed (see Shapiro (1970) for more details). In the computations shown, a five-point filter defined by

$$\overline{Z}_i = \frac{1}{16} \left(-[Z_{i+2} + Z_{i-2}] + 4[Z_{i+1} + Z_{i-1}] + 10 Z_i \right), \tag{4.51}$$

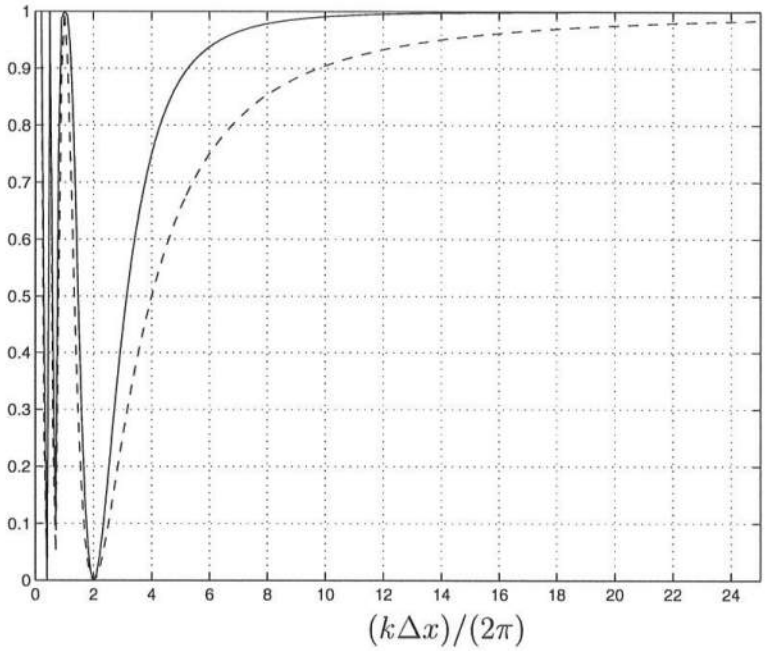

Figure 4.3: Amplification factors for a 3-point Shapiro filter (– – –) and a 5-point Shapiro filter (———).

which has the amplification factor

$$R_2(k) = \frac{\overline{A}}{A} = 1 - \sin^4 \frac{k\Delta x}{2} \tag{4.52}$$

is used (———, figure 4.3). This filter is applied twice every wave period for both ζ and $\overline{u}$ which is enough to check the growth of the spurious high frequency waves.

4.2 Boundary conditions.

Boundary conditions are necessary for any numerical model. Regardless of the validity of the model, use of inappropriate boundary conditions will yield incorrect results from the model. In this model, waves are input at the left boundary and absorbed at the right boundary. In addition, the inclusion of wave breaking in the model implies that there is a third boundary where the vorticity is generated. In our case, this boundary is the lower edge of the roller, which is prescribed separately for the breaking waves. The parameters for this boundary are obtained from the

hydraulic jump measurements detailed in the previous chapter. In this section, all three boundary conditions are discussed.

4.2.1 The absorbing-generating boundary.

For practical applications, any wave propagation model will have to account for waves traveling in either direction. This could be the result of waves reflecting from a sloping bottom, higher harmonics generated due to wave breaking or waves reflecting off a wall. Specifying only the incident waves at the generating boundary invariably results in the wave field becoming rapidly distorted, frequently with catastrophic results. There are a number of ways to solve this problem.

Wei *et al.* (1995) and Yu (1996) used a simple absorbing-generating boundary condition to take out the outgoing waves. This mechanism was based on linear theory and was found not very effective. Larsen and Dancy (1983) proposed a method based on mass conservation to add and subtract mass at a given point in the 2-dimensional domain. Wei *et al.* (1999) extended this method for Boussinesq-type equations using a spatially distributed source function inside the domain. The waves propagate in either direction and sponge layers at both ends of the domain is used to absorb the waves.

Hibberd and Peregrine (1979) used the method of characteristics to derive a boundary condition for the non-linear shallow water equation. Here the incoming Riemann variable was specified and the outgoing wave is calculated. For simultaneous absorption and generation of waves at the boundary, the incoming variable is not known apriori. Kobayashi *et al.* (1987) solved this problem by using the outgoing characteristic and substituting a linear long wave relation between the velocity and surface elevation to calculate the outgoing wave. Van Dongeren and Svendsen (1997) extended this method to equations of continuity and momentum locally dominated by the terms corresponding to the non-linear shallow water equations. The performance of this absorbing-generating boundary condition was shown superior to the classical Sommerfeld radiation condition.

For our case, which is a one-dimensional model, we extend the absorbing-generating boundary condition of Van Dongeren and Svendsen (1997) to the Boussinesq model. The criteria that the continuity and momentum equations is locally

dominated by the linear and non-linear terms is satisfied since $O(\mu^2) \ll 1$. The equations for a horizontal bottom with no wave breaking, which is a subset of (2.53) and (2.72), can be written as

$$\frac{\partial \zeta}{\partial t} + \frac{\partial}{\partial x}\left[\overline{u}(h+\zeta)\right] = 0, \tag{4.53}$$

$$\frac{\partial \overline{u}}{\partial t} + g\frac{\partial \zeta}{\partial x} + \overline{u}\frac{\partial \overline{u}}{\partial x} = \mathcal{G}, \tag{4.54}$$

where $\mathcal{G}$ represents the $O(\mu^2)$ terms, including the non-linear terms for the fully non-linear model. If we define $d = h + \zeta$, (4.53) and (4.54) can be expressed in matrix form as

$$\frac{\partial \boldsymbol{f}}{\partial t} + \boldsymbol{A}\frac{\partial \boldsymbol{f}}{\partial x} = \boldsymbol{G}, \tag{4.55}$$

where

$$\boldsymbol{f} = \begin{bmatrix} d \\ \overline{u} \end{bmatrix}, \quad \boldsymbol{A} = \begin{bmatrix} \overline{u} & d \\ g & \overline{u} \end{bmatrix} \quad \text{and} \quad \boldsymbol{G} = \begin{bmatrix} 0 \\ \mathcal{G} \end{bmatrix} \tag{4.56}$$

We write the equations in characteristic form by realizing that the eigenvalues of $\boldsymbol{A}$ are $\overline{u} \pm \sqrt{gd}$ which are always real. Therefore, a modal matrix $\boldsymbol{P}$ can be constructed from the eigenvectors such that $\boldsymbol{P}^{-1}\boldsymbol{A}\boldsymbol{P}$ is diagonal, which gives

$$\boldsymbol{P} = \begin{bmatrix} \sqrt{d/g} & -\sqrt{d/g} \\ 1 & 1 \end{bmatrix} \quad \text{and} \quad \boldsymbol{P}^{-1} = \frac{1}{2}\begin{bmatrix} \sqrt{g/d} & 1 \\ -\sqrt{g/d} & 1 \end{bmatrix}. \tag{4.57}$$

Equation (4.55), can then be re-expressed as

$$\boldsymbol{P}^{-1}\frac{\partial \boldsymbol{f}}{\partial t} + \boldsymbol{P}^{-1}\boldsymbol{A}\boldsymbol{P}\boldsymbol{P}^{-1}\frac{\partial \boldsymbol{f}}{\partial x} = \boldsymbol{P}^{-1}\boldsymbol{G}, \tag{4.58}$$

which yields a set of two equations in terms of $\overline{u}$ and ζ,

$$\frac{\partial \beta^+}{\partial t} + \left(\overline{u} + \sqrt{gd}\right)\frac{\partial \beta^+}{\partial x} = \mathcal{G}, \tag{4.59}$$

$$\frac{\partial \beta^-}{\partial t} + \left(\overline{u} - \sqrt{gd}\right)\frac{\partial \beta^-}{\partial x} = \mathcal{G}. \tag{4.60}$$

Here $\beta^+ = \overline{u} + 2\sqrt{gh}$ is the incoming characteristic and $\beta^- = \overline{u} - 2\sqrt{gh}$ is the outgoing characteristic. The information about the waves that are propagating

away from the shoreline is given by β^-. We now have to assume something about the interaction between the incoming waves, which are specified and the outgoing waves which are unknown. Following Van Dongeren and Svendsen (1997) we utilize that the linear terms in the equations are $O(1)$ and the $O(\delta, \mu^2)$ terms are considered small. We can divide both the volume flux and the surface elevation into incoming and outgoing components

$$\overline{u} = \overline{u}_i + \overline{u}_r \quad \text{and} \quad \zeta = \zeta_i + \zeta_r, \tag{4.61}$$

where the subscript i denotes quantities coming into the domain and the subscript r represents the outgoing components. Now, the expression for β^- is, keeping terms up to $O(\delta^2)$

$$\begin{aligned}\beta^- &= \overline{u}_i + \overline{u}_r - 2\sqrt{gh\left(1 + \frac{\zeta_i + \zeta_r}{h}\right)} \\ &= \overline{u}_i + \overline{u}_r - 2\sqrt{gh}\left(1 + \frac{\zeta_i + \zeta_r}{2h} - \frac{(\zeta_i + \zeta_r)^2}{8h}\right) + O\left(\delta^2\right).\end{aligned} \tag{4.62}$$

We now express the water surface elevations (ζ_i and ζ_r) in terms of the velocities ($\overline{u}_i$ and $\overline{u}_r$) utilizing the relation

$$\overline{u}_i = \frac{c\zeta_i}{h + \zeta_i}, \qquad \overline{u}_r = -\frac{c\zeta_r}{h + \zeta_r}, \qquad c = \sqrt{g(h + \zeta_i + \zeta_r)}. \tag{4.63}$$

After some algebraic manipulations, the water surface elevations ζ_i and ζ_r can be expressed in terms of the velocities as

$$\frac{\zeta_i}{h} = \frac{\overline{u}_i}{c_0} + \frac{1}{2}\frac{\overline{u}_i^2}{c_0^2} + \frac{\overline{u}_i\overline{u}_r}{2c_0^2} + O\left(\frac{\zeta_i^3}{h^3}\right), \tag{4.64}$$

$$\frac{\zeta_r}{h} = -\frac{\overline{u}_r}{c_0} + \frac{1}{2}\frac{\overline{u}_r^2}{c_0^2} + \frac{\overline{u}_i\overline{u}_r}{2c_0^2} + O\left(\frac{\zeta_r^3}{h^3}\right), \tag{4.65}$$

where $c_0 = \sqrt{gh}$ and both ζ_i/h, $\zeta_r/h \simeq O(\delta)$. Substituting (4.64) and (4.65) into (4.62) gives

$$\frac{\beta^-}{c_0} = -2 - \frac{1}{4}\frac{\overline{u}_i^2}{c_0^2} - \frac{3}{2}\frac{\overline{u}_i\overline{u}_r}{c_0^2} + 2\frac{\overline{u}_r}{c_0} - \frac{1}{4}\frac{\overline{u}_r^2}{c_0^2}. \tag{4.66}$$

Solving this equation with respect to $\overline{u}_r$, the outgoing component is calculated as

$$\frac{\overline{u}_r}{c_0} = \left(-3\frac{\overline{u}_i}{c_0} + 4\right) \pm 2\sqrt{2\frac{\overline{u}_i^2}{c_0^2} - 6\frac{\overline{u}_i}{c_0} + 4 - \left(\frac{\beta^-}{c_0} + 2\right)}. \tag{4.67}$$

The still water condition is

$$\overline{u}_r = 0, \qquad \overline{u}_i = 0 \qquad \text{and} \qquad \frac{\beta^-}{c_0} + 2 = 0, \tag{4.68}$$

which gives the positive root as the spurious root, which leaves

$$\frac{\overline{u}_r}{c_0} = \left(-3\frac{\overline{u}_i}{c_0} + 4\right) - 2\sqrt{2\frac{\overline{u}_i^2}{c_0^2} - 6\frac{\overline{u}_i}{c_0} - \left(\frac{\beta^-}{c_0} - 2\right)}. \tag{4.69}$$

The value of β^- at the boundary is calculated from (4.57) using the ABM scheme at each time step. During the solution of the Boussinesq equations the values of $\overline{u}$ and ζ are calculated at the next time step at all interior points of the computational domain. At the boundary, the incoming wave ($\overline{u}_i$) is specified. The expression (4.69) then gives the value of $\overline{u}_r$, and hence $\overline{u}$ at the boundary. The continuity equation gives the value of ζ at the boundary.

Van Dongeren and Svendsen (1997) tested this boundary condition for very long waves. For the present model, short waves are used as input to the model for all practical applications. Figure 4.4 shows the performance of the boundary condition for two wave conditions. For both cases, the initial condition is no waves in the domain ($\zeta = 0$ everywhere in the domain). Waves are generated at the boundary during $t = 0 - 6T$. The waves are tapered with a hyperbolic tangent function to suppress transients during the first and last period. The waves propagate up to a wall where they are reflected. The reflect waves then pass through the absorbing-generating boundary at $x = 0$. The length of the wave tank (λ) was 5.0 m for the first case and 20 m for the second.

Figure 4.4(a) shows the time series at the absorbing-generating boundary at $x = 0$ for a long wave of $T\sqrt{g/h} = 26$ and $L/\lambda \simeq 2$, where L is the wave length. The waves reflected from the wall boundary reaches the absorbing-generating boundary while waves are still being generated and sent into the domain. As a result, standing waves are present in the domain for most of time the waves are in domain. Due

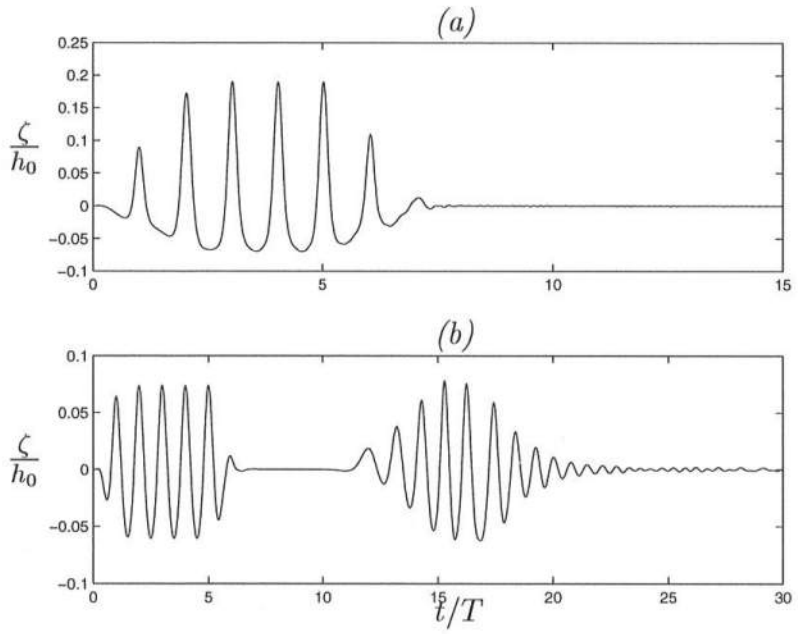

Figure 4.4: Time series of the water surface elevation at the boundary ($x = 0$) for the fully non-linear model, showing the effect of the absorbing generating boundary condition. (a) long waves ($T\sqrt{g/h} = 26$) (b) short waves ($T\sqrt{g/h} = 10.5$).

to the dispersive nature of the equations, there is a tail of very short waves for the reflected waves. These small waves propagate slowly out of the domain. It is seen that still water condition is recovered quickly.

Figure 4.4(b) shows the time series at the boundary ($x = 0$) for a much shorter wave of $T\sqrt{g/h} = 10.5$ and with $L/\lambda \simeq 0.2$. After about ten wave periods, the reflected waves reach the absorbing-generating boundary. Again, the dispersive nature of the model transforms the wave packet and at the boundary, the reflected waves are groupy in nature. The recovery of still water conditions takes a longer time in this case, probably also as a result of the length of the domain in comparison to the wave length. Overall, the performance of this boundary condition is very good for regular waves. The performance of this boundary for random waves has not yet been tested.

4.2.2 Wave absorption at the shore.

Instead of modeling a moving shoreline, the present version of the model uses a shelf of finite but very small water depth close to the shoreline. When the breaking waves reach the shelf, the wave heights are small. Even so, a wall boundary at the end of the domain will reflect these waves back into the domain causing disturbances in the wave field. These reflected waves are eliminated by a sponge layer close to the boundary which takes out the energy from these waves (Israeli and Orszag 1981).

For a sponge layer which extends from $x = x_s$ to $x = x_l$, the corresponding dissipation term in the model is defined as

$$F_{sp} = W(x)\overline{u}, \tag{4.70}$$

where

$$W(x) = \begin{cases} 0, & x < x_s \\ \alpha_1 f(x). & x > x_s \end{cases} \tag{4.71}$$

The value of $W(x)$ is set to zero outside the sponge layer. To avoid possible reflections from the sponge layer, the value of $W(x)$ is increased gradually from the starting location of the sponge layer ($x = x_s$) to the end of the sponge layer ($x = x_l$). Therefore, in (4.71), the value of $f(x)$ increases gradually from zero to one. The coefficient α_1 determines the strength of the sponge layer. The function $f(x)$ is given by

$$f(x) = \frac{\exp\left[(x_{sp})^n\right] - 1}{\exp(1) - 1}, \qquad x_{sp} = \frac{x - x_s}{x_l - x_s}. \tag{4.72}$$

The value of n in $f(x)$ has to be larger than one to ensure a smooth transition into the sponge layer. In the computations given later, the value used is $n = 2$. The value of α_1 needs to be monitored to prevent wave reflections. In general, the value used in the model ranged from $\alpha_1 = 5$ to $\alpha_1 = 10$. The shelf depth (h_s) used in the model is 0.01 m and the length of the sponge layer $(x_l - x_s)/h_s \simeq 200$.

4.2.3 Boundary conditions for wave breaking.

Once the wave starts breaking, a recirculating region is formed at the front face of the wave. This region, commonly called the "roller", moves with the wave.

The physical process was identified and explained in the previous chapter where the measurements from hydraulic jumps were also presented. In this section, we discuss how these measurements can be applied to waves.

One of the difficulties lie in the fact that in reality, the flow inside the roller as well as the size and shape of the roller keeps changing as the wave propagates towards the shore. At present, not much is known about this process. The analysis of the roller development is still an ongoing study (see, e.g., Brocchini and Peregrine 1998) and is beyond the scope of the present work. Here, the vorticity generated in the roller region is approximated by specifying the vorticity at the mean lower edge of the roller.

In the present model, we use the equivalence established between breaking waves and hydraulic jumps. As mentioned in Chapter 3, breaking waves viewed in a coordinate system moving with the waves have flow patterns similar to that in hydraulic jumps. The turbulent stresses, the surface profile and the vorticity are invariants under such a transformation. Therefore, the thickness of the roller and the magnitude of the vorticity are obtained from the measurements in the hydraulic jump analyzed in Chapter 3. These quantities are approximated by using a curve fit through the data points (figure 4.5).

The non-dimensional roller thickness can be represented by the curve

$$\zeta_e = 0.78 e^{x/\ell_r} \left(\frac{x}{\ell_r} - \frac{x^2}{\ell_r^2} \right) \tag{4.73}$$

and the non-dimensional vorticity values is well represented by the linear fit

$$\omega_s = 15.75 \left(1 - \frac{x}{\ell_r} \right).$$

It turns out that the numerical computations are eased somewhat if this is replaced by the expression

$$\omega_s = 15.75 \left(1 - e^{40x/\ell_r} \right) \left(1 - \frac{x}{\ell_r} \right), \tag{4.74}$$

which is shown as the solid line in figure 4.5b. This avoids the sharp discontinuity at $x/\ell_r = 0$. The expressions of ζ_e and ω_s from (4.73) and (4.74) are used in the solution to the vorticity equation.

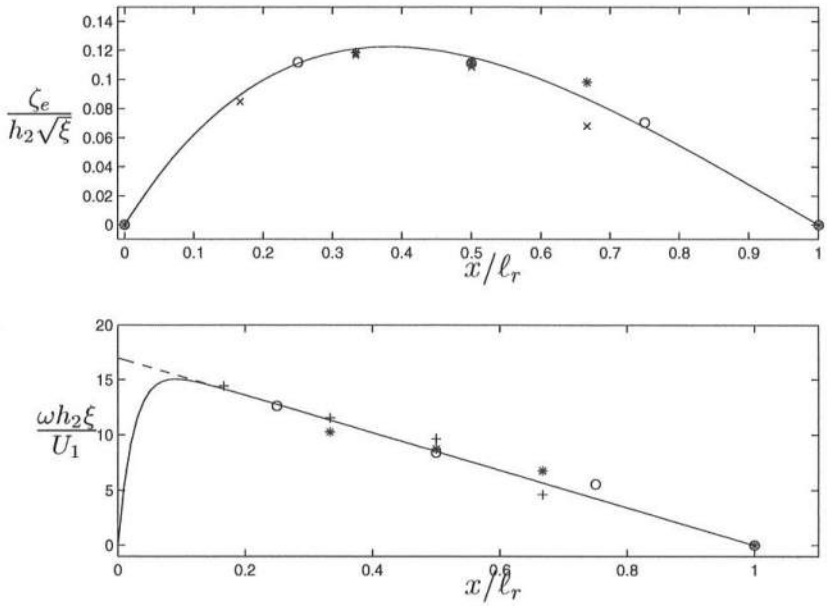

Figure 4.5: (a) The non-dimensional thickness of the roller for the hydraulic jumps: Data for Froude numbers 1.38(∘), 1.46(×), 1.56(∗) and least-squares fit (———). (b) Non-dimensional vorticity at the lower edge of the roller with least squares linear fit (– – –) and according to (4.74)(———).

Note that the non-dimensionalization of the roller thickness involves the depth ratio $\xi = h_2/h_1$ where h_2 is the depth far downstream of the jump and h_1 is the minimum depth in front of the jump. The non-dimensionalization for the vorticity also involves the velocity U_1 at the minimum depth h_1. The equivalence between these quantities in the hydraulic jump and that in a wave has to be determined.

The maximum depth h_2 can easily be approximated to the total depth at the crest of the wave h_c and the minimum depth h_1 is associated with the depth at the wave trough h_t. The equivalent velocity is approximated as follows: The speed of a bore is given by

$$c_b^2 = \frac{1}{2} g h_1 \xi \left(\xi + 1\right). \tag{4.75}$$

The bore moves into quiescent water, whereas the breaking wave has an opposing velocity of the wave trough in front of it. This opposing velocity u_t, if the wave has

constant form and there is no net mass flux, is

$$u_t = c_w \frac{\zeta_t}{h + \zeta_t}, \tag{4.76}$$

where c_w is the wave speed, h is the still water depth and ζ_t is the trough elevation (which is negative). Then, we have

$$c_w - u_t = c_b. \tag{4.77}$$

If we substitute the expressions for c_b and u_t from (4.75) and (4.76) into (4.77) and use the equivalence for the depths mentioned, we get

$$c_w^2 = \frac{1}{2} g h_t \left(\frac{h_t}{h} \right)^2 \xi \left(\xi + 1 \right), \tag{4.78}$$

where $\xi = h_c / h_t$ and $h_t = h + \zeta_t$. In the wave model, these relations are used to get the dimensional values of the vorticity and the roller thickness.

4.2.4 Initiation of breaking and development of the roller.

The Boussinesq equations will not directly lead to wave breaking in shallow water due to the inclusion of the dispersive terms in the equations. The frequency dispersion will tend to balance the amplitude dispersion, thus stabilizing the wave profile. Hence, any modeling of surf zone waves using Boussinesq-type equations necessitates explicit specification of the location where the waves start breaking.

During the initial stages of breaking, the waves undergo a rapid transformation from organized motion to turbulent motion. One of the important phenomena that occur during this stage, in addition to a rapid decrease in wave height, is the development of a roller at the front face of the wave. After some time, these breaking waves reach a quasi-steady state, forming a propagating bore.

The development of the roller in breaking waves is a complicated process. A mathematical formulation for this process has not been developed yet. A relatively simple method, based on geometrical considerations, was given by Deigaard (1989) for determining the point of initiation of wave breaking and the length of the roller. Schäffer *et al.* (1993) adapted this method for waves in the surf zone based on the following considerations: As the waves approach the shoreline, the local steepness at

the front face of the waves become large leading to instabilities and the wave breaks. The critical slope at the toe of the roller $\tan\alpha$ (see figure 4.6) found by Deigaard (1989) in the inner surf zone was $\alpha = 10°$. Schäffer *et al.* (1993) contended that at the point of initiation of breaking, this slope can be much larger. Thus, an exponential variation

$$\tan\alpha = \tan\alpha_0 + (\tan\alpha_b - \tan\alpha_0)\exp\left[-\ln 2\left(\frac{t-t_b}{T_{st}}\right)\right], \tag{4.79}$$

where $\alpha_0 = 10°$ is the value of the slope at the toe of the roller in the inner surf zone found by Deigaard (1989), $\alpha_0 = \alpha_b$ is the angle at which wave breaking is initiated, T_{st} is the time during which the roller develops, t_b is the time at which the breaking start. Thus, the development of the roller follows an exponential curve. The end of the roller was determined by using a linear extrapolation from the toe of the roller to the surface of the wave as shown in figure 4.6(a). The shape of the roller (figure 4.6(a), – – –) was then determined by multiplying the thickness $e(x)$ by a shape factor. This method has been used with good success by Madsen *et al.* (1997) and Yu (1996). A similar method is used in the model of Kennedy *et al.* (1999), which is an extension of the Wei *et al.* (1995) model

For the present model, the location of the toe of the roller and the development of the roller is determined using the same method. However, the roller is assumed to end at the crest of the wave (figure 4.6(b)). The reason is that in the present model, the breaking terms are calculated from the vorticity distribution. There is residual vorticity even after the roller has passed by. This is not the case for Schäffer *et al.* (1993), where the breaking term is active only in the region where the roller exists. The start of wave breaking is defined as the location where the front face of the wave exceeds a particular angle α_b. The roller slowly develops during a specified period T_{st} which essentially models the transition region. The wave transforms into a fully developed bore during this time frame. For most natural beaches where there are no longshore bars, the wave does not stop breaking until the shoreline is reached. Where the wave breaks on a bar, the breaking may stop when the wave propagates into the deeper water behind the bar. This is modeled by stopping the breaking when the maximum angle at the front face of the wave is less than α_0.

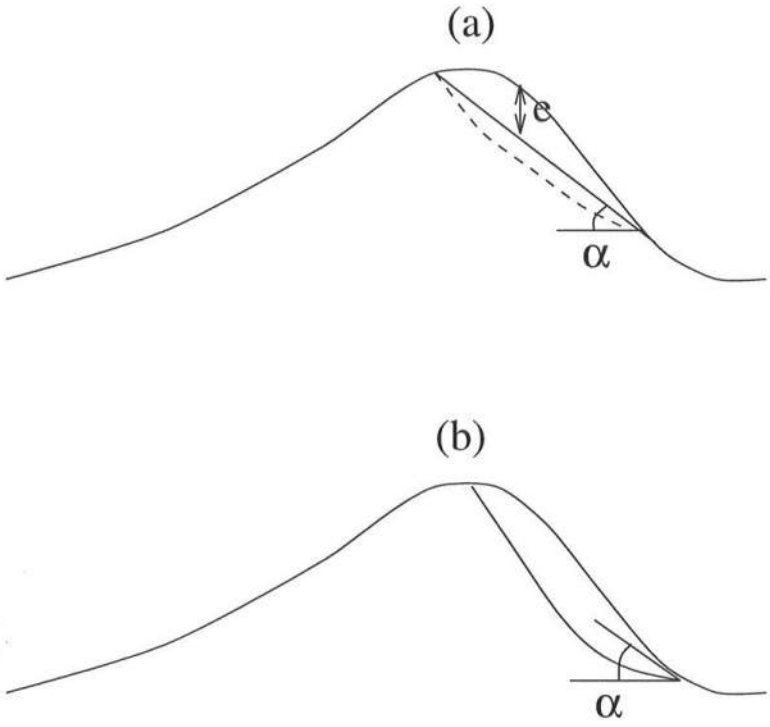

Figure 4.6: Determination of the position of surface roller.

For the weakly non-linear model, the inception point for wave breaking is when $\alpha_b \geq 20°$. Recent experiments by Duncan *et al.* (1999) show that the time scale for the development of the roller is about $T_{st} = 0.25T$ where T is the wave period. The model results shown use the value $T_{st} = 0.2T$. The value of α_0 was found not to have much influence on the wave breaking on a gentle slope and the value used was $\alpha_0 = 10°$. All values were calibrated by comparing the wave height results to one data set. For subsequent comparisons, these values were left unchanged.

For the fully non-linear model, the starting point for wave breaking used is $\alpha_b \geq 32°$, which is an increase from the value used in the weakly non-linear model. The reason for this increase is that the wave shape predicted by the fully non-linear model is steeper than the weakly non-linear formulation. Hence, using the same criteria for the fully non-linear model causes the waves to break very early. The other two parameters (α_0 and T_{st}) retain the same value.

Chapter 5

COMPARISON OF MODEL RESULTS WITH DATA.

To demonstrate the performance of the model described in the previous chapters, tests have been conducted for monochromatic wave conditions with different wave heights and periods ranging from long waves to waves in the intermediate water depth. First, the model is tested for the case of solitary wave propagation on a horizontal bottom as well as on plane beaches. These tests are compared to the previously available results from the fully non-linear Boussinesq model of Wei *et al.* (1995) and Kennedy *et al.* (1999), and the full potential flow model (Wei *et al.* 1995).

Next, the vorticity distribution in breaking waves, the shape of the roller and the magnitudes of the different terms that represent breaking are discussed. Then, the present Boussinesq-type models are compared to wave height and set-up data of Hansen and Svendsen (1979) for waves shoaling and breaking on a gentle slope. A spectral solution to the weakly non-linear equations is used as input to the model for all studies of breaking waves. The differences between the weakly non-linear and the fully non-linear model are shown along with available results from Kennedy *et al.* (1999) model.

The model results are then compared to the surface profile and velocity measurements of Cox *et al.* (1995). Again, the weakly and the fully non-linear models are compared to the data. The results from the model can then be used to calculate the undertow profiles. Two sets of comparisons are shown: one with the data of Cox *et al.* (1995) and another with the results of Ting and Kirby (1994). The difference between using the present model and a potential flow model is also illustrated.

The availability of the velocity profiles from the model also makes it possible to calculate other wave-averaged quantities such as the wave mass flux, the cross-shore wave radiation stress. These quantities cannot be measured directly. The estimates of these quantities are presented. The phase speed of the waves in the breaking region is also discussed in this context.

5.1 Solitary wave propagation and shoaling.

First, we look at propagation of solitary waves over a horizontal bottom. This test indicates the stability and conservative properties of the numerical scheme.

Analytical closed form solutions of solitary waves have been derived for some approximate equations such as the KdV equations and Serre equations. Very accurate solutions can be obtained by solving the full potential problem using Boundary Element methods (Grilli *et al.* 1994). It is possible to obtain spectral solutions (as shown in appendix C for monochromatic waves) for solitary waves. However, solitary waves are infinitely long and a large number of terms would have to be retained for the spectral solutions to be reasonably accurate.

Approximate solutions have been derived for the weakly non-linear $\zeta - u_\alpha$ equations by Wei *et al.* (1995). Even using these solutions as the input condition for the numerical model, Wei *et al.* (1995) found that the wave heights and wave shape changed constantly during the initial stages of the computation. This change in solitary wave profile even on a horizontal bottom is due to the approximate nature of the solution even for the weakly non-linear equations (whereas they use a fully non-linear model). Also, differences between the solution to the numerical equations and the solution to the actual equations cause the solitary wave to change shape. Small oscillatory tails with a smaller phase speed than the primary wave were found to develop and lag behind. The primary wave stabilized after some time, i.e., the wave shape remained constant, indicating that the permanent form solution to the numerical equations had been attained. Once the form of the waves stabilized, it propagated without change of shape over very long distances. The height of this wave, however, was different from that of the approximate solution input at the boundary. Therefore, a trial-and-error method was used wherein the height of the solitary wave input to the model was adjusted until a stable solitary wave with the

desired wave height was obtained. The shape and height of these solutions were then compared to the solution obtained by Tanaka (1986) to show the accuracy of the model.

It is also possible to obtain the permanent form solution to the numerical equations using the solution to the KdV equation by the same process of trial and error. The solution to KdV equations are simpler, and hence is the method of choice here. The solitary wave solution to the KdV equation (see, e.g., Dean and Dalrymple 1991) is

$$\zeta(x,t) = a\,\mathrm{sech}^2\left\{\frac{\sqrt{3}}{2}\sqrt{\left(\frac{a}{h^3}\right)}\,(x - Ct - x_0)\right\}, \tag{5.1a}$$

with

$$C = \sqrt{gh}\left(1 + \frac{a}{2h}\right), \tag{5.1b}$$

where a is the amplitude of the wave. The stable form of the solitary wave corresponding to the fully non-linear $\zeta - \overline{u}$ model is obtained similar to the procedure used by Wei *et al.* (1995).

Figure 5.1 shows the comparison between this stable solitary wave form obtained for the present version ($\zeta - \overline{u}$) of the fully non-linear model described in the earlier chapters and the closed form solution of Tanaka (1986) for three different values of non-linearity ($\delta = a/h_0$= 0.2, 0.3 and 0.4). The solitary wave forms given by the present model closely match Tanaka's solutions. For the case of $\delta = 0.4$, the result from Wei *et al.* (1995) is also shown. Using the $\zeta - \overline{u}$ version of the Boussinesq equations (present model) gives a slightly wider profile for the water surface elevations compared to Tanaka's solution whereas using the $\zeta - u_\alpha$ version (Wei *et al.* (1995) model) gives a slightly narrower profile for waves with higher non-linearity. This shows that the fully non-linear $\zeta - \overline{u}$ model can predict the form of the solitary waves propagating on a horizontal bottom with an accuracy comparable to the that of the Wei *et al.* (1995) model.

We now look at the case of solitary wave shoaling. Near the breaking region, solitary waves generally attain a larger wave height to water depth ratio than in the case of monochromatic wave trains. Thus, this test demonstrates the performance

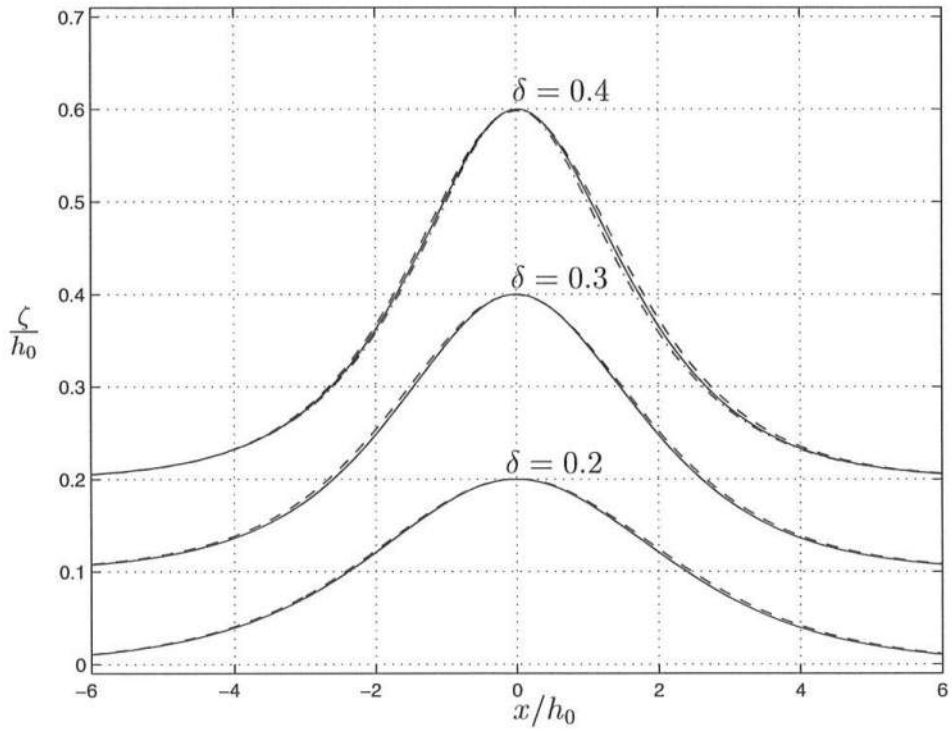

Figure 5.1: Comparison of solitary wave shapes for $\delta = 0.2$, $\delta = 0.3$ and $\delta = 0.4$ of the present model (– – –) with results from Tanaka (1986) (———) and Wei *et al.* (1995) (–·–·–).

of the model in the region of high non-linearity. Furthermore, this test gives an indication of the speed of propagation of waves predicted by the model, in the absence of extra influences like, for example, wave reflection.

Figure 5.2 shows the computational domain for this case. Permanent form solitary wave solutions are obtained, as mentioned before, by propagating an approximate solution over long distances. These stable solitary wave solutions are used as the input at the offshore boundary where the constant depth is h_0. The waves are propagated on to a beach slope of 1:m. The coordinate is set such that the toe of the slope is $x = 0$ and $t = 0$ when the wave crest reaches the toe. The depth at the shelf close to the shoreline is $h_1 = 2\ cm$ for these computations.

Four different cases are presented here with different wave conditions on different beach slopes corresponding to the results shown in Wei *et al.* (1995).

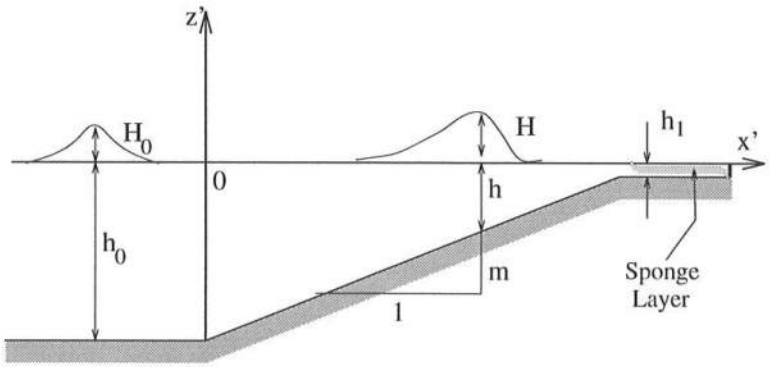

Figure 5.2: Schematic computational domain used for solitary wave shoaling comparisons.

The fully non-linear potential flow (FNPF) model solves the exact boundary value problem for irrotational wave motion in incompressible, inviscid fluid given by

$$\phi_{xx} + \phi_{zz} = 0 \qquad -h < z < \zeta, \tag{5.2}$$

$$\phi_z + h_x \phi_x = 0 \qquad z = -h, \tag{5.3}$$

$$g\zeta + \phi_t + \frac{1}{2}[(\phi_x)^2 + (\phi_z)^2] = 0 \qquad z = \zeta, \tag{5.4}$$

$$\zeta_t + \zeta_x \phi_x - \phi_z = 0 \qquad z = \zeta, \tag{5.5}$$

using Boundary Element methods. Grilli *et al.* (1994) showed that the the FNPF model gives very accurate results for the case of solitary wave shoaling. Very close to the breaking region, the error between the FNPF model and experimental data was about 1%. Therefore, in this section, the results from the FNPF model are used as the reference. To compare the present model to the Wei *et al.* (1995) model and the FNPF model, the input wave has to match as closely as possible. For the FNPF model, the exact solution, using the method of Tanaka (1986), was used as input, whereas for the present model as well as for the model of Wei *et al.* (1995), the numerically stable solutions were used as the input. The results from the $\zeta - \overline{u}$ model are compared to FNPF model and the Wei *et al.* (1995) model.

The comparisons between the three models are shown in figure 5.3. The four sub-plots (a)-(d) correspond to four different slopes of 1:100, 1:35, 1:15 and 1:8

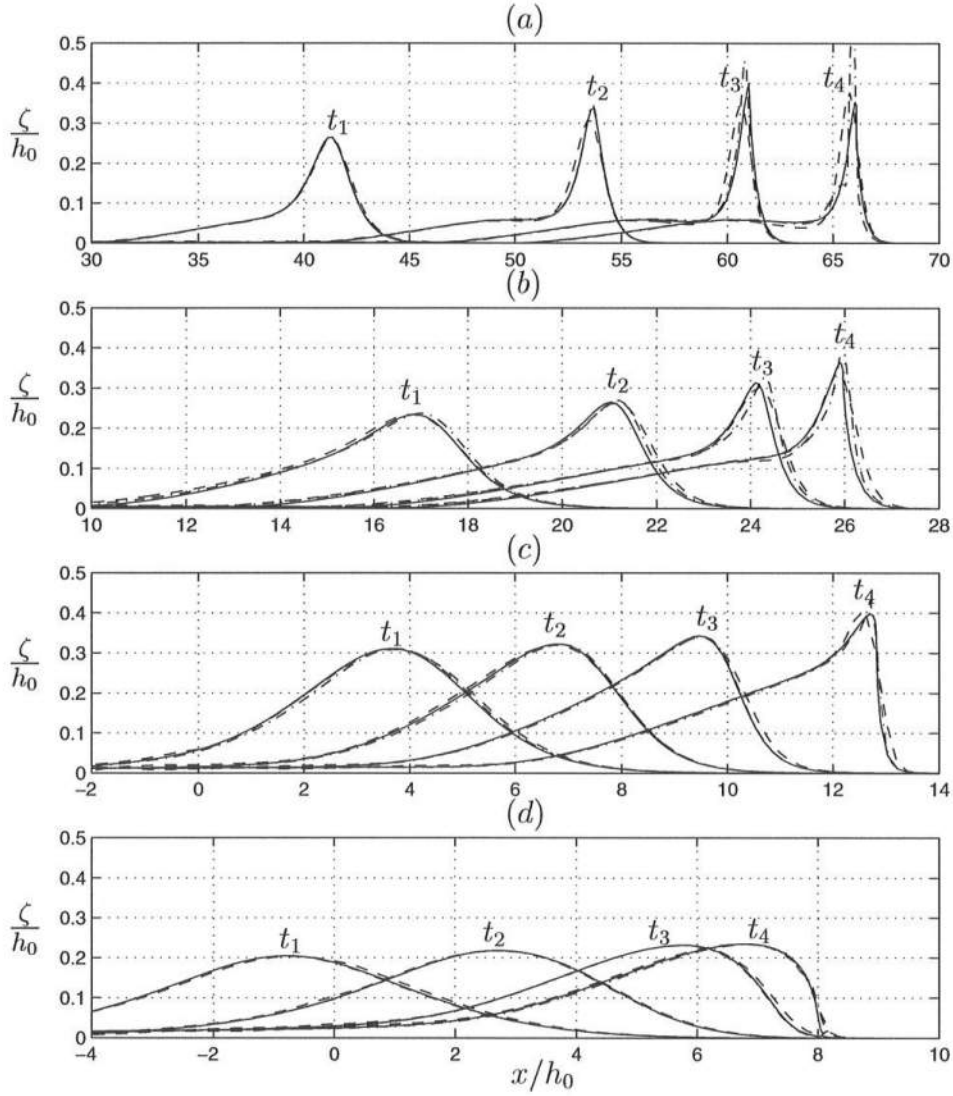

Figure 5.3: Comparison of surface elevations for solitary waves shoaling on plane beaches at four different times after the start of the computation. FNPF (———), the Wei *et al.* (1995) model (–·–·–) and the present model (– – –).
(a) s=1:100, δ=0.2, t_1 = 39.982, t_2 = 53.191, t_3 = 61.131 and t_4 = 66.890.
(b) s=1:35, δ=0.2, t_1 = 16.243, t_2 = 20.64, t_3 = 24.032 and t_4 = 25.936.
(c) s=1:15, δ=0.3, t_1 = 3.23, t_2 = 6, t_3 = 8.401 and t_4 = 11.32.
(d) s=1:8, δ=0.2, t_1 = -0.739, t_2 = 2.575, t_3 = 5.576and t_4 = 6.833.
The last profile in (a)-(c) corresponds to the theoretical breaking point.

respectively. These slopes range from a very gentle beach to a very steep beach. The value of δ at the constant depth section is 0.2 for (a), (b) and (d) and is 0.3 for (c). Four different spatial profiles corresponding to different times (scaled as $t\sqrt{g/h_0}$) are shown in each of the sub-plots. The profiles, obtained from each of the model at the same time after the crest of the wave has reached the toe of the slope, are compared to each other. The last profile (corresponding to t_4) is the theoretical breaking point defined here as the location where the wave front has a vertical tangent in the FNPF model. We expect to have the largest effects of non-linearity at this location.

For the first case, where $\delta = 0.2$ and slope is 1:100, the predictions of the Boussinesq models agree well with the FNPF solution at $t = t_1$. However, as the wave propagates shoreward, the Wei *et al.* (1995) model tends to over-estimate the wave height and the present model tends to under-estimate the wave heights. The FNPF model shows a decrease in wave height just before breaking which is not represented by either of the two Boussinesq models. Of the four cases shown, the differences between the Boussinesq models and the FNPF model are most evident in this case. In the other three cases, although not very visible in this plot, the Wei *et al.* (1995) model consistently over-estimates the height of the wave crest, whereas the present model consistently under-estimates the height of the wave crest.

In addition, the wave profiles from the two fully non-linear Boussinesq models are also slightly different from that given by the FNPF model. The Wei *et al.* (1995) model gives a slightly narrower crest and the present model gives a slightly wider crest. Another point of interest is that the wave celerity predicted by the two Boussinesq models is larger than that given by the FNPF model. This is observed from the location of the front face of the wave predicted by the Boussinesq models compared to those predicted by the FNPF model at the same time.

It was mentioned in Chapter 2 that the slope terms are small and hence can be neglected in the non-linear terms of $O(\delta\mu^2)$. Figure 5.4 shows the results for the solitary wave shoaling for the same situations as in figure 5.3, this time comparing the present model with and without the h_x, h_{xx} and h_{xxx} terms to the FNPF model. As is evident, there is no significant difference, even for a very steep beach of 1:8. Therefore, we can deduce that the h_x terms are indeed small and can be neglected

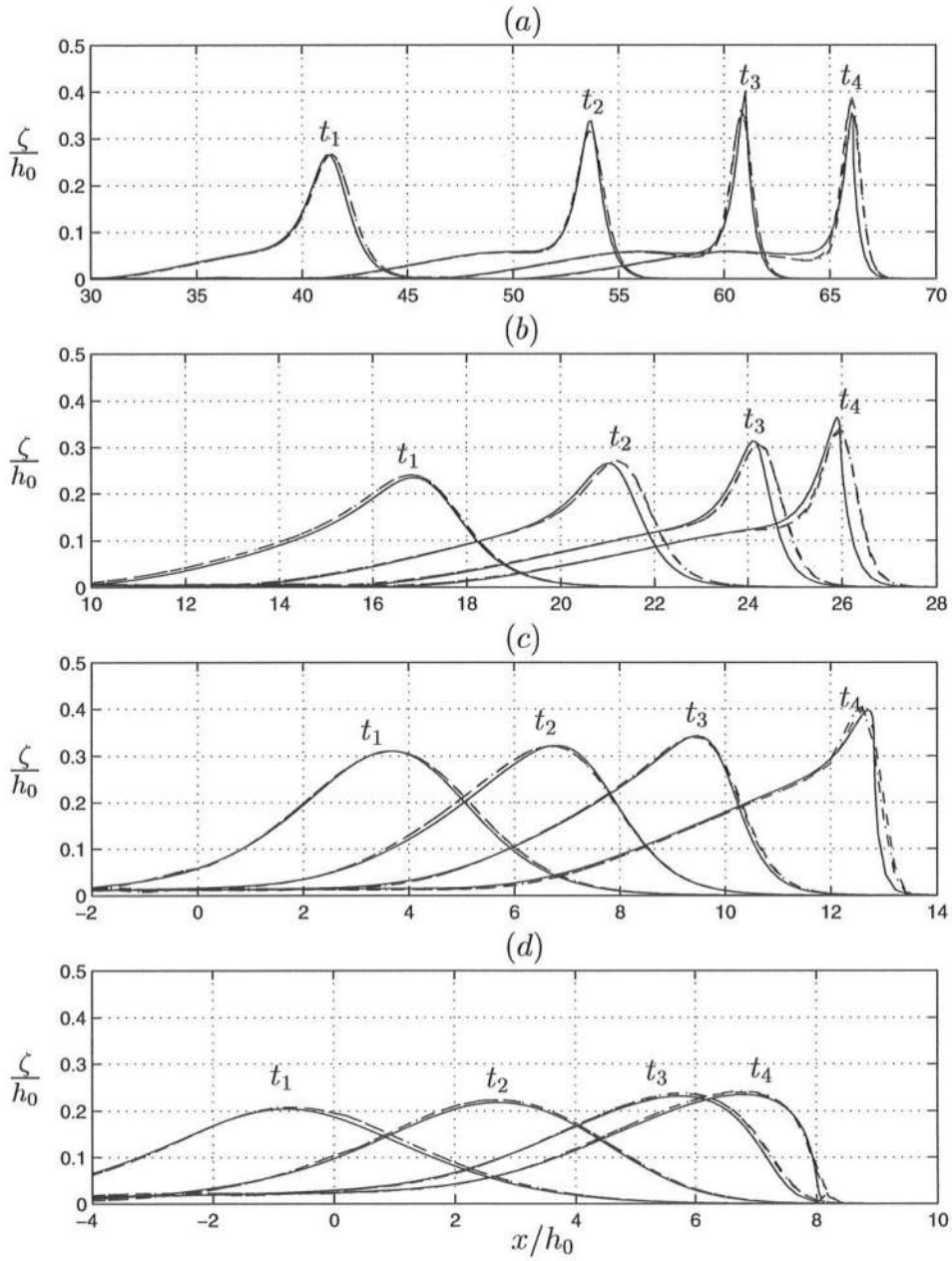

Figure 5.4: Comparison of surface elevations for solitary waves shoaling on plane beaches between the FNPF model (———), the fully non-linear $\zeta - \overline{u}$ model with the slope terms included (– – –) and the fully non-linear $\zeta - \overline{u}$ model without the slope terms (–·–·–).

for the breaking terms as well.

5.2 Model characteristics.

Before the model results are presented, we first look at some of the characteristics of the breaking model. First, we look at the vorticity field in the breaking waves. The model domain is similar to that shown in figure 5.2. For this case, the beach slope is 1:35, the wave height at the constant depth section is 12.5 *cm* and the wave period is 2.2 *secs*. These values correspond to the experimental conditions of Cox *et al.* (1995) described later. Figure 5.5 shows the vorticity contours, with 5.5(a) showing the contours just after wave breaking starts, 5.5(b) a little distance into the surf zone and 5.5(c) well into the surf zone. Figure 5.6 shows the vertical profiles of the vorticity at these same locations concentrating more in the region of the roller.

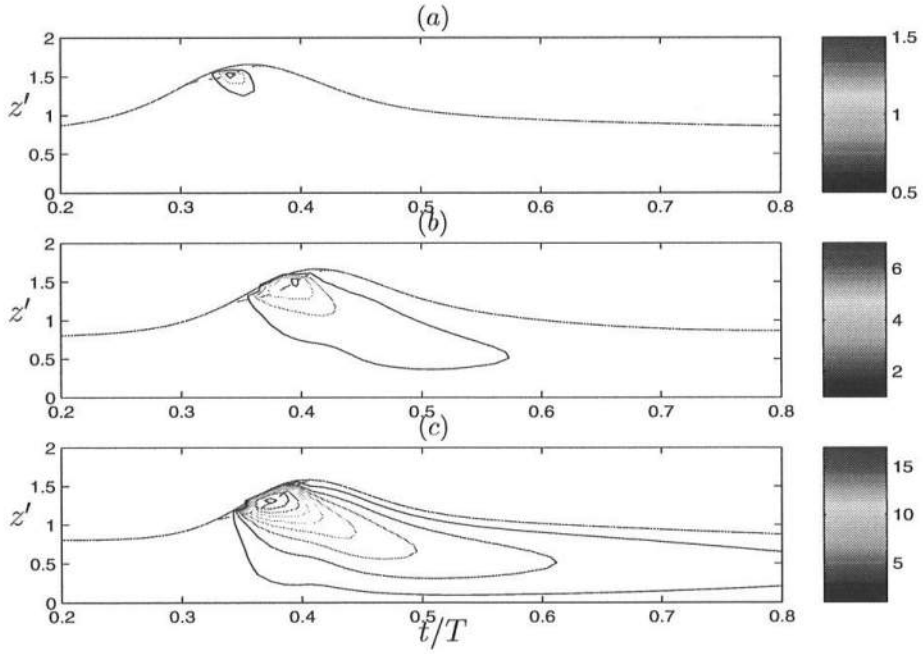

Figure 5.5: Contours of the vorticity under the wave at three locations in the surf zone. The vertical axis is $z' = (z+h)/h$ and the horizontal axis is the time normalized by the wave period. (a) $h/h_b \sim 1$ (b) $h/h_b = 0.9$ (c) $h/h_b = 0.5$

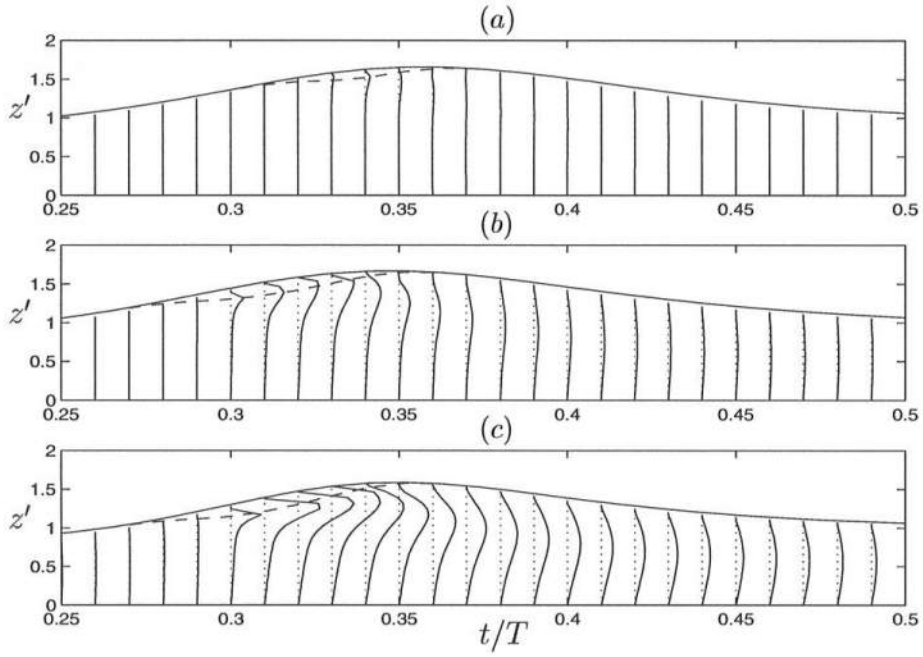

Figure 5.6: Profiles of the vorticity under the wave at three locations in the surf zone shown in figure 5.5. Again, the vertical axis is $z' = (z + h)/h$ and the horizontal axis is the time normalized by the wave period. (a) $h/h_b \sim 1$ (b) $h/h_b = 0.9$ (c) $h/h_b = 0.5$

Observations of waves in the laboratory (see, e.g., Lin and Rockwell 1994) show that the vorticity produced in the roller is convected downward and towards the back of the wave. This feature is also seen from the measurements in hydraulic jump (see Chapter 3). As is expected, the figures show the same feature. Also, for a wave that is a fully developed breaker, the absolute maximum of the vorticity in the wave occurs very shortly after the toe of the roller has passed by. Along each vertical section, it is only close to the toe that the maximum of the vorticity is close to the lower edge of the roller. From approximately halfway through the roller region, the maximum of the vorticity is found below the lower limit of the roller. The maximum vorticity remains well below the surface as the vorticity decays downstream of the roller on the back side of the wave. This result is similar to that observed in hydraulic jumps (figure 3.12) and Lin and Rockwell (1994). Thus, this important feature of the vorticity is also captured by the model.

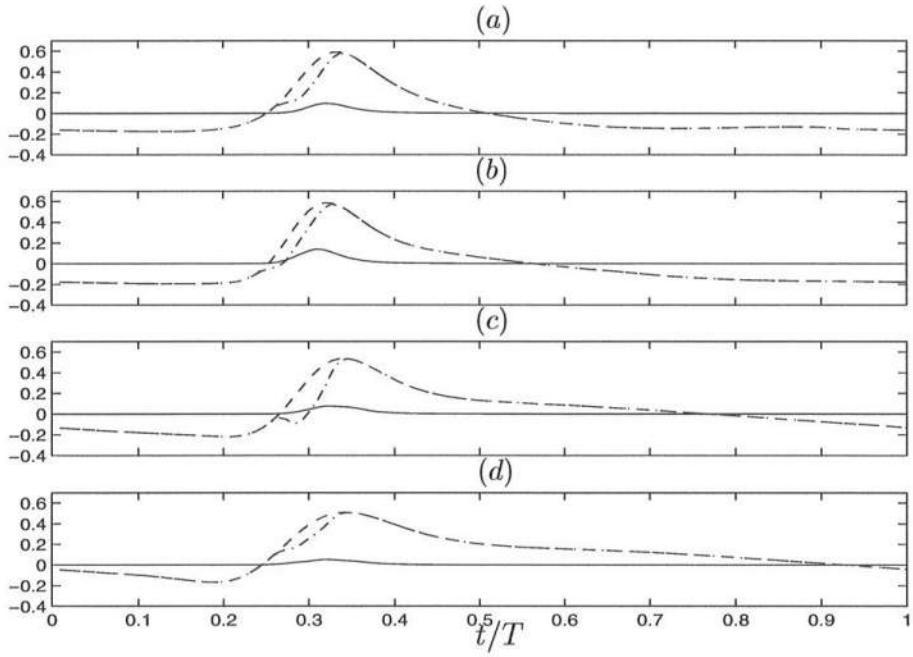

Figure 5.7: Variation of $\Delta M/M$ (———) in surf zone waves (a) $h/h_b \sim 0.84$ (b) $h/h_b = 0.67$ (c) $h/h_b = 0.5$ (d) $h/h_b = 0.35$. The water surface ζ/h (– – –) and the roller ζ_e/h (–·–·–) are also shown.

Figure 5.7 shows the variation of of the normalized excess momentum flux $\Delta M/M$ as the breaking waves propagate towards shore. One feature is that the magnitude of ΔM decreases towards the shore line. The maximum value of $\Delta M/M$ in the cross-shore direction is about 0.25 which is slightly smaller than the values calculated from the hydraulic jump measurements (figure 3.7). Another feature is that the maximum of ΔM is in front of the wave crest. As shown by Svendsen *et al.* (1996), this is important for the decrease in wave height in the breaking region. This feature is also seen in the hydraulic jumps (figure 3.7). It was shown by Svendsen *et al.* (1996) that if the maximum of ΔM is behind the crest, the wave heights increase in the breaking region.

Figure 5.8 shows the magnitudes of the breaking terms at $h/h_b = 0.67$, where ΔM is again the excess momentum due to the roller, ΔP is the effect of the excess pressure due to the roller, D_w is effect of the vertical motion of the fluid, D_{uw} is the effect of the mixing term and D_s is the shear stress term. The figure shows clearly

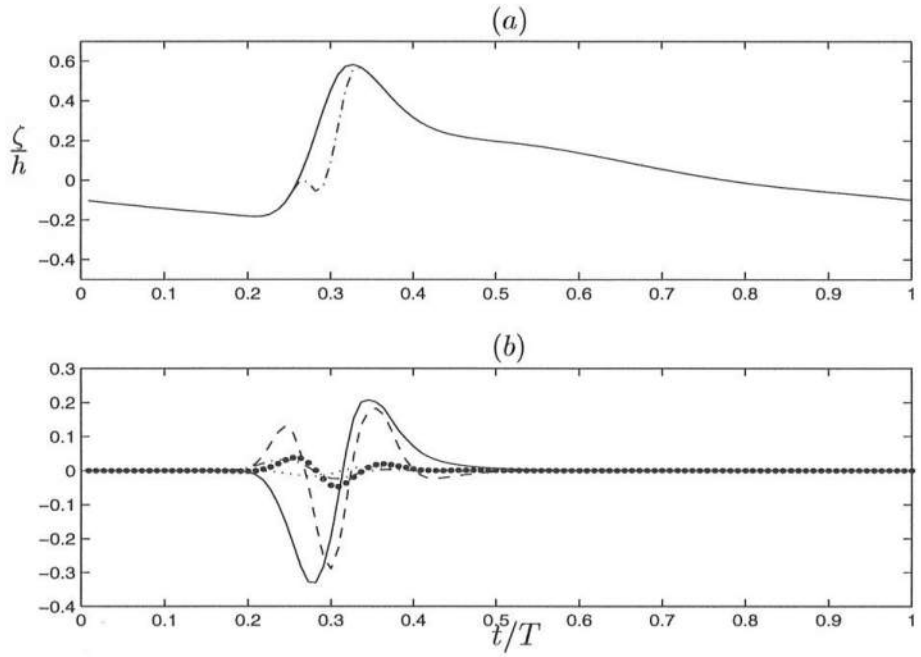

Figure 5.8: Magnitudes of the breaking terms in surf zone waves at $h/h_b = 0.67$. (a) Profile of the water surface elevation and the roller. (b) Variation of $(\Delta M)_x/M_x$ (———), $(\Delta P)_{xxt}/M_x$ (– – –), D_w/M_x (–·–·–), D_s (· · · · ·), D_{uw}/M_x (•)

that the major contributions to the breaking comes from the excess momentum (ΔM) term and the excess pressure (ΔP) term. The contributions from the roller area is included in the ΔM term. However, it turns out that the major effect of this contribution comes about as a shift in the location of the maximum of ΔM with respect to the crest. Including the contribution from the roller area shift the maximum of ΔM farther to the front of the wave crest, which enhances the breaking somewhat (Yu 1996).

It is seen from the figure that the breaking terms of $O(\delta\mu^2)$, which include the mixing terms and the turbulent stress terms, are negligible in comparison to the two main effects of excess momentum flux (ΔM) and the effect of the vertical acceleration due to the roller (ΔP_{xxt}).

Table 5.1: Wave parameters from Hansen and Svendsen (1979) at the toe of the beach.

Case No.	T $(secs)$	H (cm)	δ	$T\sqrt{g/h_0}$	I_r
wh031041	3.3333	4.3	0.12	17.4	0.65
wh041041	2.5	3.9	0.11	13.0	0.48
wh051041	2.0	3.6	0.10	10.44	0.38
wh061071	1.0	6.7	0.19	5.22	0.23

5.3 Comparisons with regular wave data.

In this section, the performance of the present model (both the fully non-linear and the weakly non-linear versions) in the shoaling region and in the surf zone is compared to experimental data for regular waves. The comparisons are shown for the wave heights, the wave profiles, the velocity field, the set-up and the undertow.

5.3.1 Wave heights.

Wave heights and set-up measurements for monochromatic waves are available from the experiments by Hansen and Svendsen (1979). Those experiments were conducted in a wave flume with a plain beach of slope 1:34.26. The water depth at the start of the slope was $h_0 = 0.36\ m$. Seventeen tests were conducted with five different wave heights and seven different wave periods. The wave heights and set-up for each case were measured at a number of locations. Comparisons will be shown for four cases for which sufficient measurements were available in the surf zone. Table 5.1 presents the wave period and the wave height at the start of the slope for each of the cases shown here.

The wave periods chosen for these comparisons range from fairly long waves ($T\sqrt{g/h_0} = 17.4$) to fairly short waves ($T\sqrt{g/h_0} = 5.22$). The computational domain is as shown in figure 5.2. The Iribarren number (equation 1.1) gives an indication of the breaking characteristics of these waves. For the first case ($I_r = 0.65$) we expect plunging breakers and in the last two cases ($I_r = 0.38,\ 0.23$) we expect spilling breakers. The second case, where $I_r = 0.48$, could be either plunging breakers or spilling breakers depending on whether the value given by Galvin (1968)

is followed ($I_r < 0.46 \Rightarrow$ spilling breakers) or that given by Battjes (1974) is followed ($I_r < 0.5 \Rightarrow$ spilling breakers).

Figure 5.9 shows the computed relative wave heights ($H(x)/h_0$) versus the non-dimensional water depth ($h(x)/h_0$) compared to the data for the four cases. In these computations, the present breaking models based on the weakly non-linear and the fully non-linear Boussinesq equations use a spectral solution to the weakly non-linear equations (Appendix C) as input at the offshore boundary. A maximum of fifteen Fourier components are used for describing the incoming wave for each case. The cut-off point N for the number of Fourier components was chosen so that the Fourier amplitude of the $(N+1)st$ component was less than $1.e^{-8}$. The Kennedy *et al.* (1999) model, which is an extension of the Wei *et al.* (1995) model, uses a sinusoidal wave corrected for the second harmonic as the input wave condition.

In the initial shoaling region it is seen from figure 5.9 that the wave heights predicted by the weakly non-linear Boussinesq model (–·–·–) compare well with the data ($\diamond$). However, as the waves get closer to the breaking point, the computed results start deviating from the measured values. The model under-predicts the wave heights close to the breaking point. This misrepresentation is smallest for 5.9(a) where the wave period is the largest (i.e., for the longest wave) and the errors are largest for 5.9(c) (the shortest wave for which computations from weakly non-linear equations are shown). As mentioned in section 4.2.4, breaking in the weakly non-linear model is initiated when the maximum slope at the front face of the wave exceeds 20°. In the outer surf zone, the difference between the computed results and the data get smaller. In the inner surf zone, the agreement between the model and the data is very good.

While the assumption of weak non-linearity may be true during the initial stages of shoaling, the non-linear effects start to dominate as the waves approach breaking. Thus, this basic assumption becomes invalid close to the region of wave breaking. Once the waves start breaking, the wave heights predicted by the model decrease. The energy dissipation due to wave breaking is proportional to H^3. Therefore, the energy dissipation in the model is smaller than that for the data and hence so is the decrease in wave height. Once the wave heights computed by the model

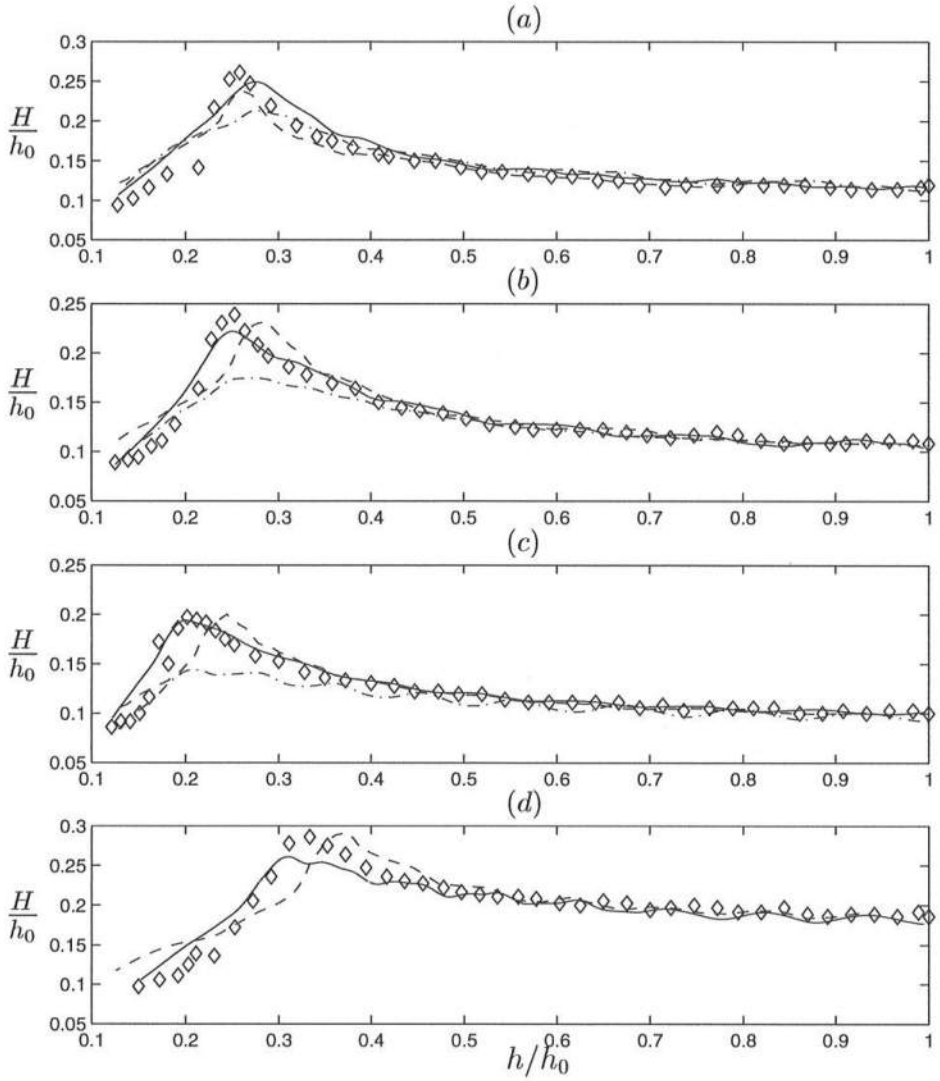

Figure 5.9: Comparison of wave heights with experimental data from Hansen and Svendsen (1979) ($\diamond$), for waves shoaling and breaking on a gently sloping beach, using the weakly non-linear model (–·–·–), the fully non-linear model (———) and the Kennedy *et al.* (1999) model (– – –).

are close to those given by the data, the energy dissipation is also equivalent. This results in a better prediction of the wave heights in the inner surf zone.

The performance of the present fully non-linear model (———, figure 5.9) is very good throughout the computational domain. The wave heights are slightly under-predicted just before breaking is initiated. As mentioned in section 4.2.4, wave breaking for the fully non-linear model is initiated when the maximum slope at the front face of the wave α_b exceeds 32° which corresponds to $\zeta_x = 0.63$. In general, the start of wave breaking in the model is at a slightly small water depth than for the data. The wave heights are slightly over-predicted in the surf zone, especially in the region just after breaking starts. This discrepancy is the largest for the first two cases, where we can expect plunging breaking. The main reasons for this mismatch are the misrepresentation of the start of breaking and that limited information is available about the development of the roller immediately after breaking starts.

With the fully non-linear Kennedy *et al.* (1999) model (– – –, figure 5.9), the computed wave heights are slightly larger than the data in the region just before breaking. For this model breaking was initiated when the maximum slope at the front face of the wave was larger than $\zeta_x = 0.65$ ($\alpha_b \simeq 33°$). For this model, the start of wave breaking is at a slightly larger water depth than that in the data. In general, we see that the prediction of wave heights in the surf zone is poorer for this model than for the present fully non-linear model.

In all four cases, the value of the eddy viscosity used in the computations is $\nu_t = 0.04h\sqrt{gh}$ in the surf zone for both the weakly non-linear and the fully non-linear models. However, the value of this parameter is uncertain (see figures 3.14, 3.15 and also Cox *et al.* (1995)). The value of eddy viscosity chosen here corresponds to the value that gave the best undertow profile to the weakly-nonlinear model compared to the data of Cox *et al.* (1995) (discussed in the next part). Experiments by Cox *et al.* (1995) show that the average magnitude of the eddy viscosity in the surf zone in those measurements is about $\nu_t = 0.03h\sqrt{gh}$. To illustrate the effect of a smaller value of ν_t, figure 5.10 shows the wave height variation for $\nu_t = 0.03h\sqrt{gh}$. This decrease in ν_t results in a decrease in the strength of breaking and leads to larger wave heights in the surf zone. However, it is seen that this increase in wave height

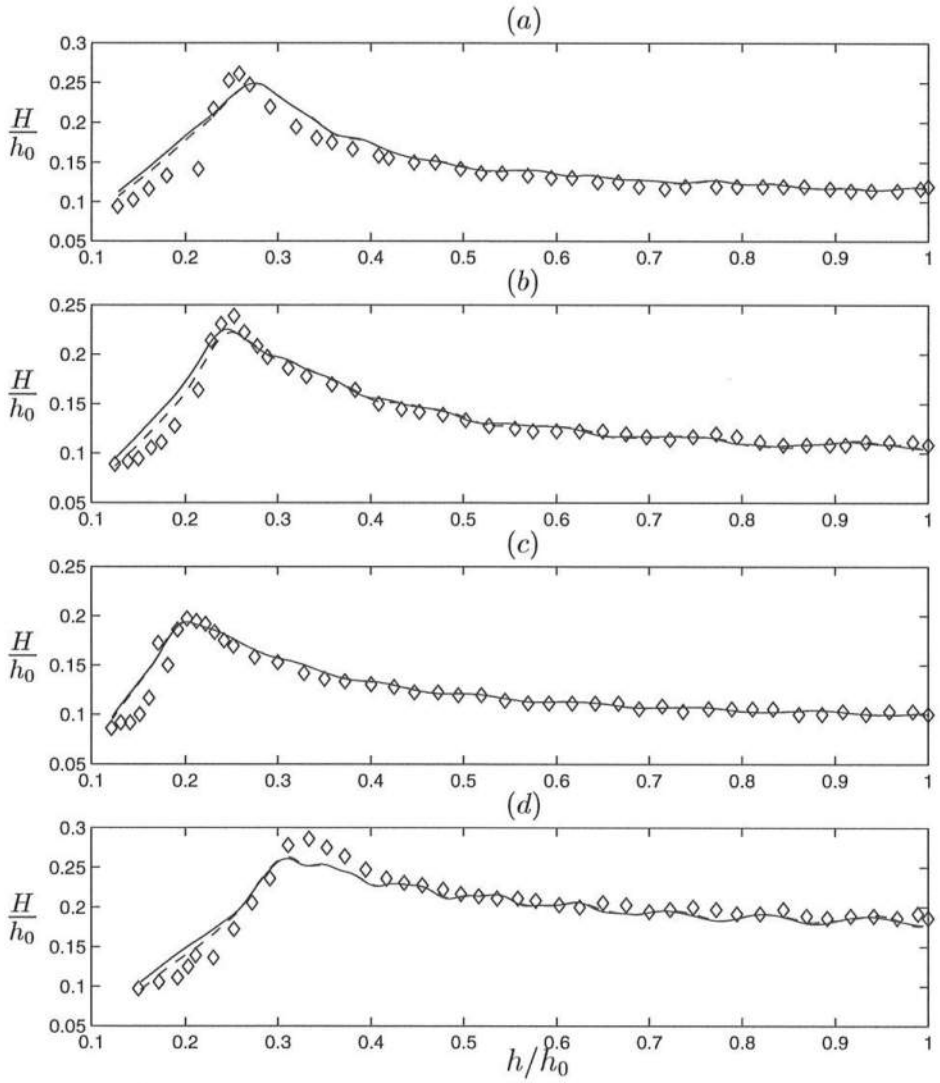

Figure 5.10: Comparison of wave heights with experimental data from Hansen and Svendsen (1979) ($\diamond$) and the fully non-linear model: $\nu_t = 0.03h\sqrt{gh}$ (———), $\nu_t = 0.04h\sqrt{gh}$ (– – –).

is within the uncertainty of the measurements. Thus, the wave height predictions are to some extent not very sensitive to variations of the eddy viscosity as long as the magnitude of the eddy viscosity used is within the range that can be justified on the basis of our present knowledge.

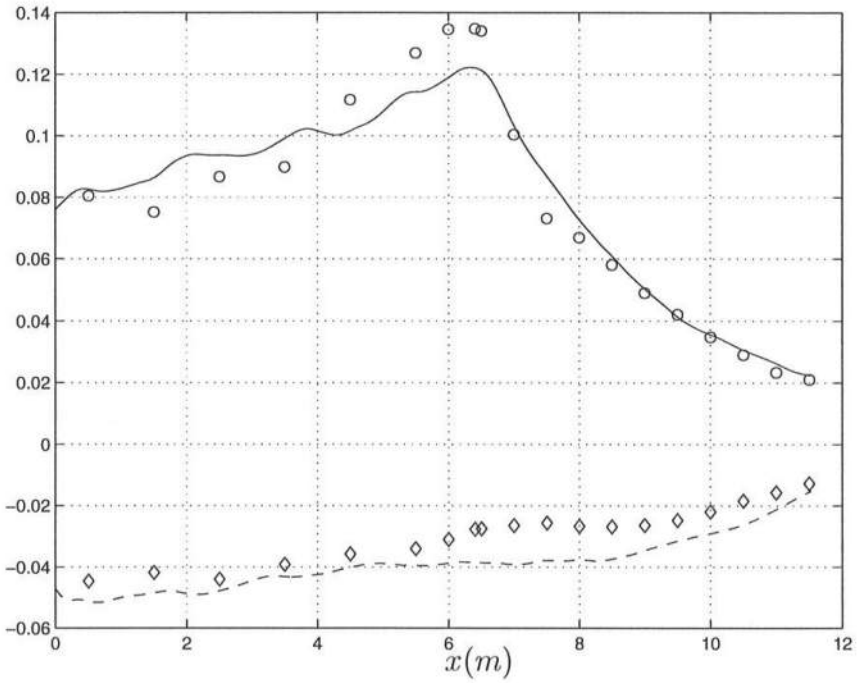

Figure 5.11: Comparison of wave crest elevations (———) and trough depressions (– – –) with experimental data (○ and ◇) from Ting and Kirby (1994).

Figure 5.11 shows the comparison between the model and the data of Ting and Kirby (1994). These experiments were conducted on a plane beach of slope 1:35. Cnoidal waves of height $H = 12.5\ cm$ and wave period $T = 2.0\ secs$ were generated at the wave-maker. The toe of the beach is at $x = 0\ m$. The Iribarren number was around 0.2, which indicates that the waves are spilling breakers. The breaking depth in the measurements was given as $h = 19.6\ cm$. The eddy viscosity used in the computations is $\nu_t = 0.04h\sqrt{gh}$. The figure compares the crest and trough elevations at different locations in the wave tank. Again, we see that the representation of the

data is very good. The maximum error in the prediction of the crest elevations (approximately 8%) occur just before the model predicts breaking (at $h \sim 21\ cm$). In the breaking region, the crest elevations are represented extremely well. On the other hand, for the trough elevation, the errors in the prediction is much larger (approximately 40% close to breaking) and the agreement is not good compared to the agreement in the crest elevations.

5.3.2 Surface profiles.

Next, the surface profiles are compared to the data of Cox *et al.* (1995). The experiments were conducted in a wave flume with a plain beach slope of 1:35. Cnoidal waves were generated at the wave-maker with height $H_0 = 11.5\ cm$ and wave period $T_0 = 2.2\ secs$. The water depth at the toe of the beach was $h_0 = 0.40\ m$. The Iribarren number is approximately 0.23, which indicates that these waves are spilling breakers.

Measurements were taken at the six locations shown in table 5.2. The first two measurement locations were outside the breaking region with the second location very close to the breaking point. The third location was in the transition region where the breaker is not fully developed into a bore form. The last three locations were in the inner surf zone where the breakers are quasi-steady.

Table 5.2: Location of measuring lines for the data of Cox *et al.* (1995)

Line No.	L1	L2	L3	L4	L5	L6
h (cm)	28.0	21.14	17.71	14.29	10.86	7.43

Figure 5.12 shows the wave profiles from the data (———), the computed wave profiles from the fully non-linear breaking model (– – –) and the weakly non-linear model (–·–·–). At the first location, (figure 5.12(a); $h = 28.0\ cm$) which is in the shoaling region, the model predictions compare well with the data. The weakly non-linear model under-predicts the crest height slightly and has a slightly wider crest. In contrast, the fully non-linear model gets the wave shape almost exactly correct.

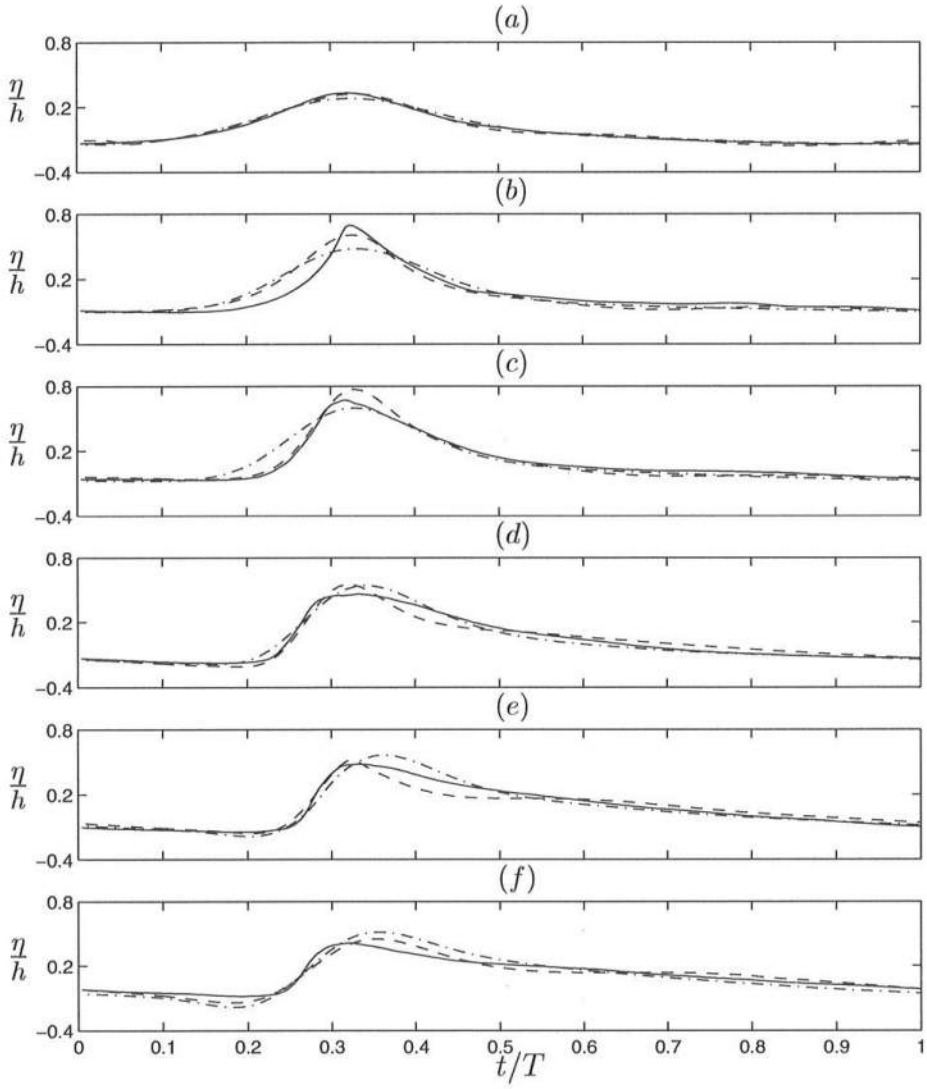

Figure 5.12: Comparison of surface profiles between the weakly non-linear breaking model (–·–·–), the fully non-linear breaking model (– – –) with experimental data from Cox *et al.* (1995) (———).

At the next location (figure 5.12(b); $h = 21.14\ cm$) where the data show that the waves are just about to break, the model results do not match very well. The front face of the wave profiles shown by the data has much steeper slopes than those computed by the model. The weakly non-linear model gives a much wider crest than the fully non-linear model. Also, the crest height prediction is better with more non-linearity included.

In the "transition" region (figure 5.12(c); $h = 17.71\ cm$) where the waves are breaking but have not completely transformed into quasi-steady bore forms, the crest height representation by the weakly non-linear model is good. The fully non-linear model predicts a larger crest height at this location. On the other hand, the wave shape is much better predicted by the fully non-linear model.

As the wave propagate towards the shore (figure 5.12(d)-(e); $h = 14.29\ cm$, $10.89\ cm$ and $7.43\ cm$), the fully non-linear model starts to represent the wave profiles better than the weakly non-linear model. However, the slopes on the wave fronts predicted by the model never really come close to that seen in the data.

This feature, that the wave shape described by the model has a wider crest than that observed from the data, was also noticed in the first section (where the solitary wave shoaling results were presented). We expect that this feature can be corrected to a large extent by keeping all terms up to $O(\mu^4)$ in the Boussinesq equations (see, e.g., Gobbi *et al.* 1999; Madsen and Schäffer 1998a).

5.3.3 Velocity profiles.

Cox *et al.* (1995) also measured the horizontal velocities at the six locations shown in table 5.2 using a LDV, with a Burst Spectrum Analyzer. The velocity measurements were obtained at a number of vertical locations up to the mean water level, and the data were available up to the still water level.

Figure 5.13 shows the comparison between the model results and the measured velocities. For reference, the water surface elevation from the model and the data are reproduced. In addition, the dotted lines mark the phase at which the velocities are measured, as well as the zero of the velocities at that phase. The horizontal line at the top right of each plot is the wave speed at that location, calculated from the model. The calculation of the wave speed from the model computations

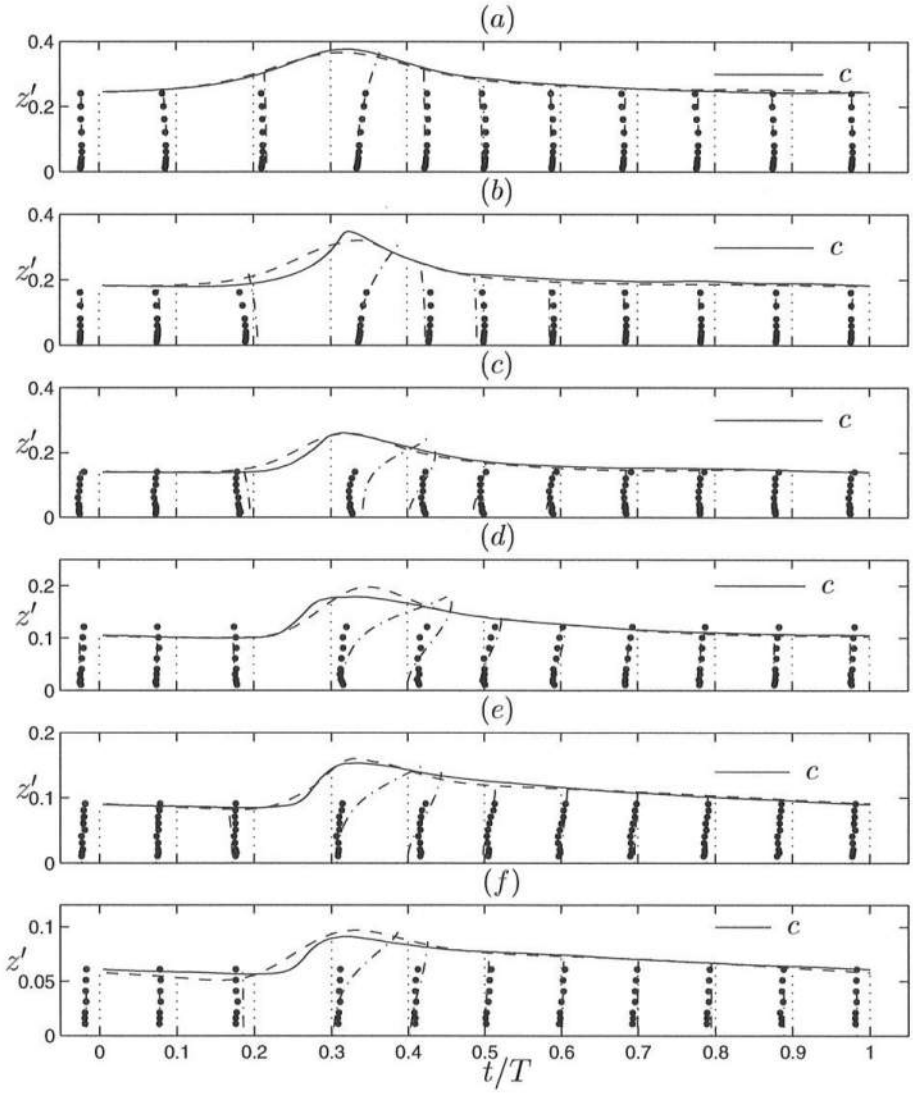

Figure 5.13: Comparison of velocity profiles between the fully non-linear breaking model (– · – · –) with experimental data from Cox *et al.* (1995) (•) at 11 phases. Water surface elevation: Model (– – –), data (———). The horizontal line at the top right of each sub-plot is the magnitude of the wave speed. The ordinate $z' = z - h$ is zero at the bottom.

is shown in the next section. The abscissa in the figure is normalized by the wave period.

The agreement between the computed and the measured velocities are excellent in most of the region. Under the wave crest, the model tends to predict a slightly larger velocity. This difference is likely caused by two factors. The first factor is that the predicted wave surface is different from the measured surface elevation. Figure 5.13(a) shows that, at least in the shoaling region, when the surface elevation is predicted well, the velocity predictions follow suit. In the surf zone (figures 5.13(c)-(f)), it is again noticed that at the phases where the surface profiles determined by the model matches that in the data, the velocity predictions are also good.

The second factor is the assumption of a constant eddy viscosity over the water column. Measurements in hydraulic jumps (figure 3.15) as well as in monochromatic wave fields (Cox *et al.* 1995) show that the magnitude of the eddy viscosity decreases from the surface to the bottom. This assumption of a constant eddy viscosity diffuses the vorticity generated by the roller downward into the water column faster than if the eddy viscosity was decreasing towards the bottom. This, in turn, causes an increase in the rotational component of the velocity (which is always positive for a positive vorticity) in the lower part of the water column.

Figure 5.14 shows the computed horizontal velocities from the weakly non-linear model for the same data set. As in the case of the fully non-linear model, the computed velocities compare well with the measured velocities at the locations where the surface profiles match. However, for the weakly non-linear model, the agreement between the surface elevations is worse than that computed using the fully non-linear model. Therefore, the computed velocities are off-target at more locations. In addition, the predicted particle velocities at the surface are smaller than that observed in the fully non-linear model.

5.3.4 Set-down and set-up.

Another important gauge for the model performance is the prediction of wave set down and set-up. The results from the three Boussinesq models (the present fully non-linear model, the weakly non-linear model and Kennedy *et al.* (1999)

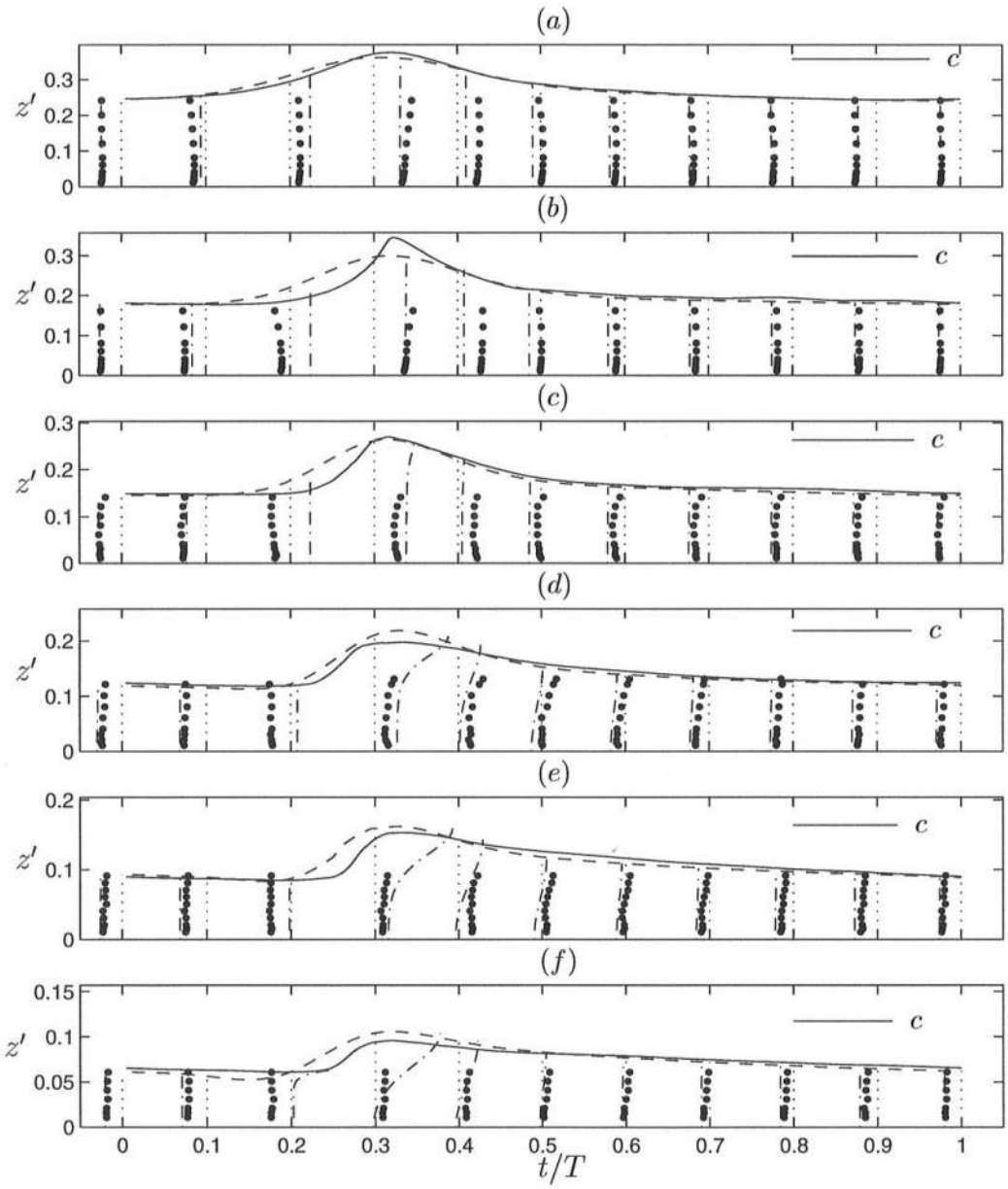

Figure 5.14: Comparison of velocity profiles between the weakly non-linear breaking model (– · – · –) with experimental data from Cox *et al.* (1995) (•) at 11 phases. Water surface elevation: Model (– – –), data (———). The horizontal line at the top right of each sub-plot is the magnitude of the wave speed. The ordinate $z' = z - h$ is zero at the bottom.

model) are compared to the data of Hansen and Svendsen (1979). The parameters of this data set were given in table 5.1.

Figure 5.15 shows that the set-down as well as the set-up predicted by the present version of the weakly non-linear model (–·–·–) is good in comparison to the data for the case of the longest wave (figure 5.15a). In the other two cases, the mean water level is over-predicted by this model. The deviations between the computed results and the data can be deduced by looking at the wave height comparisons in figure 5.9. The decrease in wave height during the early stages of breaking in the present model is somewhat smaller than in the data. The cross-shore radiation stress S_{xx} is proportional to H^2. Hence, the cross-shore gradient of the radiation stress computed by the model will be smaller than for the data. The relation between the mean water level and the radiation stress for steady state in the absence of bottom friction is

$$\frac{\partial S_{xx}}{\partial x} = -\rho g h \frac{\partial \overline{\zeta}}{\partial x} \tag{5.6}$$

where $\overline{\zeta}$ is the mean water surface. Thus, the smaller shoaling predicted by the weakly non-linear model implies a smaller gradient in the set-down computed by the model. Similarly, the smaller decrease in wave height in the outer surf zone leads to a smaller gradient in the set-up in this region.

Figure 5.15 also shows the mean water level predicted by the present fully non-linear model (———) and the Kennedy *et al.* (1999) model. The results from the fully non-linear models represent the results from the data better than the weakly non-linear model.

5.3.5 Undertow profiles.

In contrast to other Boussinesq breaking models, the present model has the capability to predict undertow, as well as other wave averaged quantities. To estimate these quantities, the vertical distribution of the velocities is required. In this section, this feature of the model is demonstrated by comparing the computed results to two sets of data mentioned before: Cox *et al.* (1995) and Ting and Kirby (1994).

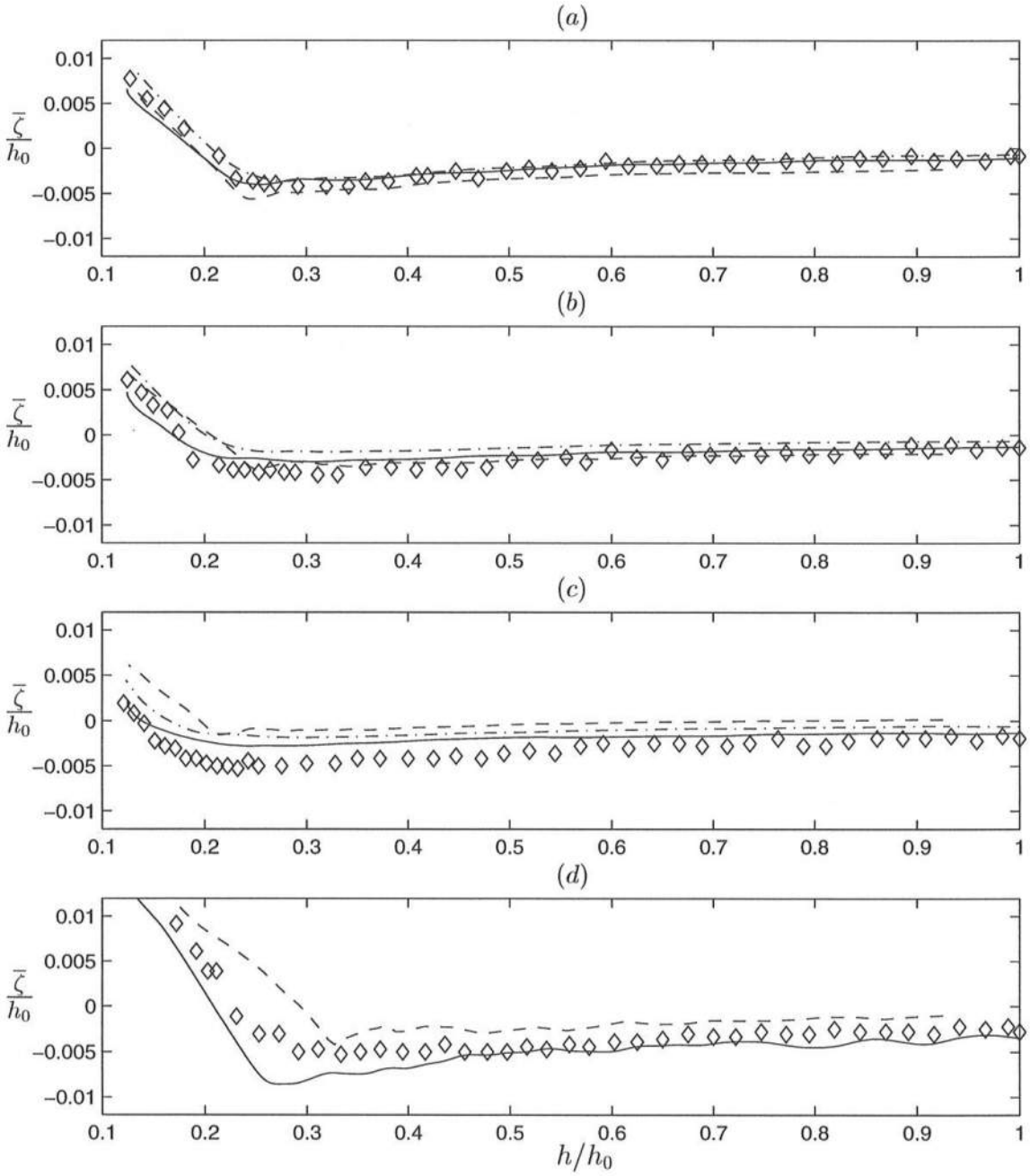

Figure 5.15: Comparison of mean water level with experimental data from Hansen and Svendsen (1979) ($\diamond$), for waves shoaling and breaking on a gently sloping beach, using the weakly non-linear model (–·–·–), the fully non-linear model (———) and the Kennedy *et al.* (1999) model (– – –).

When starting the computations of the waves from a cold start (i.e., there are no waves in the domain), a significant surge is initiated in the tank. After this surge has settled, there is a strong seaward mass flux near the bottom, which is called the undertow. The undertow is particularly pronounced inside the surf zone.

The total horizontal velocity u can be separated into an oscillatory component u_w and a current component V. This current component is a constant over a wave period. The total mass flux over a wave period is then given by

$$\overbrace{Q} = \overbrace{\int_{-h}^{\zeta} (u_w + V)\, dz} \tag{5.7}$$

where the $\overbrace{()}$ represents the averaging over a wave period. The oscillatory (or wave) component is defined such that the average velocity $\overbrace{u_w}$ below trough is zero. This also implies that the mass flux due to waves below the trough level is zero, and therefore

$$\overbrace{Q} = \overbrace{\int_{\zeta_t}^{\zeta} u_w\, dz} + \int_{-h}^{\bar{\zeta}} V\, dz \tag{5.8}$$

where the first integral on the right is the mass flux $\overbrace{Q_w}$ due to the wave motion. The undertow $V(z)$ is then calculated as the wave averaged value of u at any vertical location below trough.

Figure 5.16 shows the model results from the weakly non-linear (– – –) and fully non-linear (———) models and the data of Cox *et al.* (1995). The results are shown for the measurement locations where the waves in the data are breaking, up to the wave trough limit in the vertical direction. Figure 5.16(a) is the comparison in the transition region. The computed results in this region are affected by the fact that the start of breaking is different in the model in comparison to the data. Even so, the model gives a good representation of the undertow profile. Figure 5.16(b)-(d) are in the inner surf zone and in this region, the results from the model agree well with the data. Recall that in the present version of the breaking models, the effect of bottom friction is not accounted for. Therefore, a finite velocity is obtained at the bottom in the model predictions.

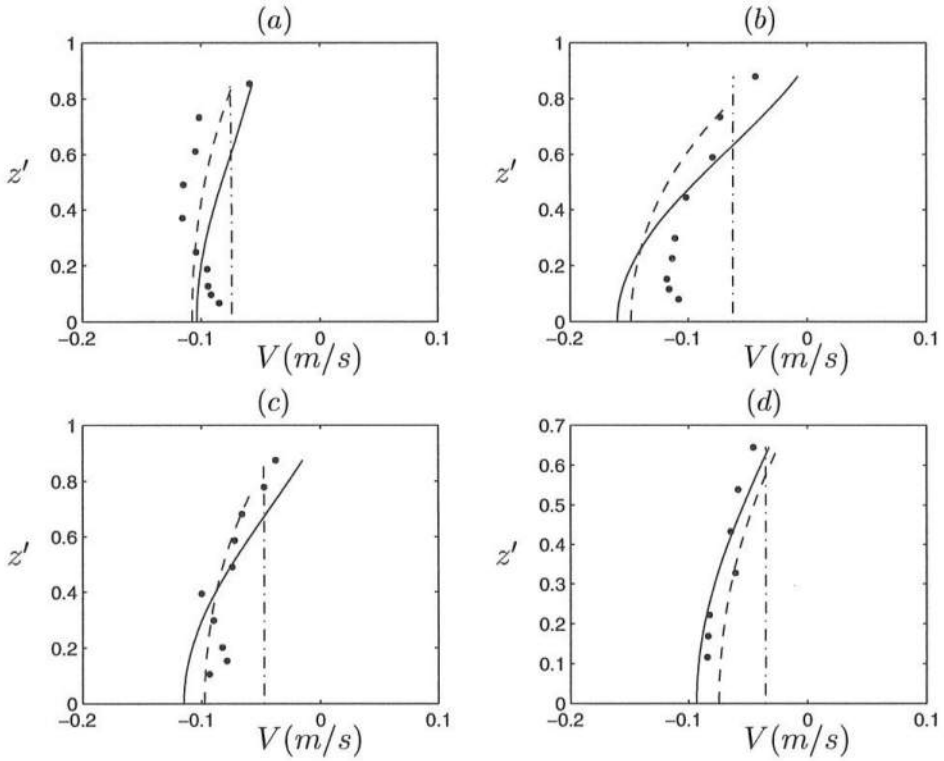

Figure 5.16: Comparison of the undertow profiles between the fully non-linear model (———), the weakly non-linear model (– – –), fully non-linear model using potential flow assumption (–·–·–) and the data from Cox *et al.* (1995) (•). $z = 0$ is the bottom. The vertical axis is $z' = (h + z)/(h + \overline{\zeta})$. Plots (a), (b), (c) and (d) correspond to L3, L4, L5 and L6 in table 5.2 respectively.

As can be seen from the figure, the effect of the bottom boundary layer further into the surf zone (figures 5.16c and 5.16d) is limited to a very narrow region near the bottom. This is in spite of the fact that in these measurements, the bottom roughness was enhanced by sand particles glued to the bottom. In the region where the effect of the bottom boundary does not penetrate far into the water column, the difference between the computed and measured values is very small.

Figure 5.16 also shows the computed undertow assuming potential flow in the surf zone (–·–·–). In this case, the horizontal velocity is given by the potential

part in equation (2.41)

$$u(x,z) = \overline{u} + \mu^2(\frac{\Delta_1}{2} - z)(h\overline{u})_{xx} + \frac{\mu^2}{2}\left(\frac{\Delta_2}{3} - z^2\right)\overline{u}_{xx} \tag{5.9}$$

where $\overline{u}$ is the depth averaged velocity. The effect of the rotational component of the velocity is still included in the momentum equation as the breaking terms. It is evident that this assumption of potential flow does not yield a very good prediction of the undertow.

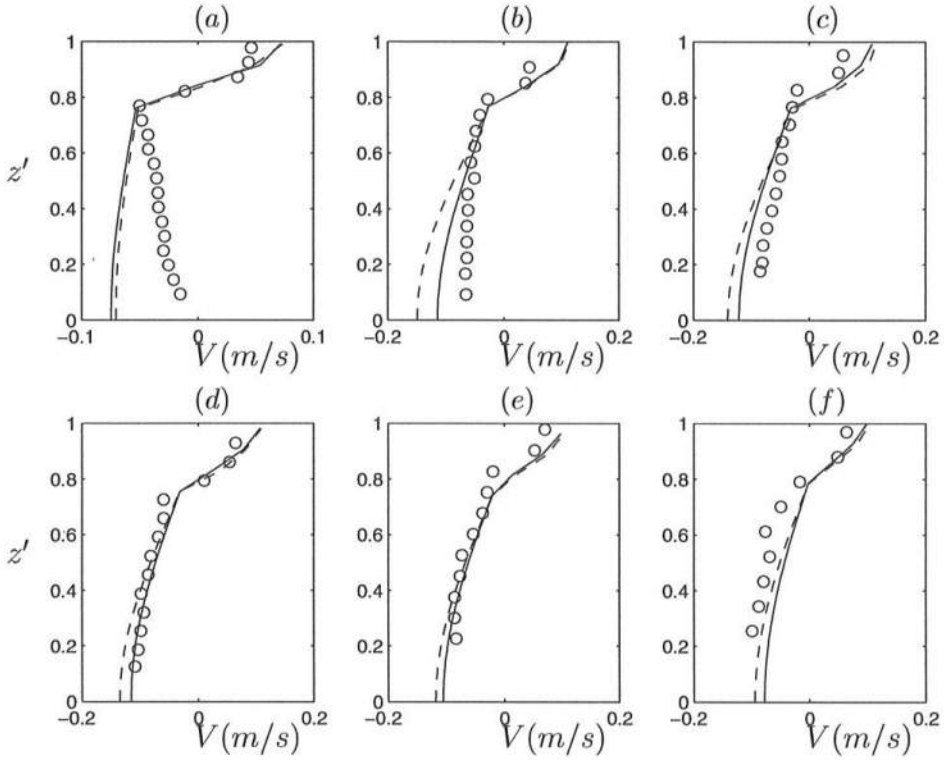

Figure 5.17: Comparison of the undertow profiles between the fully non-linear model with $\nu_t = 0.04h\sqrt{gh}$ (———), with $\nu_t = 0.03h\sqrt{gh}$ (– – –) and data from Ting and Kirby (1994) (○). The vertical axis is $z' = (h+z)/(h+\overline{\zeta})$.

Figure 5.17 shows the comparison between the wave-averaged velocities from the fully non-linear model and the data of Ting and Kirby (1994). The locations at which the comparisons are shown are given in table 5.3.5. As mentioned in section 5.3.1, the waves were said to break at a depth of $h = 0.196\ m$. However, the

Table 5.3: Locations at which comparisons to Ting and Kirby (1994) data are shown in figure 5.17. x is the location, in meters, from the toe of the beach and h is the still water depths at these locations.

Sub-plot	(a)	(b)	(c)	(d)	(e)	(f)
$x\ (m)$	6.665	7.275	7.885	8.495	9.11	9.725
$h\ (m)$	0.185	0.169	0.152	0.137	0.119	0.097

undertow profile at $h = 0.185\ m$ (figure 5.17a) seems to suggest that the waves are not breaking at this location. Again, due to the omission of the bottom friction, the model results at this location do not compare well with the measurements. On the other hand, further into the surf zone it is seen that the agreement between the model results and the data is again very good.

The measurements in this case extend up to the mean water level. Between the trough and the crest, the net flow is shoreward. The computed wave averaged velocities show that even in this region, the agreement between the model results and the data is very good.

The figures also shows the results of using two different values of the eddy viscosity: $\nu_t = 0.03h\sqrt{gh}$ (– – –) and $\nu_t = 0.04h\sqrt{gh}$ (———). It is seen that decreasing the eddy viscosity has the effect of increasing the magnitude of the undertow. This feature was also reported by Svendsen *et al.* (1987) who mention the sensitivity of the undertow to the magnitude of the eddy viscosity.

The reason for this increase in the magnitude of the undertow corresponding to a decrease in the magnitude of the eddy viscosity can be explained as follows. With a smaller value of the eddy viscosity, the vorticity is diffused slower down into the water column. This implies that the magnitude of the vorticity at the surface is larger for a smaller magnitude of ν_t. Consequently, the velocities close to the water surface in the region of the wave crest will be larger when the magnitude of ν_t is smaller. Hence, by conservation of mass, the shoreward mass transport will also be larger which leads to a larger return flow.

5.4 Evaluation of phase-averaged quantities.

A phase-resolving model such as the Boussinesq-type model presented here has the advantage that the individual short wave properties can be obtained directly from the computations. The phase-averaged properties such as the wave mass flux and the radiation stress can be directly computed. This section illustrates the differences between obtaining the results directly from the model computations and obtaining the same results using the model prediction of wave heights as input to the results given by linear theory.

5.4.1 Mass flux.

Equation (5.7) can also be written as

$$\widehat{Q} = \overbrace{\int_{\zeta_t}^{\zeta} (u_w + V)\, dz}^{} + \int_{-h}^{\zeta_t} V\, dz \tag{5.10}$$

In this form, the equation illustrates the difficulties with determining the mass flux $\widehat{Q_w}$ in the short wave motion, because above trough level we cannot readily define a mean velocity and hence cannot separate the oscillating component u_w of the motion from the mean. Only the total velocity $u_w + V$ is known above trough level. In order to determine the value of Q_w we need to define the mean value V above trough level. This can apparently be done in several ways and the choice does influence what we get for Q_w. It is emphasized, however, that this does not mean that the integrated results are inaccurate, because what is not included in V is included in u_w and vise versa. Hence, in the time averaged momentum equation, changes in the way we divide the velocity above trough level will show up as changes in what is counted as radiation stress and what is included in the nonlinear current terms. Outside the surf zone, the current is almost constant over depth. Hence it is natural to extrapolate V to $\overline{\zeta}$ from ζ_t. Inside the surf zone, however, V is far from a constant. Hence some of the choices we can make are

$$V = \frac{\widehat{Q}}{h + \overline{\zeta}}; \qquad \zeta_t < z < \overline{\zeta} \tag{5.11a}$$

$$V = V(\zeta_t); \qquad \zeta_t < z < \overline{\zeta} \tag{5.11b}$$

$$V = \frac{\widehat{Q}}{h + \zeta_t}; \qquad \zeta_t < z < \overline{\zeta} \tag{5.11c}$$

The non-dimensional mass flux is defined as

$$Q'_w = \frac{h}{cH^2} Q_w \tag{5.12}$$

where c is the phase speed of the wave, h is the local water depth and H is the local wave height. Figure 5.18 shows the calculated wave mass flux for the four cases of Hansen and Svendsen (1979) (figures 5.18(a)-(d)), the wave conditions of Cox *et al.* (1995) (figure 5.18(e)) and that of Ting and Kirby (1994) (figure 5.18(f)). The mass flux calculated using the formula given by linear wave theory

$$Q'_w = \frac{1}{8} \frac{gh}{c^2} \tag{5.13}$$

is also shown for comparison. It is seen that the non-dimensional wave mass flux decreases as the waves approach breaking. In all cases, in this region the model results show a smaller mass flux than that calculated using linear theory. Linear theory does not account for the asymmetry of the waves as they shoal, and hence predicts a larger mass flux. Once the waves break, the non-dimensional mass flux increases. Figures 5.18(d)-(f) show that after some distance the mass flux reaches some value after which it stays reasonably constant in the surf zone.

The figures also show the difference in the computed mass flux for the different choices (5.11a)-(5.11c). Using (5.11a) or (5.11c) gives almost identical results. However, using (5.11b) gives a slightly larger value for the mass flux.

5.4.2 Radiation stress.

The wave radiation stress is defined as

$$S_{xx} = \overbrace{\int_{-h}^{\zeta} (\rho u_w^2 + p_D)\, dz} + \frac{1}{2} \rho g \overbrace{(\zeta - \overline{\zeta})^2} \tag{5.14}$$

where, again the $\widehat{()}$ represents wave averaged quantities, u_w is the velocity component due to the wave only, p_D is the dynamic pressure. To the lowest order of

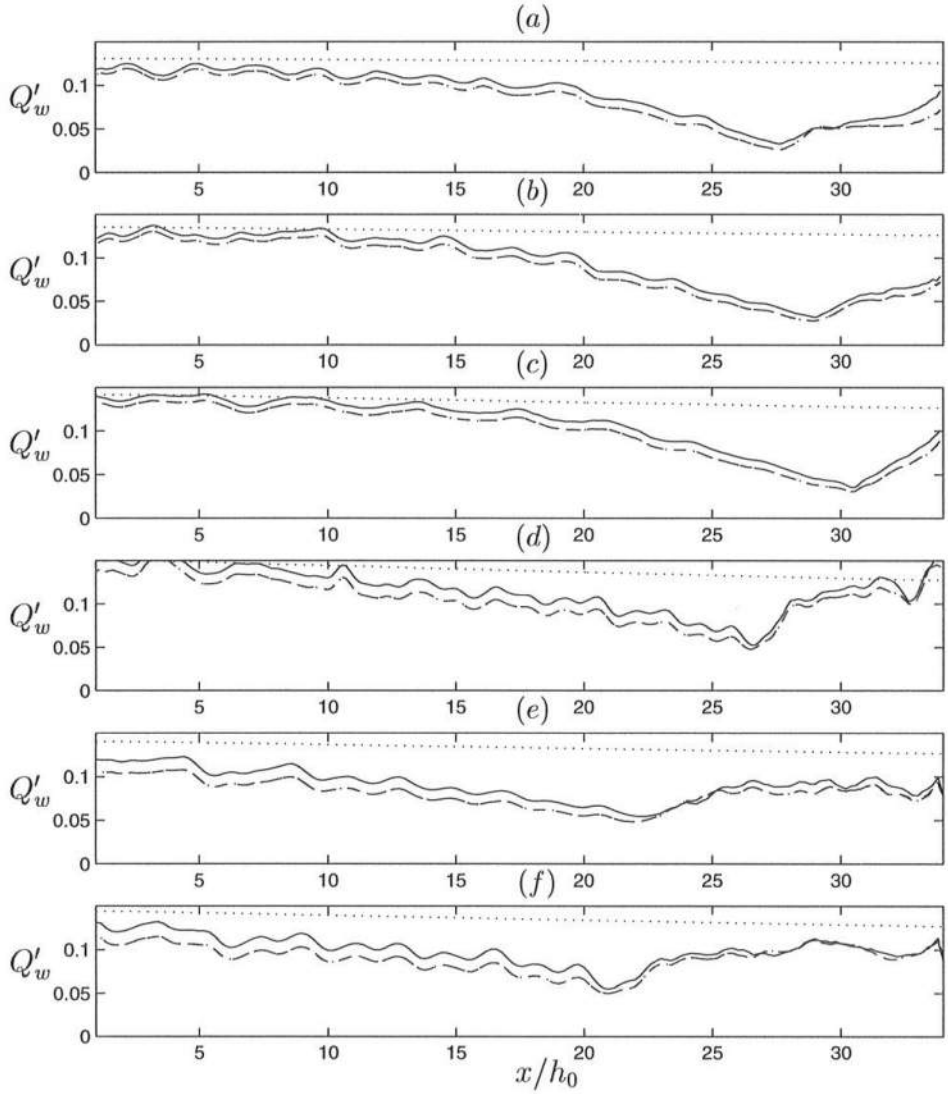

Figure 5.18: Computed non-dimensional wave mass flux (5.12) for 6 wave conditions: (a) wh031041 (table 5.2), (b) wh041041 (table 5.2), (c) wh051041 (table 5.2), (d) wh061071 (table 5.2), (e) Cox *et al.* (1995) and (f) Ting and Kirby (1994). Linear theory (· · · · ·), using (5.10) and (5.11a) (–·–·–), using (5.10) and (5.11b) (———) and using (5.10) and (5.11c) (– – –).

approximation retained, $p_D \simeq -\rho w^2$ where w is the vertical velocity. We define the non-dimensional radiation stress as

$$P \equiv \frac{S_{xx}}{\rho g H^2} = \frac{1}{gH^2}\overbrace{\int_{-h}^{\zeta}(u_w^2 - w^2)\,dz} + \frac{1}{2}\frac{\overbrace{(\zeta-\overline{\zeta})^2}}{H^2} \tag{5.15}$$

Utilizing the decomposition described in the previous subsection, and the fact that below the trough level, the average velocity in the oscillatory part of the motion due is zero, P can be expressed in terms of the total horizontal velocity as

$$P = \frac{1}{gH^2}\overbrace{\int_{-h}^{\zeta}(u^2 - w^2)\,dz} - \frac{2}{gH^2}\overbrace{\int_{\zeta_t}^{\zeta} u_w V\,dz} - \frac{1}{gH^2}\int_{-h}^{\overline{\zeta}} V^2\,dz + \frac{1}{2}\frac{\overbrace{(\zeta-\overline{\zeta})^2}}{H^2} \tag{5.16}$$

where ζ_t represents the trough level. To evaluate the second term which involves $u_w V$, we again choose V to be defined by one of (5.11a)-(5.11c), which gives

$$\begin{aligned} P = \frac{1}{gH^2}\left[\overbrace{\left(\frac{Q^2}{h+\zeta}\right)} + \widehat{\Delta M}\right] - \frac{1}{gH^2}\int_{-h}^{\overline{\zeta}} V^2\,dz + \frac{1}{2}\frac{\overbrace{(\zeta-\overline{\zeta})^2}}{H^2} \\ - 2\frac{V(\overline{\zeta})}{gH^2}\left[\overbrace{\int_{\zeta_t}^{\zeta} u\,dz} - V(\overline{\zeta})(\overline{\zeta}-\zeta_t)\right] - \frac{1}{gH^2}\overbrace{\int_{-h}^{\zeta} w^2\,dz} \end{aligned} \tag{5.17}$$

Figure 5.19 shows the cross-shore variation of the radiation stress, obtained using the model results for the four cases of Hansen and Svendsen (1979) (figures 5.18(a)-(d)), the wave conditions of Cox *et al.* (1995) (figure 5.18(e)) and that of Ting and Kirby (1994) (figure 5.18(f)). Linear long wave theory predicts a constant value of $P = 0.1875$ whereas the values obtained from the model varies. Over most of the domain, the value of P is significantly less than this value.

As the waves shoal, the crests become more and more peaked resulting in decreasing values of P. The lowest value of P is just before breaking in all cases. Once the waves start breaking, they become more triangular shaped, which results in increasing values of P. Though differing in details, this variation is in qualitative agreement with the results found by Svendsen and Putrevu (1993) from analysis of experimental data. It is also seen that the cross-shore variation of the radiation stress is similar to the mass flux variation.

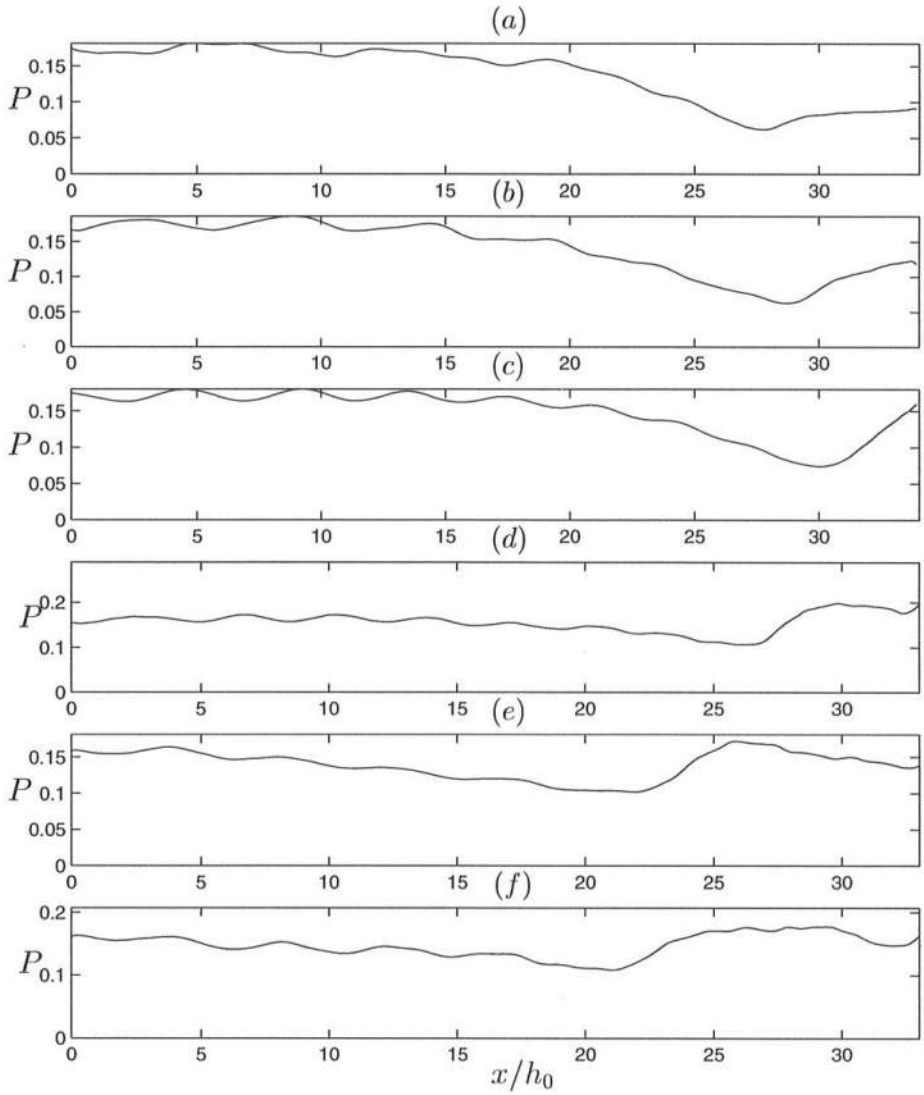

Figure 5.19: Computed non-dimensional wave radiation stress (5.17) for 6 wave conditions: (a) wh031041 (table 5.2), (b) wh041041 (table 5.2), (c) wh051041 (table 5.2), (d) wh061071 (table 5.2), (e) Cox *et al.* (1995) and (f) Ting and Kirby (1994).

We also notice that in the cross-shore variation of P which is expected to decrease monotonically towards the breaking point, there is an oscillatory component. The wave period of this oscillation is exactly one half the wave period of the actual wave. Closer inspection shows that this is because as the waves shoal, they start deviating from the permanent form solution to the Boussinesq equation for that particular water depth. Consequently, energy is transferred between the primary and the higher harmonics and in particular between the primary and the second harmonic components. This causes the wavy feature seen in the figure.

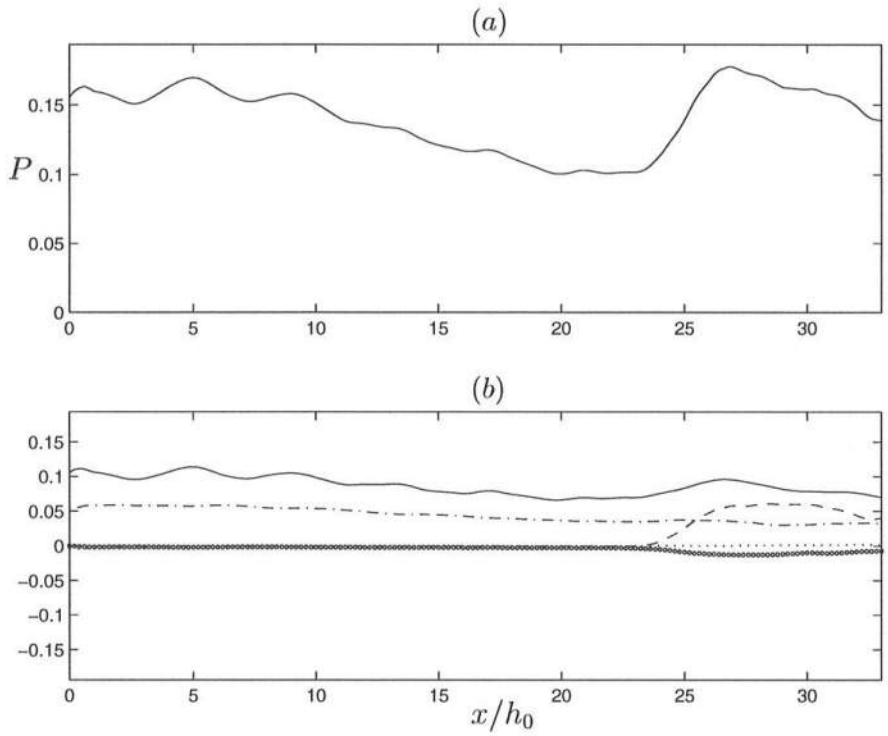

Figure 5.20: (a) Computed non-dimensional wave radiation stress (5.17) for Cox *et al.* (1995). (b) Contributions to P from $Q^2/(h+\zeta)$ term (———), $(\zeta - \overline{\zeta})^2$ term (–·–·–), ΔM (– – –), undertow (•) and the vertical velocity $(\cdots)$

Figure 5.20(a) shows the cross-shore variation of P in Cox *et al.* (1995) reproduced from figure 5.19(e). Figure 5.20(b) shows the contributions from the different terms in (5.17). We see that the contribution from the dynamic pressure

term ($\diamond$) is negligible everywhere in comparison to the other terms. The main contributions in the shoaling region are from the $Q^2/(h+\zeta)$ term (———) and the $(\zeta - \overline{\zeta})^2$ term (–·–·–). Inside the surf zone, the additional contribution comes mainly from the ΔM term (– – –). The contribution from the current contribution from the region between the wave trough and the mean water level is small and the contribution from the vertical velocity is almost zero.

5.4.3 Wave celerity.

The phase speed of a wave, defined as $c = \omega/k$ where ω is the angular frequency and k is the wave number, is difficult to calculate directly when the depth varies continuously in the direction of the wave propagation. However, if we assume a locally permanent form so that

$$\zeta(x,t) = \sum_{n=1}^{\infty} a_n e^{in(kx-\omega t)}$$

then, the local celerity is given by

$$c = -\frac{\partial\zeta/\partial t}{\partial\zeta/\partial x} = \frac{\partial Q/\partial x}{\partial\zeta/\partial x} \tag{5.18}$$

where Q is the volume flux. For each wave, this celerity obtained at the steepest part of the wave front which is defined as the phase speed of the wave or the wave celerity. This is also the definition used by Madsen *et al.* (1997).

Figure 5.21 shows the wave celerity computed using (5.18) for the six wave conditions mentioned in the previous sections. In the figure, the celerity is normalized by $\sqrt{gh}$ which is long wave phase speed. For all cases, at the offshore boundary, the speed of propagation is smaller than $\sqrt{gh}$. As the waves move into shallower water, the speed increases until the waves start to break. This maximum speed for all cases lie in the range 1.3-1.4$\sqrt{gh}$. In most cases, the speed starts to decrease once the wave breaks. For the first case (figure 5.21(a)), the celerity eventually decreases to a value close to $\sqrt{gh}$. For all other cases, the minimum celerity in the surf zone is about 1.2$\sqrt{gh}$.

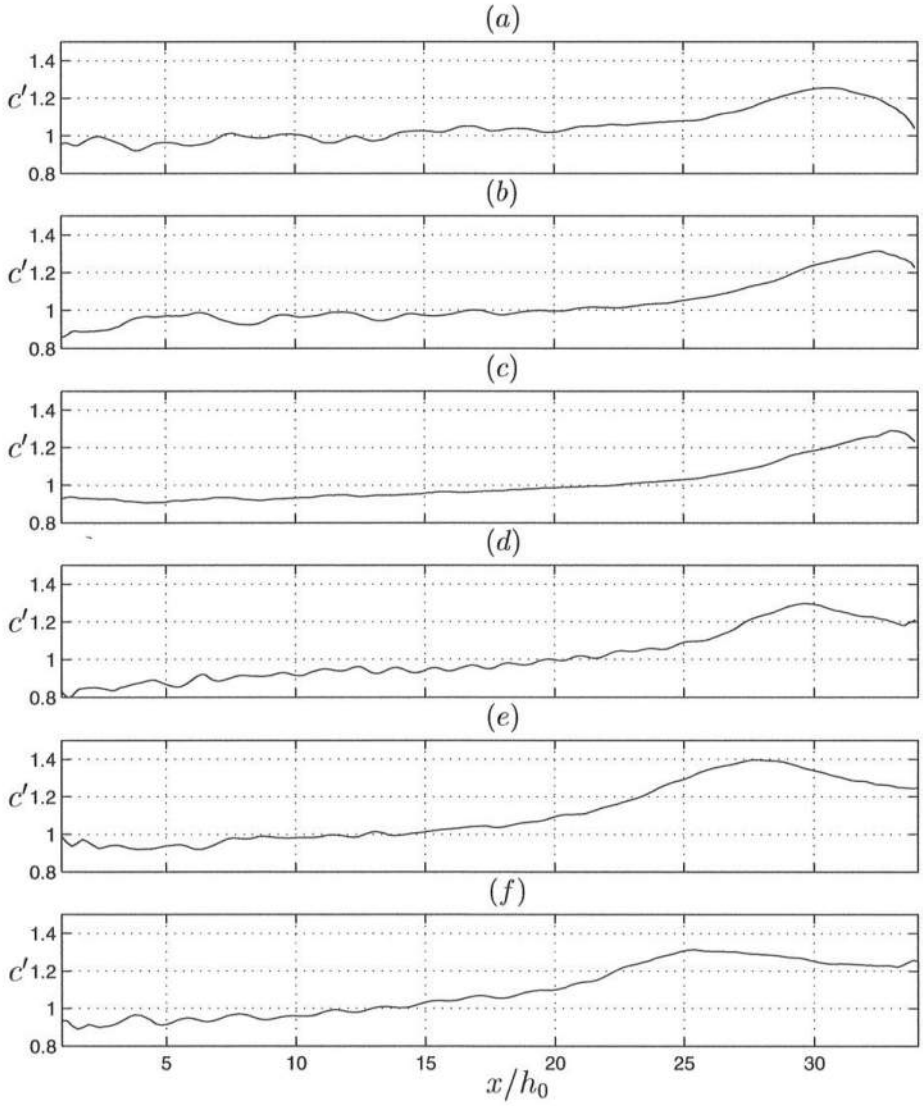

Figure 5.21: Computed non-dimensional phase speed $c/\sqrt{gh}$ of the waves for 6 wave conditions: (a) wh031041 (table 5.2), (b) wh041041 (table 5.2), (c) wh051041 (table 5.2), (d) wh061071 (table 5.2), (e) Cox *et al.* (1995) and (f) Ting and Kirby (1994).

Chapter 6

CONCLUSIONS.

A Boussinesq-type model, which is fully non-linear up to $O(\mu^2)$, has been developed to model spilling breakers in shallow water. Unlike other Boussinesq models, which use the potential flow assumption to describe the velocity field, the breaking model described here includes the vorticity that is generated when waves are breaking. Thus, the model can also describe the velocity field in the surf zone due to the short wave motion.

Following the approach of Svendsen *et al.* (1996), the model is derived from the depth-integrated momentum and continuity equations (Chapter 2). The vertical variation of the velocity is obtained from the equation for stream function, which allows the inclusion of the vorticity generated by breaking. This enables us to calculate the velocity field in the surf zone with greater accuracy. The benefit is that the wave-averaged quantities, such as the undertow, can be evaluated directly from the model results. The breaking terms are essentially corrections to the momentum balance. These correction terms come about due to the change in velocity profile once the waves start breaking. The change in the velocity profiles can in turn be attributed to the production of vorticity in the roller region of the breaking waves.

The vorticity, which appears as a third variable in addition to the water surface elevation and the velocity, is obtained from the solution to the vorticity transport equation (Chapter 3). An analytical solution to this equation is found by means of a series expansion. To model the waves inside the surf zone, the analogy between breaking waves and bores is used. The boundary conditions for the vorticity are deduced from measurements in hydraulic jumps. The jumps considered have Froude numbers that are similar to that in breaking waves. The boundary at which the vorticity is prescribed is the lower edge of the roller. The location of this

boundary is also obtained from the measurements in hydraulic jumps. A turbulent eddy viscosity, comparable in magnitude to that observed in the laboratory surf zone, is used for the diffusion/convection of the vorticity in the breaking waves.

A fourth-order ABM predictor-corrector scheme, similar to that used by Wei and Kirby (1995), is used to solve the governing equations numerically (Chapter 4). The spatial derivatives are obtained with enough accuracy that the magnitudes of the truncation errors that result from the finite difference method are smaller than the magnitudes of the terms in the equation. The model equations are rearranged so that the solutions for the velocity variable are obtained using a tridiagonal system of equations. This effectively increases the stability range of the model.

An absorbing-generating boundary condition is used at the offshore boundary. The method of characteristics is used to absorb the outgoing wave at the offshore boundary. The depth-averaged velocity corresponding to the permanent form solution of the weakly non-linear equation is prescribed at this boundary. At the shoreline, the present version of the model has a shelf with small water depth. A sponge layer is used to absorb the breaking waves in the region of this shelf.

The performance of the model for monochromatic wave situations is presented in Chapter 5. The model results are compared to laboratory data where possible. The solitary wave propagation and shoaling is compared to the results from solving the fully non-linear potential flow (FNPF) equations obtained using a boundary element method. It is seen that the model prediction of the wave shape and height is very good.

The vorticity field in breaking waves predicted by the model is also qualitatively in agreement with laboratory data. The model computations show that the vorticity generated in the roller region spreads downward and towards the back of the wave.

The comparison to experimental data for monochromatic wave shoaling and breaking show that the performance of the model in the surf zone is also very good. The model results for the wave height and set-up in the surf zone compare well with experimental data. The model is also found to predict the velocity field for breaking waves reasonably well. The undertow comparisons show that while the

present model predicts the undertow well, a breaking model based on potential flow does not. The correspondence between the magnitude of the eddy viscosity and the undertow was discussed.

The model results also show that use of linear theory to predict the wave averaged quantities, such as the mass flux and the radiation stress, gives larger magnitudes of these quantities. The computed radiation stress from the model is qualitatively similar to the radiation stress computed from measured data.

Although the present model gives very good predictions of the breaking wave characteristics, additional features can be implemented which could improve the model. The undertow predictions show that the bottom friction is important, especially in the shoaling region and in the outer surf zone. This would also necessitate the inclusion of the vorticity generated by the bottom boundary layer which may not be trivial.

Another area for enhancing the model is in the solution to the vorticity equation. As was indicated earlier, there is considerable uncertainty in the estimation of the eddy viscosity. However, measurements indicate that the eddy viscosity decreases monotonically (almost linearly) from the surface to the bottom. Analytical solutions to the vorticity equations can be obtained for such variations. However, these solutions are cumbersome to implement even for the lowest order problem. Therefore, it would be much more practical to employ a numerical solution technique in this case. As mentioned before, these methods would have to be more efficient than simple finite difference methods.

Modeling the shoreline by means of a moving boundary condition, to model the swash region and the run-up and run-down, would facilitate the study of such phenomena as long wave generation by regular and irregular wave groups. One possible problem in this scenario would be the modeling of bore-bore capture in the surf zone.

These are some of the features that may be included in the one-dimensional model. Further development of the model would involve extending the model to two dimensions to study long shore currents, rip current and other nearshore circulation patterns.

Appendix A

ALTERNATIVE DERIVATION OF THE STREAM FUNCTION ψ.

We have the equation for ψ in non-dimensional form (equation 2.26)

$$\mu^2\psi_{xx} + \psi_{zz} = \omega, \tag{A.1}$$

with the boundary conditions

$$\psi(-h) = 0, \tag{A.2}$$

$$\psi(\zeta) = \int_{-h}^{\delta\zeta} u\, dz. \tag{A.3}$$

Integrating (A.1) once from the bottom to an arbitrary location z in the water column

$$\psi_z = -\int_{-h}^{z} \mu^2\psi_{xx}\, dz + \int_{-h}^{z} \omega\, dz + \psi_z(-h). \tag{A.4}$$

Since $u = \partial\psi/\partial z$, (A.4) is

$$\psi_z = -\int_{-h}^{z} \mu^2\psi_{xx}\, dz + \int_{-h}^{z} \omega\, dz + u_0, \tag{A.5}$$

where u_0 is the velocity at $z = -h$. Integrating (A.5) again from the bottom to an arbitrary location z,

$$\psi = -\int_{-h}^{z}\int_{-h}^{z} \mu^2\psi_{xx}\, dz\, dz + \int_{-h}^{z}\int_{-h}^{z} \omega\, dz\, dz + u_0(z+h). \tag{A.6}$$

To the lowest order in μ^2, we have

$$\psi = \int_{-h}^{z}\int_{-h}^{z} \omega\, dz\, dz + u_0(z+h), \tag{A.7}$$

which gives

$$\psi_{xx} = \int_{-h}^{z} \int_{-h}^{z} \omega_{xx}\, dz\, dz + u_{0_{xx}}(z+h) + u_0 h_{xx} + 2u_{0_x} h_x, \tag{A.8}$$

where we have used the assumption that $\omega(-h) = 0$. Substituting (A.8) into (A.6) gives the expression for ψ

$$\begin{aligned}\psi =& u_0(z+h) - \frac{1}{6}\mu^2 u_{0_{xx}}(z+h)^3 + \int_{-h}^{z}\int_{-h}^{z} \omega\, dz\, dz \\ &- \frac{1}{2}\mu^2(z+h)^2\left(u_0 h_{xx} + 2u_{0_x} h_x\right) - \mu^2 \int_{-h}^{z}\int_{-h}^{z}\int_{-h}^{z}\int_{-h}^{z} \omega_{xx}\, dz\, dz\, dz\, dz,\end{aligned} \tag{A.9}$$

which is exactly the same expression as (2.34).

Thus, equation (2.34) can be derived without assuming (2.27). As we know from classical Boussinesq theory, (2.27a) is not necessary; it is a consequence of $\mu^2 \ll 1$. However, for pedagogical reasons it makes sense to assume (2.27b) and then show that we really need the entire expansion for ω.

Appendix B

EXPRESSIONS FOR THE BREAKING TERMS.

The solution to the vorticity equation is

$$\begin{aligned}\omega =&\sigma\omega_s + \omega^{(1)} + \omega^{(2)} \\ =&\sigma\omega_s + \sum_{n=1}^{\infty} G_n^{(1)} \sin n\pi\sigma + \sum_{n=1}^{\infty} G_n^{(2)} \sin n\pi\sigma,\end{aligned} \tag{B.1}$$

with

$$G_n^{(1)}(t) = (-1)^n \frac{2}{n\pi} \int_0^t \frac{\partial \omega_s}{\partial t} e^{n^2\pi^2\kappa(\tau - t)}\, d\tau, \tag{B.2}$$

$$G_n^{(2)}(t) = \int_0^t F_n^{(2)} e^{n^2\pi^2\kappa(\tau - t)}\, d\tau, \tag{B.3}$$

$$F_n^{(2)}(t) = 2\int_0^1 F^{(2)} \sin n\pi\sigma\, d\sigma, \tag{B.4}$$

where $G_n^{(1)}(t)$'s are the coefficients of the solution to the $O(\delta^0)$ problem and $G_n^{(2)}(t)$'s are the coefficients of the solution to the $O(\delta)$ problem. The expression for $F^{(2)}$ is

$$\begin{aligned}F^{(2)} =&2\kappa\frac{\zeta_e}{h}\frac{\partial^2\omega^{(1)}}{\partial\sigma^2} + 2\omega_s\frac{\sigma}{h}\frac{\partial\zeta_e}{\partial t} + \frac{\sigma}{h}\frac{\partial\zeta_e}{\partial t}\frac{\partial\omega^{(1)}}{\partial\sigma} - u^{(1)}\frac{\partial\omega^{(1)}}{\partial\sigma} - u^{(1)}\sigma\frac{\partial\omega_s}{\partial x} \\ &- \frac{w^{(1)}}{h}\left(\frac{\partial\omega^{(1)}}{\partial\sigma} + \omega_s\right).\end{aligned} \tag{B.5}$$

First, we have to evaluate $F_n^{(2)}$ based on the values of $\omega^{(1)}$, $u^{(1)}$ and $w^{(1)}$ obtained using $G_n^{(1)}(t)$. Here, we make the assumption that the roller thickness is much smaller than the wave height. Hence, in the terms where the rotational velocity is integrated over the depth, the contribution from this region is negligible in comparison to the contribution from the region between the bottom of the roller and the sea bed. In the convective momentum term (ΔM), which is also the sole

$O(\delta)$ term whereas the rest of the breaking terms are $O(\mu^2)$, the integrand is the square of the velocity. Here the contribution from the roller region is included by approximating the vorticity in the roller region by a linear polynomial which has a value of ω_s at the lower edge of the roller and zero at the surface.

The expressions for $u^{(1)}$ and $w^{(1)}$ are approximated as

$$u_r^{(1)} = \int_{-h}^{\delta\zeta} \omega \, dz, \tag{B.6}$$

$$\begin{aligned} u^{(1)} &= \overline{u}^{(1)} + \left(u_r^{(1)} - \overline{u}_r{}^{(1)}\right) + O(\mu^2) \\ &= \overline{u}^{(1)} + \left[\omega_s\left(\frac{\sigma^2}{2} - \frac{1}{6}\right) - \sum_{n=1}^{\infty} \frac{G_n^{(1)}}{n\pi}\cos n\pi\sigma\right] + O(\mu^2), \end{aligned} \tag{B.7}$$

$$\begin{aligned} w^{(1)} &= -\frac{\partial}{\partial x}\int_{-h}^{\delta\zeta} u^{(1)}\, dz \\ &= -h\overline{u}_x\sigma - h^2\sum_{n=1}^{\infty}\frac{\partial G_n^{(1)}}{\partial x}\frac{\cos n\pi\sigma}{n\pi} + O(\delta, h_x, \mu^2). \end{aligned} \tag{B.8}$$

Substituting the solution to $\omega^{(1)}$ from (B.1) and (B.7)-(B.8) in the expression for $F^{(2)}$ given by (B.5), the Fourier coefficients $F_n^{(2)}$ are calculated using (B.4). The result, obtained after some algebra is

$$\begin{aligned} F_n^{(2)} = &-2n^2\pi^2\kappa\frac{\zeta_e}{h^3}G_n^{(1)} - \frac{1}{2h}\frac{\partial\zeta_e}{\partial t}G_n^{(1)} - 4\frac{\omega_s}{h}\frac{\partial\zeta_e}{\partial t}\frac{\cos n\pi}{n\pi} - \overline{u}\frac{\partial G_n^{(1)}}{\partial x} - \frac{3h\omega_s}{4n^2\pi^2}\frac{\partial G_n^{(1)}}{\partial x} \\ &+ 2\overline{u}\frac{\partial\omega_s}{\partial x}\frac{\cos n\pi}{n\pi} - h\omega_s\frac{\partial\omega_s}{\partial x}\frac{\cos n\pi}{n\pi}\left(\frac{4}{n^2\pi^2} - \frac{2}{3}\right) - \frac{3}{8}\frac{hG_n^{(1)}}{n^2\pi^2}\frac{\partial\omega_s}{\partial x} \\ &- \frac{G_n^{(1)}}{2n\pi}\frac{\partial\overline{u}}{\partial x} - 2\omega_s\frac{\cos n\pi}{n\pi}\frac{\partial\overline{u}}{\partial x} - \left(\frac{2}{h}\frac{\partial\zeta_e}{\partial t} + 2\frac{\partial\overline{u}}{\partial x}\right)\sum_{\substack{m=1\\m\neq n}}^{\infty} nmG_m^{(1)}\frac{(-1)^{n+m}}{n^2-m^2} \\ &- 4h\omega_s\sum_{\substack{m=1\\m\neq n}}^{\infty}\frac{\partial G_m^{(1)}}{\partial x}\frac{nm(-1)^{n+m}}{(n^2-m^2)^2} - 2h\frac{\partial\omega_s}{\partial x}\sum_{\substack{m=1\\m\neq n}}^{\infty}\frac{G_m^{(1)}}{m\pi}\frac{n(-1)^{n+m}}{(n^2-m^2)\pi^2} \\ &+ 2h\frac{\partial\omega_s}{\partial x}\sum_{\substack{m=1\\m\neq n}}^{\infty} nmG_m^{(1)}\frac{(-1)^{n+m}(3m^2+n^2)}{(n^2-m^2)^3\pi^2}. \end{aligned} \tag{B.9}$$

Now the breaking terms can be evaluated using (B.1), which can be written in a simpler form using the relation

$$\sigma\omega_s = \sum_{n=1}^{\infty} G_n^{(0)} \sin n\pi\sigma; \qquad G_n^{(0)} = (-1)^n \frac{2\omega_s}{n\pi}, \tag{B.10}$$

which gives

$$\omega = \sum_{n=1}^{\infty} G_n \sin n\pi\sigma, \tag{B.11}$$

where $G_n = G_n^{(0)} + G_n^{(1)} + G_n^{(2)}$.

B.1 Expressions for the $O(\delta)$ breaking term.

The term ΔM in (2.72) is the only breaking term that is $O(\delta)$. In the evaluation of this term, the contribution from the roller region is also included. The expression for ΔM is written as

$$\begin{aligned} \Delta M &= \int_{-h}^{\zeta_e} \left(u_r^2 - \overline{u}_r^2\right)\, dz \\ &= \int_{-h}^{\zeta_e} u_r^2\, dz + \int_{\zeta_e}^{\zeta} u_r^2\, dz - \frac{(Q_r + \Delta Q_r)^2}{h+\zeta}, \end{aligned} \tag{B.12}$$

where

$$Q_r \equiv \int_{-h}^{\zeta_e} u_r\, dz \qquad \text{and} \qquad \Delta Q_r = \int_{\zeta_e}^{\zeta} u_r\, dz. \tag{B.13}$$

Although it is known from the estimates in the hydraulic jump measurements that the variation of ω in the roller region is closer to a quadratic variation, to simplify the problem, a linear approximation is assumed for ω in this region. This linear variation also captures most of the contributions from this region. Thus, the variation of vorticity is given by

$$\omega = \begin{cases} \displaystyle\sum_{n=1}^{\infty} G_n \sin n\pi\sigma & z < \zeta_e \\ \\ \omega_s \left(\dfrac{\zeta - z}{\zeta - \zeta_e}\right) & \zeta_e < z < \zeta \end{cases} \tag{B.14}$$

which gives

$$u_r = \begin{cases} \displaystyle\int_{-h}^{\delta\zeta} \omega \, dz & z < \zeta_e \\ \\ \displaystyle u_{rb} + \int_{\zeta_e}^{\zeta} \omega \, dz & \zeta_e < z < \zeta \end{cases} \tag{B.15}$$

where u_{rb} is the rotational velocity at the lower edge of the roller. This gives the expressions

$$\int_{-h}^{\zeta_e} u_r^2 \, dz = (h+\zeta_e)^3 \left[\left(\sum_{n=1}^{\infty} \frac{G_n}{n\pi} \right)^2 + \sum_{n=1}^{\infty} \frac{G_n}{2n^2\pi^2} \right], \tag{B.16}$$

$$\int_{\zeta_e}^{\zeta} u_r^2 \, dz = u_{rb}^2(\zeta - \zeta_e) + \frac{2}{3} u_{rb}\omega_s(\zeta - \zeta_e)^2 + \frac{2}{15}\omega_s^2(\zeta - \zeta_e)^3, \tag{B.17}$$

$$Q_r = (h+\zeta_e)^2 \sum_{n=1}^{\infty} \frac{G_n}{n\pi}, \tag{B.18}$$

$$\Delta Q_r = u_{rb}(\zeta - \zeta_e) + \frac{\omega_s}{3}(\zeta - \zeta_e)^2, \tag{B.19}$$

which are then used to obtain ΔM from (B.12).

B.2 Expressions for the $O(\mu^2)$ breaking terms.

The breaking terms that are $O(\mu^2)$ in (2.72) are ΔM_1, ΔP, D_w and D_{uw} which are the higher-order correction to the convective momentum term, the effect of the vertical acceleration, the vertical motion of the fluid and the net shear stress due to the mean flow respectively. The integral expressions for these breaking terms are given by (2.59), (2.2.2), (2.66), and (2.69) respectively. The contributions from the roller region in the expressions for these terms are assumed small. Therefore, the expression for u_r can be approximated as

$$\overline{u}_r = \frac{Q_r}{h+\zeta_e} = (h+\zeta_e) \sum_{n=1}^{\infty} \frac{G_n}{n\pi}, \tag{B.20}$$

which gives

$$u_r - \overline{u}_r = -(h+\zeta_e) \sum_{n=1}^{\infty} \frac{G_n}{n\pi} \cos n\pi\sigma. \tag{B.21}$$

This expression for $u_r - \overline{u}_r$ is used to evaluate the expression for the breaking terms that are $O(\mu^2)$. Thus,

$$\begin{aligned}
\Delta P &= -\int_{-h}^{\zeta}\int_{z}^{\zeta}\int_{-h}^{z}(u_r-\overline{u}_r)\,dz\,dz\,dz \\
&\simeq -\int_{-h}^{\zeta_e}\int_{z}^{\zeta_e}\int_{-h}^{z}(u_r-\overline{u}_r)\,dz\,dz\,dz \\
&= -(h+\zeta_e)^3\int_0^1\int_\sigma^1\int_0^\sigma(u_r-\overline{u}_r)\,d\sigma\,d\sigma\,d\sigma \\
&= -(h+\zeta_e)^4\sum_{n=1}^{\infty}\frac{G_n}{n^3\pi^3}\cos n\pi, \qquad \text{(B.22)}
\end{aligned}$$

$$\begin{aligned}
\Delta M_1 &= -(\overline{u}_p)_{xx}\left[\int_{-h}^{\zeta}(2hz+z^2)(u_r-\overline{u}_r)\,dz\right] \\
&\simeq -(\overline{u}_p)_{xx}\left[\int_{-h}^{\zeta_e}(2hz+z^2)(u_r-\overline{u}_r)\,dz\right] \\
&= -2(h+\zeta_e)^2(\overline{u}_p)_{xx}\sum_{n=1}^{\infty}\frac{G_n}{n^3\pi^3}\cos n\pi, \qquad \text{(B.23)}
\end{aligned}$$

$$\begin{aligned}
D_w &= \frac{\partial}{\partial x}\int_{-h}^{\zeta}\left[\left(\frac{\partial}{\partial x}\int_{-h}^{z}(u_r-\overline{u}_r)\,dz\right)\frac{\partial}{\partial x}\int_{-h}^{z}(\overline{u}+u_r-\overline{u}_r)\,dz\right]dz \\
&\simeq \frac{\partial}{\partial x}\int_{-h}^{\zeta_e}\left[\left(\frac{\partial}{\partial x}\int_{-h}^{z}(u_r-\overline{u}_r)\,dz\right)\frac{\partial}{\partial x}\int_{-h}^{z}(\overline{u}+u_r-\overline{u}_r)\,dz\right]dz \\
&= (h+\zeta_e)^3(\zeta_{ex})^2\left[\sum_{n=1}^{\infty}\frac{G_n^2}{n^4\pi^4}\left(\frac{13}{4}+\frac{n^2\pi^2}{6}\right)\right. \\
&\qquad \left.\sum_{n=1}^{\infty}\sum_{\substack{m=1\\m\neq n}}^{\infty}2\frac{G_nG_m}{nm\pi^2}\left(\frac{3n^2-m^2}{(n^2-m^2)^2\pi^2}\right)\cos(n+m)\pi\right] \\
&\qquad +(h+\zeta_e)^4\zeta_{ex}\sum_{n=1}^{\infty}\left[\frac{5}{2}\frac{G_nG_{n_x}}{n^4\pi^4}+\sum_{\substack{m=1\\m\neq n}}^{\infty}\frac{G_{n_x}G_m}{nm\pi^2}\left(\frac{\cos(n+m)\pi}{(n^2-m^2)^2\pi^2}\right)\right]
\end{aligned}$$

$$2\overline{u}_x \frac{\partial}{\partial x}\left[(h+\zeta_e)^4 \sum_{n=1}^{\infty} \frac{G_n}{n^3\pi^3}\cos n\pi\right] + (h+\zeta_e)^5 \sum_{n=1}^{\infty} \frac{G_{n_x}^2}{2n^4\pi^4}, \tag{B.24}$$

(B.25)

$$\begin{aligned}
D_{uw} &= \int_{-h}^{\zeta} \frac{\partial^2}{\partial x^2} \int_{-h}^{\zeta} \left[(u_r - \overline{u}_r)\frac{\partial}{\partial x}\int_{-h}^{z} \overline{u}dz + (\overline{u} + u_r - \overline{u}_r)\frac{\partial}{\partial x}\int_{-h}^{z}(u_r - \overline{u}_r)dz\right] dzdz \\
&\simeq \int_{-h}^{\zeta_e} \frac{\partial^2}{\partial x^2} \int_{-h}^{\zeta_e} \left[(u_r - \overline{u}_r)\frac{\partial}{\partial x}\int_{-h}^{z} \overline{u}dz + (\overline{u} + u_r - \overline{u}_r)\frac{\partial}{\partial x}\int_{-h}^{z}(u_r - \overline{u}_r)dz\right] dzdz \\
&= -(h+\zeta_e)^4 \overline{u}_x \sum_{n=1}^{\infty} 2\frac{G_n}{n^3\pi^3}\cos n\pi + \overline{u}\frac{\partial}{\partial x}\left[(h+\zeta_e)^4 \sum_{n=1}^{\infty} \frac{G_n}{n^3\pi^3}\cos n\pi\right] \\
&\quad - (h+\zeta_e)^5 \sum_{n=1}^{\infty}\left[\frac{G_n G_{n_x}}{4n^4\pi^4} + \sum_{\substack{m=1 \\ m\neq n}}^{\infty} \frac{G_n G_{m_x}}{m^2\pi^4}\left(\frac{\cos(n+m)\pi}{n^2-m^2}\right)\right] \\
&\quad - (h+\zeta_e)^4 \zeta_{e_x} \sum_{n=1}^{\infty}\left[\frac{G_n^2}{n^4\pi^4}\left(\frac{n^2\pi^2}{6} + \frac{3}{4}\right)\right. \\
&\qquad \left. + \sum_{\substack{m=1 \\ m\neq n}}^{\infty} \frac{2G_n G_m}{m^2\pi^4}\left(\frac{n^2 - m^2 + n^2m^2 + m^4}{(n^2-m^2)^2}\right)\cos(n+m)\pi\right].
\end{aligned} \tag{B.26}$$

Appendix C

SPECTRAL SOLUTION TO WEAKLY NON-LINEAR EQUATIONS.

The permanent form solution to the weakly non-linear $\zeta - Q$ version of the Boussinesq equations was shown in Yu (1996). Here, the same approach is used to derive the permanent form solution to the weakly non-linear $\zeta - \overline{u}$ equations for a horizontal bottom. The equations are

$$\zeta_t + h\overline{u}_x + (\zeta\overline{u})_x = 0, \tag{C.1}$$

$$\overline{u}_t + \overline{u}\overline{u}_x + g\zeta_x + \left(B - \frac{1}{3}\right) h^2 \overline{u}_{xxt} + Bgh^3\zeta_{xxx} = O(\delta\mu^2). \tag{C.2}$$

The water surface elevation ζ and the velocity $\overline{u}$ can be represented by a Fourier sum

$$\zeta = \sum_{n=1}^{N} \frac{a_n}{2} e^{in\theta} + \star, \tag{C.3}$$

$$\overline{u} = \sum_{n=1}^{N} \frac{b_n}{2} e^{in\theta} + \star, \tag{C.4}$$

where $\theta = kx - \sigma t$, k is the wave number, σ is the angular frequency, $i = \sqrt{-1}$ and $\star$ represents the complex conjugates. The idea is to obtain a solution to (C.1) and (C.2) such that each Fourier component of the solution travels at the same phase speed. The derivatives of (C.3) and (C.4) that appear in (C.1) and (C.2) become

$$\zeta_t = \sum_{n=1}^{N} -in\sigma \frac{a_n}{2} e^{in\theta} + \star, \tag{C.5a}$$

$$\zeta_x = \sum_{n=1}^{N} ink \frac{a_n}{2} e^{in\theta} + \star, \tag{C.5b}$$

$$\zeta_{xxx} = \sum_{n=1}^{N} -in^3k^3\frac{a_n}{2}e^{in\theta} + \star, \tag{C.5c}$$

$$\overline{u}_t = \sum_{n=1}^{N} -in\sigma\frac{b_n}{2}e^{in\theta} + \star, \tag{C.5d}$$

$$\overline{u}_x = \sum_{n=1}^{N} ink\frac{b_n}{2}e^{in\theta} + \star, \tag{C.5e}$$

$$\overline{u}_{xxt} = \sum_{n=1}^{N} in^3k^2\sigma\frac{b_n}{2}e^{in\theta} + \star. \tag{C.5f}$$

The non-linear terms become

$$\begin{aligned}\zeta\overline{u} &= \left(\sum_{n=1}^{N}\frac{a_n}{2}e^{in\theta} + \star\right)\cdot\left(\sum_{n=1}^{N}\frac{b_n}{2}e^{in\theta} + \star\right) \\ &= \sum_{n=1}^{N}\frac{1}{2}a_nb_n + \frac{1}{4}\sum_{n=1}^{N}\left[\sum_{l=1}^{n}a_lb_{n-l} + \sum_{l=n+1}^{N}\left(a_lb_{l-n} + b_la_{l-n}\right)\right]e^{in\theta} + \star,\end{aligned} \tag{C.5g}$$

$$\begin{aligned}\overline{u}^2 &= \left(\sum_{n=1}^{N}\frac{b_n}{2}e^{in\theta} + \star\right)\cdot\left(\sum_{n=1}^{N}\frac{b_n}{2}e^{in\theta} + \star\right) \\ &= \sum_{n=1}^{N}\left(\sum_{l=1}^{n}\frac{1}{4}b_lb_{n-l} + \sum_{l=n+1}^{N}\frac{1}{2}b_lb_{l-n}\right)e^{in\theta} + \star.\end{aligned} \tag{C.5h}$$

Substituting (C.5) into (C.1) gives

$$\sum_{n=1}^{N}\left(-\sigma a_n + khb_n + \frac{k}{2}\left[\sum_{l=1}^{n}a_lb_{n-l} + \sum_{l=n+1}^{N}\left(a_lb_{l-n} + b_la_{l-n}\right)\right]\right)e^{in\theta} + \star = 0. \tag{C.6}$$

This equation has to be valid for each n, so that

$$-\sigma a_n + khb_n + \frac{k}{2}\left[\sum_{l=1}^{n}a_lb_{n-l} + \sum_{l=n+1}^{N}\left(a_lb_{l-n} + b_la_{l-n}\right)\right] = 0, \tag{C.7}$$

for $n = 1, 2, \cdots, N$. Similarly, substituting (C.5) into (C.2) gives

$$\begin{aligned}-\sigma b_n + k\sum_{l=1}^{n}\frac{1}{4}b_lb_{n-l} + \frac{k}{2}\sum_{l=n+1}^{N}b_lb_{l-n} + gka_n \\ + \left(B - \frac{1}{3}\right)h^2n^2k^2\sigma b_n - Bgh^3n^2k^3a_n = 0,\end{aligned} \tag{C.8}$$

for $n = 1, 2, \cdots, N$. Finally, we have the wave height

$$H = \zeta|_{\theta=0} - \zeta|_{\theta=\pi} = \sum_{n=1}^{N} a_n \left(1 - \cos n\pi\right). \tag{C.9}$$

Equations (C.7), (C.8) and (C.9) form a set of $2N+1$ equations in the $2N+1$ unknowns $(k, a_1, a_2, \cdots, a_N, b_1, b_2, \cdots, b_N)$. Thus, with the wave height and wave period known, these equations are solved to give the Fourier amplitudes and the wave number. The set of equations is a non-linear algebraic set of equations and is solved using a Newton-Raphson iteration method (Press *et al.* 1992). The solutions for two different cases are shown in figure C.1.

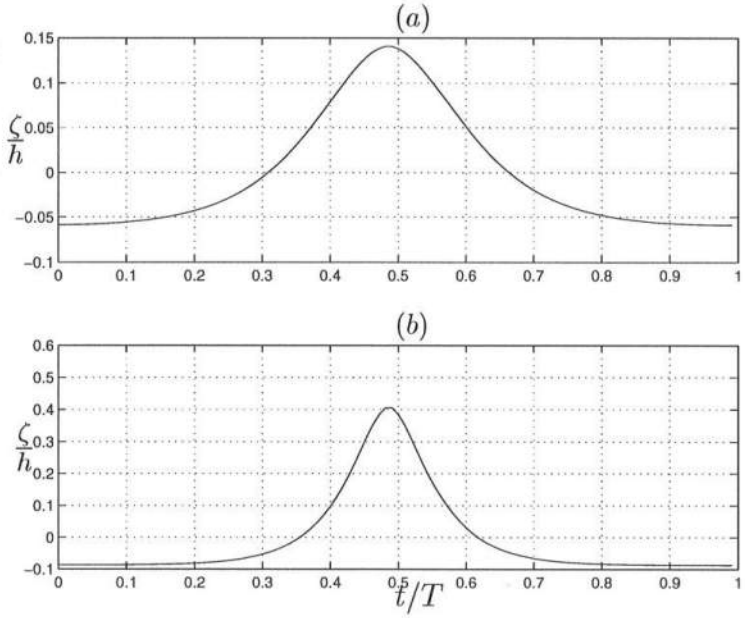

Figure C.1: Permanent form solutions to the weakly non-linear $\zeta - \overline{u}$ equations. (a) $\delta/h = 0.2$, $\mu^2 = 0.2$ (b) $\delta/h = 0.5$, $\mu^2 = 0.14$.

Bibliography

Abbot, M. B., A. Damsgaard, and G. S. Rodenhuis (1973). System 21, Jupiter, a design system for two-dimensional nearly horizontal flows. *J. Hydraulic Res. 11*, pp. 1–28.

Airy, G. B. (1945). Tides and waves. *Encycl. Metrop., Section VI.*

Anderson, D. A., J. C. Tannehill, and R. H. Pletcher (1984). *Computational fluid mechanics and heat transfer.* New York, USA: Hemisphere Publishing Corp.

Bakunin, J. (1995). Experimental study of hydraulic jumps in low Froude number range. Master's thesis, Center for Applied Coastal Research, University of Delaware, Newark, DE19716.

Banner, M. L. and O. M. Phillips (1974). On the incipient breaking of small scale waves. *J. Fluid Mech. 65*(4), pp. 647–656.

Battjes, J. and T. Sakai (1981). Velocity field in a steady breaker. *J. Fluid Mech. 111*, pp. 421–437.

Battjes, J. A. (1974). Surf similarity. *Proc. of 14th ICCE*, ASCE, pp. 466–480.

Battjes, J. A. (1988). Surf-zone dynamics. *Ann. Rev. Fluid Mech. 20*, pp. 257–293.

Benjamin, T. B. and M. J. Lighthill (1954). On cnoidal waves and bores. *Proc. Roy. Soc. Lond., Series A 244*, pp. 448–460.

Boussinesq, J. (1872). Theorie des ondes et des remous qui se propagent le long d'un canal rectangulaire horizontal. *en communiquant au liquide contenu dans ce canal des vitesses sensiblement pareilles de la surface au fond. Journal Math. Pures et Appl. 2nd series 17*, pp. 55–108.

Brocchini, M., M. Drago, and L. Iovenitti (1992). The modelling of short waves in shallow waters. Comparison of numerical models based on Boussinesq and Serre equations. *Proc. of 23rd ICCE*, ASCE, pp. 76–88.

Brocchini, M. and D. H. Peregrine (1996). Integral flow properties of the swash zone and averaging. *J. Fluid Mech. 317*, pp. 241–273.

Brocchini, M. and D. H. Peregrine (1998). The modelling of a spilling breaker: Strong turbulence at a free surface. *Proc. of 26th ICCE*, In press.

Chen, Q., P. A. Madsen, H. A. Schäffer, and D. R. Basco (1998). Wave-current interaction based on an enhanced Boussinesq-type approach. *Coastal Engng. 33*, pp. 11–40.

Cox, D. T., N. Kobayashi, and D. L. Kriebel (1994). Numerical model verification using Supertank data in surf and swash zone. *Coastal Dynamics '94*, ASCE, pp. 248–262. ASCE.

Cox, D. T., N. Kobayashi, and A. Okayasu (1995). Experimental and numerical modeling of surf zone hydrodynamics. Technical Report CACR-95-07, Center for Applied Coastal Research, University of Delaware.

Dean, R. G. and R. A. Dalrymple (1991). *Water wave mechanics for engineers and scientists* (2nd ed.). World Scientific.

Deigaard, R. (1989). Mathematical modelling of waves in the surf zone. Prog. Rep. 69, ISVA, Technical University, Lyngby. pp 47-59.

Deigaard, R. and J. Fredsoe (1989). Shear stress distribution in dissipative water waves. *Coastal Engng. 13*, pp. 357–378.

Duncan, J. H. (1981). An experimental investigation of wave breaking produced by a towed hydrofoil. *Proc. of Roy. Soc. of London, Series A 377*, pp. 331–348.

Duncan, J. H., H. Qiao, V. Philomin, and A. Wenz (1999). Gentle spilling breakers: crest profile evolution. *J. Fluid Mech. 379*, pp. 191–222.

Galvin, C. J. (1968). Breaker type classification on three laboratory beaches. *J. Geophysical Res. 73*(12), pp. 3651–3659.

Gobbi, M. F., J. T. Kirby, and G. Wei (1999). A fully nonlinear Boussinesq model for surface waves. II. Extension to $O(kh)^4$. *J. Fluid Mech.*, In press.

Grilli, S. T., R. Subramanya, I. A. Svendsen, and J. Veeramony (1994). Shoaling of solitary waves on plane beaches. *ASCE J. Waterway, Port, Coastal and Ocean Engng. 120*(6), pp. 609–628.

Hamm, L., P. A. Madsen, and D. H. Peregrine (1993). Wave transformation in the nearshore zone: a review. *Coastal Engng. 21*, pp. 5–39.

Hansen, J. B. and I. A. Svendsen (1979). Regular Waves in Shoaling Water: Experimental Data. Technical report, ISVA Series Paper 21.

Hibberd, S. and D. H. Peregrine (1979). Surf and run-up on a beach: A uniform bore. *J. Fluid Mech. 95*(2), pp. 323–345.

Hornung, H. G., C. Willert, and S. Turner (1995). The flow field of a hydraulic jump. *J. Fluid Mech. 287*, pp. 299–316.

Iribarren, C. R. and C. Nogales (1949). Protection des Ports. Section II, Comm. 4, XVIIth Int. Nav. Congress, Lisbon.

Israeli, M. and S. A. Orszag (1981). Approximation of radiation boundary conditions. *J. Comp. Phys. 41*, pp. 115–13.

Karambas, T. K. and C. Koutitas (1992). A breaking wave propagation model based on the Boussinesq equations. *Coastal Engng. 18*, pp. 1–19.

Karambas, T. V., Y. Krestenitis, and C. Koutatis (1990). A numerical solution of Boussinesq equations in the inshore zone. *Hydrosoft 3*(1), pp. 34–37.

Kennedy, A. B., Q. Chen, J. T. Kirby, and R. A. Dalrymple (1999). Boussinesq modeling of wave transformation, breaking and run-up. I: One dimension. Submitted to the *ASCE J. Waterway, Port, Coastal and Ocean Engng.*

Kirby, J. T. (1997). Nonlinear, dispersive long waves in water of variable depth. J. N. Hunt (Ed.), *Advances in Fluid Mech.*, Volume 10, pp. 55–125. Computational Mechanics Publications.

Kirby, J. T., J. Bakunin, and P. Huq (1995). Turbulence measurements in low Froude number hydraulic jumps. *Proc. 10th Engng. Mech. Conf.*

Kobayashi, N., G. S. De Silva, and K. D. Watson (1989). Wave transformation and swash oscillation on gentle and steep slopes. *J. Geophysical Res. 94*(6), pp. 951–966.

Kobayashi, N., A. K. Otta, and I. Roy (1987). Wave reflection and run-up on rough slopes. *ASCE J. Waterway, Port, Coastal and Ocean Engng. 113*(3), pp. 282–298.

Kofler, M. (1997). *MAPLE: An introduction and reference.* New York, USA: Addison-Wesley Longman Inc.

Larsen, J. and H. Dancy (1983). Open boundaries in short-wave simulations – A new approach. *Coastal Engng. 7*, pp. 285–297.

Lin, J. C. and D. Rockwell (1994). Instantaneous structure of a breaking wave. *Phys. Fluids 6(9)*, pp. 2877–2879.

Lin, J. C. and D. Rockwell (1995). Evolution of a quasi-steady breaking wave. *J. Fluid Mech. 111*, pp. 29–44.

Lin, P. and P. L. F. Liu (1998a). A numerical study of breaking waves in the surf zone. *J. Fluid Mech. 359*, pp. 239–264.

Lin, P. and P. L. F. Liu (1998b). Turbulence transport, vorticity dynamics, and solute mixing under plunging breaking waves in surf zone. *J. Geophysical Res. 103*, pp. 15677–15694.

Madsen, P. A., R. Murray, and O. R. Sørensen (1991). A new form of Boussinesq equations with improved dispersion characteristics. *Coastal Engng. 15*, pp. 371–388.

Madsen, P. A. and H. A. Schäffer (1998a). Higher order Boussinesq-type equations - derivation and analysis. *Phil. Trans. R. Soc. Lond., Series A, 356*, pp. 3123–3184.

Madsen, P. A. and H. A. Schäffer (1998b). A review of Boussinesq-type equations for gravity waves. P. L.-F. Liu (Ed.), *Advances in Coastal and Ocean Engng.*, Volume 5, pp. 90. World Scientific, Singapore.

Madsen, P. A. and O. R. Sørensen (1993). Bound waves and triad interactions in shallow water. *Ocean Engng. 20*, pp. 359–388.

Madsen, P. A., O. R. Sørensen, and H. A. Schäffer (1997). Surf zone dynamics simulated by a Boussinesq type model. Part I. Model description and cross-shore motion of regular waves. *Coastal Engng. 32*, pp. 255–287.

Madsen, P. A. and I. A. Svendsen (1983). Turbulent bores and hydraulic jump. *J. Fluid Mech. 129*, pp. 1–25.

Mei, C. C. and B. LeMehaute (1966). Note on the equations of long waves over an uneven bottom. *J. Geophysical Res. 71*(2), pp. 393–400.

Nwogu, O. (1993). An alternative form of the Boussinesq equations for nearshore wave propagation. *ASCE J. Waterway, Port, Coastal and Ocean Engng. 119*, pp. 618–638.

Packwood, A. (1983). The influence of beach porosity on wave uprush and backwash. *Coastal Engng. 7*, pp. 29–40.

Packwood, A. and D. H. Peregrine (1980). The propagation of solitary waves and bores over a porous bed. *Coastal Engng. 3*, pp. 221–242.

Peregrine, D. H. (1967). Long waves on beaches. *J. Fluid Mech. 27*, pp. 815–827.

Peregrine, D. H. (1983). Breaking waves on beaches. *Ann. Rev. Fluid Mech. 15*, pp. 149–178.

Peregrine, D. H. and I. A. Svendsen (1978). Spilling breakers, bores and hydraulic jumps. *Proc. of 16th ICCE*, ASCE, pp. 540–550.

Press, W. H., B. P. Flannery, S. A. Teukolsky, and W. T. Vetterling (1992). *Numerical recipes in fortran* (2nd ed.). Cambridge: University Press.

Resch, F. J. and H. J. Leutheusser (1972). Reynolds stress measurements in hydraulic jumps. *J. Hydraulic Res. 10*, pp. 409–430.

Resch, F. J., H. J. Leutheusser, and M. Coantic (1976). Etude de la structure cinematique et dynamique du ressaut hydraulique. *J. Hydraulic Res. 14*(4), pp. 293–319.

Rouse, H., T. T. Siao, and S. Nagaratnam (1959). Turbulence characteristics of the hydraulic jump. *Transactions of the ASCE 124*, pp. 926–966.

Schäffer, H. A., R. Deigaard, and P. A. Madsen (1992). A two-dimensional surf zone model based on the Boussinesq equations. *Proc. of 23rd ICCE*, ASCE, pp. 576–589.

Schäffer, H. A., P. A. Madsen, and R. Deigaard (1993). A Boussinesq model for wave breaking in shallow water. *Coastal Engng. 20*, pp. 185–202.

Shapiro, R. (1970). Smoothing, filtering and boundary effects. *Rev. of Geophys. and Space Phys. 8*(2), pp. 359–387.

Skjelbreia, L. and J. Hendrickson (1961). Fifth order gravity wave theory. *Proc. of 7th ICCE*, ASCE, pp. 184–196.

Southgate, H. N. (1993). Review of wave breaking in shallow water. HR Published paper no. 71. Presented at *The Soc. Underwater Tech. Conf. on Wave Kinematics and Env. Forces.*

Svendsen, I. A. (1999). Hydrodynamics of the surf zone. International Handbook of Coastal Engng., In Press.

Svendsen, I. A. and P. A. Madsen (1984). A turbulent bore on a beach. *J. Fluid Mech. 148*, pp. 73–96.

Svendsen, I. A. and U. Putrevu (1993). Surfzone wave parameters from experimental data. *Coastal Engng. 19*, pp. 283–310.

Svendsen, I. A., H. A. Schäffer, and J. B. Hansen (1987). The interaction between the undertow and the boundary layer flow on a beach. *J. Geophysical Res. 92*(c11), pp. 11845–11856.

Svendsen, I. A., J. Veeramony, J. Bakunin, and J. T. Kirby (1998). The flow in weak turbulent hydraulic jumps. Submitted to *J. Fluid Mech.*

Svendsen, I. A., K. Yu, and J. Veeramony (1996). A Boussinesq breaking wave model with vorticity. *Proc. of 25rd ICCE*, ASCE, pp. 1192–1204.

Tanaka, M. (1986). The stability of solitary waves. *Phys. Fluids 29*(3), pp. 650–655.

Tao, J. (1983). Computation of wave runup and wave breaking. Internal Report, Danish Hydraulic Institute, Hørsholm.

Ting, F. C. K. and J. T. Kirby (1994). Observations of undertow and turbulence in a laboratory surfzone. *Coastal Engng. 24*, pp. 51–80.

Twizell, E. H. (1984). *Computational methods for partial differential equations.* West Sussex, England: Ellis Horwood Ltd.

Van Dongeren, A. R. and I. A. Svendsen (1997). Absorbing-Generating boundary condition for shallow water models. *ASCE J. Waterway, Port, Coastal and Ocean Engng. 123*(6), pp. 303–313.

Veeramony, J. and I. A. Svendsen (1998). The flow in surf zone waves. Submitted to *Coastal Engng.*

Wei, G. and J. T. Kirby (1995). A time dependent numerical code for extended Boussinesq equations. *ASCE J. Waterway, Port, Coastal and Ocean Engng. 120*, pp. 251–261.

Wei, G. and J. T. Kirby (1998). Simulation of water waves by Boussinesq models. Technical Report CACR-98-02, Center for Applied Coastal Research, University of Delaware, Newark, DE 19716.

Wei, G., J. T. Kirby, S. T. Grilli, and R. Subramanya (1995). A fully nonlinear Boussinesq model for surface waves. I. Highly nonlinear, unsteady waves. *J. Fluid Mech. 294*, pp. 71–92.

Wei, G., J. T. Kirby, and A. Sinha (1999). Generation of waves in Boussinesq models using a source function method. *Coastal Engng.*, in press.

Whitham, J. B. (1974). *Linear and non-linear waves.* New York: John Wiley.

Yoon, S. B. and P. L.-F. Liu (1989). Interactions of currents and weakly nonlinear water waves in shallow water. *J. Fluid Mech. 205*, pp. 397–419.

Yu, K. (1996). *Breaking waves in the surf-zone.* Ph. D. thesis, University of Delaware.

Yu, K. and I. A. Svendsen (1995). Breaking waves in surf zone. *Coastal Dynamics '95*, Gdańsk, Poland, pp. 329–340.

Zelt, J. A. (1991). The run-up of nonbreaking and breaking solitary waves. *Coastal Engng. 15*, pp. 205–246.